8-2014

Theoretical Studies of the Growth and Functionality of Layered Materials

Wei Chen
University of Tennessee - Knoxville, wchen18@vols.utk.edu

To the Graduate Council:

I am submitting herewith a dissertation written by Wei Chen entitled "Theoretical Studies of the Growth and Functionality of Layered Materials." I have examined the final electronic copy of this dissertation for form and content and recommend that it be accepted in partial fulfillment of the requirements for the degree of Doctor of Philosophy, with a major in Physics.

Hanno H. Weitering, Major Professor

We have read this dissertation and recommend its acceptance:

Yanfei Gao, Adriana Moreo, Haidong Zhou, Zhenyu Zhang

Accepted for the Council:

Carolyn R. Hodges

Vice Provost and Dean of the Graduate School

(Original signatures are on file with official student records.)

8-2014

Theoretical Studies of the Growth and Functionality of Layered Materials

Wei Chen
University of Tennessee - Knoxville, wchen18@vols.utk.edu

To the Graduate Council:

I am submitting herewith a dissertation written by Wei Chen entitled "Theoretical Studies of the Growth and Functionality of Layered Materials." I have examined the final electronic copy of this dissertation for form and content and recommend that it be accepted in partial fulfillment of the requirements for the degree of Doctor of Philosophy, with a major in Physics.

Hanno H. Weitering, Major Professor

We have read this dissertation and recommend its acceptance:

Yanfei Gao, Adriana Moreo, Haidong Zhou, Zhenyu Zhang

Accepted for the Council:
Carolyn R. Hodges

Vice Provost and Dean of the Graduate School

(Original signatures are on file with official student records.)

Theoretical Studies of the Growth and Functionality of Layered Materials

A Dissertation Presented for the

Doctor of Philosophy

Degree

The University of Tennessee, Knoxville

Wei Chen

August 2014

to my parents

Acknowledgements

The past five years towards Ph.D. degree was a great journey in my life to discover natural sciences, and more importantly to learn about myself. There were moments of positive as well as negative, and herein I would like to thank people who support and help me in completion of this thesis.

My deepest appreciation goes to my Ph.D. advisor, Prof. Zhenyu Zhang, for his comprehensive, insightful, and inspiring guidance in my doctoral study. His optimistic attitude of life and extremely enthusiastic pursuance towards science teach me a lot during this important period. Meanwhile, I would like to greatly thank him for the continuous and generous support after his leaving from Univ. of Tennessee.

I am grateful to Prof. Wenguang Zhu, for his kindness in teaching me techical skills and continuously giving me thoughtful suggestions.

My sincere thanks also go to Prof. Efthimios Kaxiras, for offering me a research fellow position in his group and advising me on projects with patience.

I am pleased to thank the members of my doctoral committee, Prof. Hanno H. Weitering, Prof. Yanfei Gao, Prof. Adriana Moreo, and Prof. Haidong Zhou, for reading the drafts of this dissertation and providing valuable suggestions.

I would like to thank the former group members and colleagues at UT and ORNL, where I spend the first two and a half years: Dr. Hua Chen, Dr. Xiaoguang Li, Mr. Zhiling Dun, Dr. Guangfen Wu, Dr. Guo Li, Prof. Gong Gu, Prof. Tim P. Schulze, Prof. Di Xiao, Prof. Shunfang Li; the current and former group members at USTC, where I visited every summer: Dr. Ping Cui, Dr. Haiping Lan, Prof. Shifei Qi,

Mr. Wei Qin, Mr. Gufeng Zhang; the group members at Harvard University, where I visited for two years: Mr. Ekin Dogus Cubuk, Mr. Chao Chen, Mr. Yuan Yang, Dr. Brad Malone, Dr. Georgios Tritsaris, Dr. Weili Wang, Dr. Grigory Kolesov, Mr. Dmitry Vinichenko, Dr. Elton Santos. Thank all for the valuable discussions and enjoyable time we had together.

I am grateful to my girlfriend, for her encouragement and company.

Last, and most importantly, my gratitude goes to my parents for their unconditional love and support throughout my life.

Abstract

In this thesis, we present several projects on the growth and functionality of layered materials, using density functional theory (DFT) method and phenomenological modeling approach. Beyond the understanding of growth mechanisms and exploration of properties, we propose novel avenues to realize controllable growth processes and layered materials with desirable properties. The contents have three major parts:

(1) Graphene growth on Cu(111) and Ni(111) substrates. We first demonstrate that the inherent multi-orientational degeneracy of the graphene islands on Cu(111) in the early stages of nucleation could result in the prevalence of grain boundaries (GBs). Next, we propose a possible solution to tackle this standing obstacle, by invoking a functionalized Cu(111) surface to lift the orientational degeneracy and consequently suppress the GBs. Following this work, we explore the contrasting mechanisms of graphene bilayer growth on Cu(111) and Ni(111), develop a phenomenological model to predict the critical graphene size for the nucleation of the second layer underneath, and propose ways to substantially enhance the growth rate of the second-layer graphene on Cu.

(2) Contrasting alignment of hexagonal boron nitride (h-BN) and graphene grown on Cu(100). Collaborating with the experimental group, we find that the three-fold symmetric BN exhibits definitive orientation alignments when grown on the four fold-symmetric Cu(100) surface. This is in stark contrast to graphene/Cu(100) epitaxy, despite the crystallographic similarity between graphene and h-BN. Our results reveal that the stronger C-Cu interaction lead to the misalignment, a conclusion runs counter

to the conventional wisdom that stronger epilayer-substrate interactions enhance orientational order.

(3) Electronic and chemical properties of monolayer molybdenum disulfide (MoS_2) on metal substrates. We investigate the properties of a single-layer MoS_2 adsorbed on Ir(111), Pd(111), or Ru(0001). We find the contact nature is Schottky type, and the dependence of the barrier height on the work function exhibits a partial Fermi-level pinning picture. Using hydrogen adsorption as a testing example, we further demonstrate that the introduction of a metal substrate can substantially alter the chemical reactivity on the MoS_2 planar surface.

Table of Contents

List of Tables

List of Figures

Chapter 1

Introduction

Layered materials refer to the structures consisting of 2D platelets which are stacked by weak interactions [8]. Among them, graphene, as one of the most basic building blocks in the monolayer limit, has drawn tremendous attention in the area of condensed matter physics and material science since its first isolation from graphite [9]. Nowadays, the scientific community is advancing the other basic components in the low-dimensional form beyond graphene, such as h-BN, MoS_2, and particularly emphasizing on the artificial layered structures fabricated by stacking these building blocks together. In order to fully maximize the potential functionality, large-scale fabrication of high-quality of layered materials with controllable thickness and extensive understanding of their unique properties in device applications are necessarily required. In the first chapter, we will introduce the fabrication of various layered materials in the three- and two-dimensions, and their unique electronic, chemical, and magnetic properties.

1.1 Layered Materials: Three- (3D) and Two-dimensional (2D) Structures

The weak vdW interactions between layers indicates that there exists the low-dimensional form of layered materials, from their monolayer limit to a few layer nanosheets. Over the past decades, a number of methods have been developed to exfoliate layered materials because of a wide range of properties displayed in their low-dimensional structures [8, 10]. And lately, benefiting from the development of the exfoliation method, there are growing interests in its reverse process, which means stacking the monolayer or a few layer crystals back into the 3D form, but using different elementary building blocks mixed together [3]. In the realization of these structures, undesirable defects are usually introduced in various forms, which affect their intrinsic properties of layered materials [11]. In this section, I will present the background of the fabrication and structural properties of low-dimensional structures.

1.1.1 Fabrication of monolayer structures: from 3D to 2D

Mechanical Exfoliation

Layered materials, including graphite, h-BN, MoS_2, Bi_2Se_3, complex metal oxides, etc., exist stably as natural minerals in their 3D bulk structures. Figure 1.1 shows three representatives among them, all of which are widely used as dry lubricants, because of the extremely low friction when they slide between layers. Meanwhile, these natural layered materials are also utilized in many other industrial applications, such as electrodes, lithium-ion batteries, catalysts for various chemical reactions, and substrates for electronic devices.

The single layer of graphite had already been studied extensively in theory by many researchers since 1947 [12–15]. However, in history, for a long time free-standing atomic planes were often presumed not to exist because they are thermodynamically

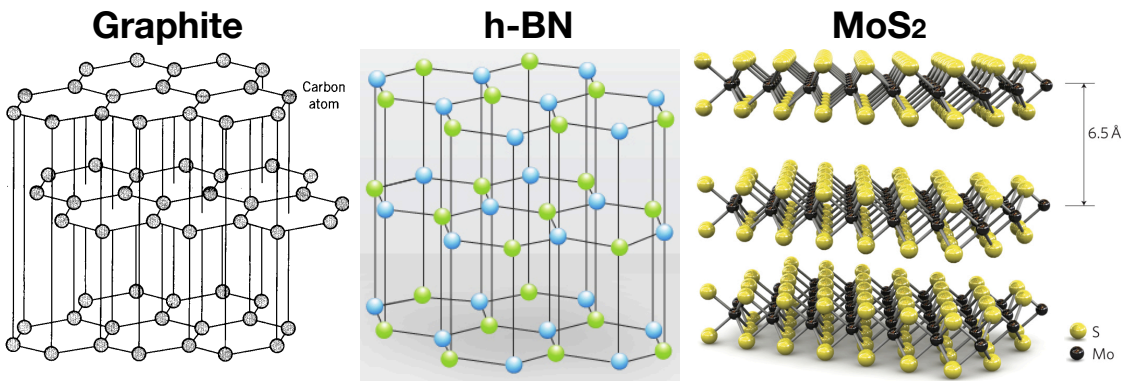

Figure 1.1: 3D structures of graphite, h-BN, and MoS_2.

unstable on a nanometer scale [16], and tend to scroll and buckle if unsupported [17]. Until October 2004, K. Novoselov, A. Geim and their collaborators showed that it is possible to isolate a single atomic layer nanosheet from graphite and transfer it to another substrate, so that the electric characterization could be realized [18], and this single layer of carbon is called graphene. Nowadays, it is believed that the intrinsic microscopic roughening at the nanoscale helps to stabilize the free-standing systems [19].

The mechanical exfoliation method for extracting thin layers of graphite from a graphite crystal with scotch tape was first suggested and tried by R. Ruoff's group, however, they were not able to identify any monolayer structures [20]. This method typically involves multiple exfoliation steps, each creating a slice with fewer layers. Geim and Novoselov succeeded by using an optical method with which they could identify fragments consisted of only a few layers, and then they managed to identify flakes made up of only a single layer [18]. Using this "scotch tape" technique, crystallites larger than 1 mm which are visible by naked eye can be realized for characterization and later used in device applications. Meanwhile, the successful exfoliation is not limited to graphite, but generally applicable to the fabrication of other single-layer structures, like h-BN, MoS_2, etc. [10], and quickly lead to the research boom of layered materials in condensed matter physics and

material science. Because of developing this simple but effective technique, and more importantly identifying the groundbreaking sinlge-layer freestanding structures, Geim and Novoselov received the Nobel Prize in 2009, soon after their discovery.

Fundamentals of epitaxial thin film growth

Epitaxial growth is widely used in material synthesis, proving an affordable method of high quality crystal growth for thin films [21, 22]. The epitaxial films may be grown by sources of gaseous or liquid precursors. In the growth process, the substrate serves as a seed crystal, so that the deposited film may choose one or more crystallographic with respect to the substrate crystal. This is in contrast to the non-epitaxial growth, in which the deposited film has disordered structure, or forms a random orientation regarding to the substrate. Epitaxial growth can be divided into two classes: one is homoepitaxial, in which the grown film and substrate are the same material; the opposite is heteroepitaxial. Since thin film growth is usually a non-equilibrium process, the competition between thermodynamic and kinetic parameters has to be considered depends on the growth conditions [23, 24].

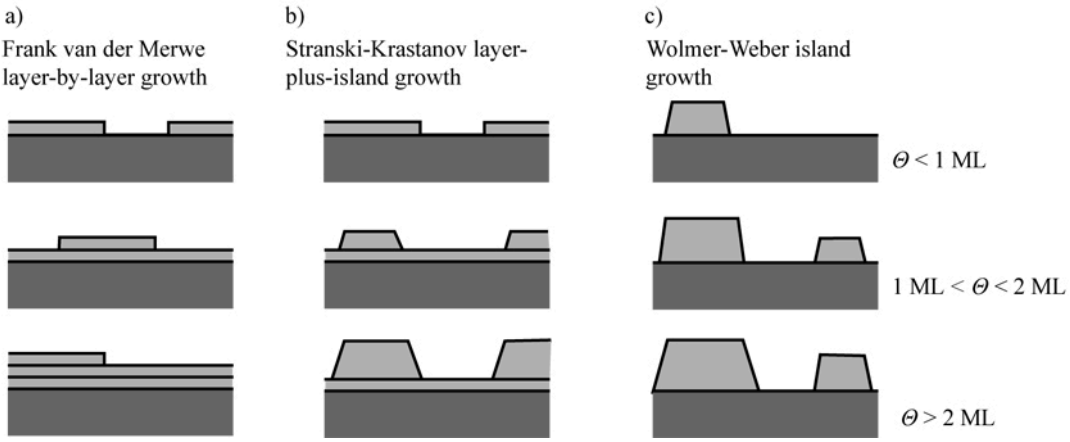

Figure 1.2: Schematic representation of three thin film growth modes. Θ is the number of monolayers. [1]

Regarding thermodynamics, i.e., competition between surface and interface energies of substrates and films, epitaxial growth is typically classified into three

modes: Frank-van der Merwe (layer-by-layer growth), Volmer-Weber (island growth), and Stranski-Krastanov (layer-by-layer followed by island growth) [1]. When the film atoms are more strongly bound to the substrate than to each other, layer-by-layer growth is achieved on the substrate, with generally the best crystalline quality of films. While in the Volmer-Weber growth mode, the atoms of the film bond with each other more stronger than with the substrate, therefore 3D islands nucleate and grow on the substrate. In the intermediate growth situation, growth is initiated with layer-by-layer, and then continues to form 3D islands after a few atomic layers, which depends on strain and the chemical potential of the deposited film.

The kinetic factors play important roles in the non-equilibrium growth. The most crucial kinetic mechanisms include adatom diffusion on terraces, along steps, and around island corners; nucleation and dynamics of the stable nucleus; atom attachment to and detachment from terraces and islands; and interlayer mass transport [23]. These basic atomistic processes are responsible for almost all the complex growth situations, and should be well understood to precisely control the quality of the fabricated thin films. For example, by reducing the activation barrier for atoms to cross steps by utilizing surfactants, the layer-by-layer growth is substantially enhanced [25].

Epitaxial growth of 2D crystals

As mentioned above, most of the 2D materials can usually be isolated by mechanical cleavage method for experimental measurement and characterization, because they are stacked by weak vdW interactions into the form of bulk [18]. However, this method is not feasible for large-scale production into device application. Nowadays, among the other different fabrication avenues being explored, epitaxial growth of 2D crystals have been realized on various substrates, including metals and insulators, and stands out as a highly appealing approach.

The advantage of growing 2D materials on insulator is that transfer to another insulator is not required. The idea of graphitization of silicon carbide (SiC) by Si

sublimation during high-temperature vacuum annealing was demonstrated in the 1960s [26]. However, the substrate surface is coved by small graphene domains with varying thickness, which limit its performance in device applications [27]. The continuity and uniformity is later greatly improved by graphitization of Si-terminated SiC(0001) surface in an argon atmosphere, in which monolayer graphene films of much larger domain sizes are achieved [28]. The improvement in quality is due to the fact that, the argon gas molecules hinders the transport of Si atoms away from the SiC surface, therefore reducing the overall sublimation rate and allowing an increase in graphitization temperature by several hundred degrees [27, 28].

Graphene growth on transiton metal substrates is remarkably easy, and it is shown to yield macroscopic single-crystalline graphene domains with very low defect density and also better achievable thickness control. The fabrication has been achieved on many different metal substates, including noble metals: Ir, Ru, Pt, Pd, Rh, Au, etc. [29–35], and low-cost metals: Ni and Cu [36, 37]. The growth mechanism varies on different metal surfaces, and roughly can be classified into two major processes by the carbon solubility [38]: first, on metals with significant carbon solubility, such as Ni, carbon dissolve into the bulk at high temperature, and then segregate from the bulk upon cooling of the substrate, resulting in graphene overlayers [36]; second, hydrocarbon molecules, like methane, ethylene, and benzene, dehydrogenate on the metal surface, such as Pt, Cu, and then immediately nucleate to form graphene films [32, 37].

Because of the low carbon solubility, relatively small lattice mismatch with graphene, and the effectively nucleation of carbon on the metal terrace [39], Cu surface enables the best platform to grow high-quality single-crystal graphene among all the metal substrates [37]. Figure 1.3 shows the common experimental setup for the chemical vapor deposition (CVD) growth of graphene on Cu substrates [2]. The mass flow controllers (MFC) are used to provide hydrocarbon molecules and other reactant gases with a controllable flow rate. The Cu foils are heated to high temperature in the furnace, and then catalyze the carbon sources deposited on the surface. Indeed,

it has been reported that single-layer domains of monolayer graphene grown on Cu foils can reach the dimensions of 0.5 mm on a side [40]. Moreoever, transfer of graphene to other substrates are demonstrated to be readily realized by chemical etching methods [41, 42].

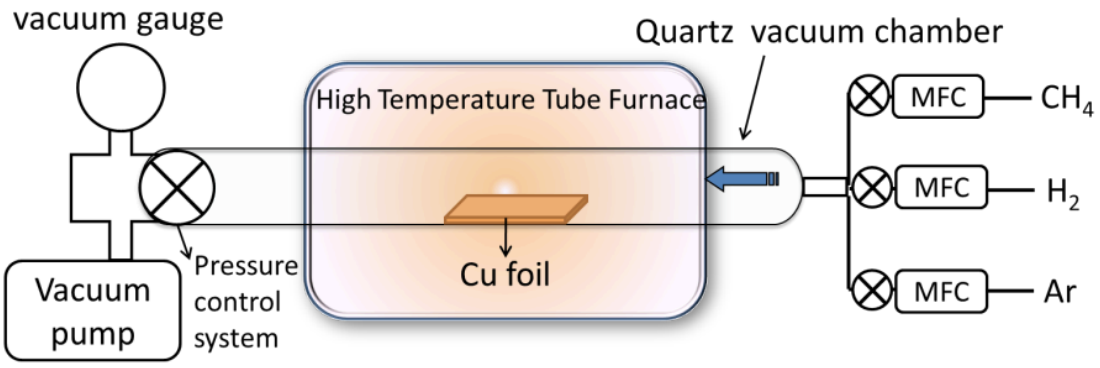

Figure 1.3: Illustration of a common setup for CVD growth of graphene on Cu substrates. [2]

The epitaxial growth method is also applicable for the synthesis of monolayer or a few layers h-BN and transition metal dichalcogenides (TMDC), such as MoS_2, but employing different sources and experimental procedures. For growth of h-BN on Cu, ammonia borane (NH_3-BH_3) is generally used. The nucleated islands are observed to be usually with triangular shape, in contrast to some of the previous report on hexagonal shape graphene grown on Cu, which is due to the more energetically favored nitrogen-terminated edges [43, 44]. The h-BN growth is found to follow the Frank-van der Merwe model for the first layer, and then changes to Stranski-Krastanov model afterwards. It was reported that the growth under low-pressure CVD is found to be not self-limited, other than the case of graphene [44]. For growth of MoS_2, the thiophenol (C_6H_6S) molecules are deposited on Cu(111) surface, followed by the removal of the phenyl groups through annealing. Molybdenum is subsequently deposited, and MoS_2 films form after annealing [45].

Other methods

Besides the approaches described above, there are several other methods to fabricate 2D crystals. For example, by cutting the one-dimensional (1D) carbon nanotubes, 2D graphene overlayer is created [46, 47]. This fancy approach is demanding with respect to the unzipping accuracy and efficiency, and should be difficult to popularized. Another method is the reduction of graphite oxides monolayer films by hydrazine, annealing in argon and hydrogen. However, the fabricated graphene has lower quality compared to sctoch-tape graphene, because functional groups are removed incompletely [48]. Above all, briefly speaking, currently mechanical exfoliation is still the most widely used approach to fabricate graphene for experimental characterization and measurement, and epitaxial graphene on metal substates, especially on Cu surfaces, hold the promises for large-scale fabrication for industrial applications.

1.1.2 Van der Waals (vdW) heterostructures: from 2D to 3D

"Library" of 2D crystals

2D crystals, with their simple structures, for example, the hexagonal lattice of graphene, provide possibilities to explore many physical phenomena, such as quantum Hall effect. Going beyond this field, it is expected that sandwich structures, made of two, three, or more different layers of 2D materials can bring even greater scope. As a result of the development of atomic-scale characterization and control of nanoscale materials, 2D crystals now can be accurately reassembled into their 3D form layer by layer, with individual layers of very different character combined together. In the 3D structures, the strong covalent bonds provide in-plane stability, whereas the relative weak vdW interactions are sufficient to hold the stack together [3].

In the existing library of 2D crystals, there are hundreds of layered materials that cleave easily from their bulk structures; however, not all of them can be used in the assembly of heterostructures. Generally, thin films have lower melting temperature and higher chemical reactivity when their thickness is decreased, therefore, at the

extreme situation of monolayers, most 2D materials are stable at ambient conditions (room temperature in air) only by passivating their surfaces [49]. In fact, monolayer of graphene is shown to be more reactive than even bilayer [50, 51]. Meanwhile, the current isolation methods of 2D crystals cannot be conducted in high vacuum or at low temperature. Therefore, despite of the enormous stable 3D bulk structures, the library of atomically thin 2D crystals available in making the vdW heterostructures is currently quite limited [3].

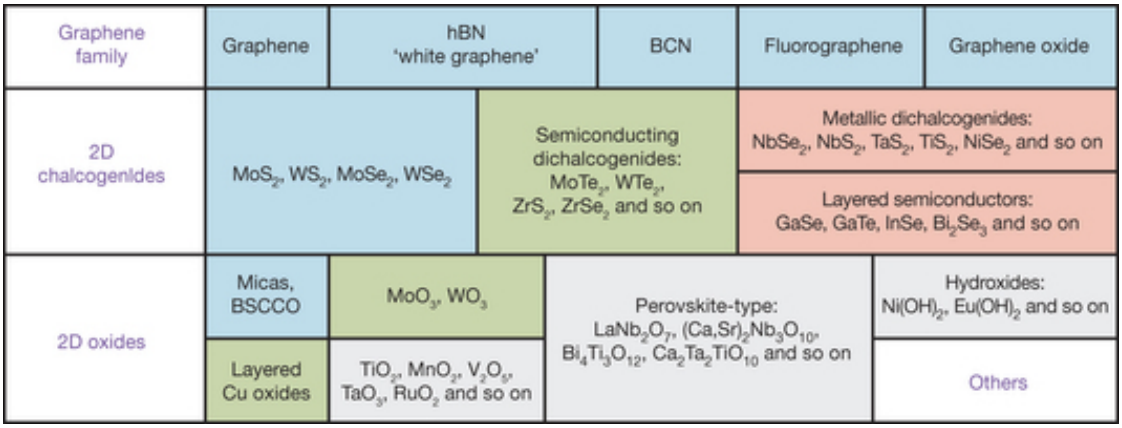

Figure 1.4: Current library of 2D crystals possible in making vdW heterostructures. The color of shade indicates the stability of monolayer structures: blue means monolayers are stable under ambient conditions; green implies monolayers are probably stable; pink indicates monolayers are stable in inert atmosphere; grey means monolayers are successfully isolated, but more information is required. [3]

Figure 1.4 shows the current library of 2D crystals, which may be assembled into vdW heterostructures. According to the information of stability, graphene, h-BN, and TMDC, such as MoS_2, are likely to be the most common components in future 2D crystal-based heterostructures and devices. Graphene, h-BN, and MoS_2 are semi-metal, insulator, semiconductor, respectively, therefore should play different roles when stacked together: graphene exhibits micrometre-scale ballistic transport and extremely high carrier mobilities at room temperature or even low temperature in electronic devices [52–55]; h-BN is used as gate dielectrics and tunnel barriers [56–59], and it has shown to preserve the unique electronic properties of graphene when

serving as the substrate [60]; MoS_2 has dependence of band structures on the number of layers [61, 62], exhibit stronger spin-orbit coupling [63] than graphen and h-BN, and shows the possibility to control spin and valley by polarized light in 2D materials [64–68].

Graphene has many derivatives, for example, graphane [51, 69], fluorographene [70–72], and graphene oxide [73–75], which have hydrogen, fluorine, and oxygen terminating the surface of graphene, respectively. Because of the passivation of surface atoms, chemically, the derivatives sometimes are more stable than the 2D crystals themselves [70, 72, 76]. The in-plane mixture of graphene and h-BN, monolayer of boron carbon nitride, has also been realized by several research groups, and exhibit different geometries and impressive properties [77–79]. As seen in Figure 1.4, there are many and various types of monolayer oxides [8, 80–83], however, more measurements on their stability are required to be conducted. Above all, there are quite a few 2D crystals available, and more being explored, to be considered as components in designing vdW heterostructures.

Approaches of assembly: current and prospective

Currently, the assembly procedure invokes firstly the preparation of 2D crystals, from scotch-tape technique [18], or epitaxial growth on metal substrates [84]. Then the crystals are transferred on top of a thin transparent film [85–89], for example, PMMA polymer, which allows characterization of the atomic structure and orientation of the materials using an optical microscope [90–93]. Then the fabricated 2D crystals can be deposited onto another prepared 2D materials, with the transparent film facing up. Next the supporting substrate will be removed, generally by chemical dissolution [89, 94, 95]. By repeating the transfer procedure, more 2D components are deposited into the stacked structure, until a desirable sequence is realized.

Although the idea of making heterostructures is simple and straightforward, the manipulation with precision at the atomic scale is severely demanding. The flakes

of 2D crystals on the suspended substrate are located by the optical microscope. Then the 2D crystals and the supporting films are precisely aligned and deposited to contact with another 2D materials or pre-stacked heterostructures, by using the arm of a micromanipulator mounted on the microscope [96, 97]. During the transfer, the target substrate is usually heated up, in order to remove the contaminants at the interfaces. The vdW forces between adjacent 2D crystals effectively drive off the trapped contaminants, or creating bubbles, and further clean them off the interface [3, 98–100].

It is inefficient to create vdW heterostructures through layer-by-layer deposition with manual operations. Moreover, the size of the assembled structure is usually quite limited for large-scale fabrication by this method. One would ask if these 2D crystals can epitaxially grow on top of each other by order. Indeed, there are successful examples of growing stacked structures, such as graphene/h-BN and graphene/MoS_2 heterostructures [101–104]. In practice, the epitaxial growth method cannot be generalized, because the interlayer interaction is only weak vdW force, and the atoms of the epilayer bond with each other more stronger than with the underlying crystals, therefore the Volmer-Weber (island) growth mode is usually preferred, so that precise control of thickness is difficult to be obtained [3]. To fully suppress the island growth, a fine tuning of the growth conditions, such as growth temperature, choice of precursors, flux rate, and growth time, is necessarily required. To achieve a self-limiting growth of only monolayer each growth period, properly choosing the surfactant [25] to alter the kinetic processes may be an effective avenue. Future theoretical studies are needed to provide instrumental guidance to development of novel experimental approaches, in order to lower the expenses in making vdW-heterostructure devices.

Examples of vdW heterostructures

There are several examples of vdW structures and devices: the graphene/h-BN heterostructure made from alternating graphene and h-BN layers, has shown tunable metal-insulator transition [105]; a double-layer graphene heterostructure with

ultrathin h-BN spacers is used to measure the Coulomb drag and symmetry breaking in interacting layers [106]; 2D superconductivity is observed at the interface of a Bi_2Te_3/FeTe heterostructure [107]; at certain orientations of a graphene overlayer with respect to a monolayer h-BN, the physical phenomena of Hofstadter's butterfly and superlattice Dirac points are observed, due to the periodic superlattice potential [108–110].

Actually, the advancing of vdW heterostructures has just begun. With so many 2D layered materials as the basic components, huge space of sequences and parameters to be considered, it is optimistic that increasingly sophisticated heterostructures will become available by improving the fabrication techniques, thus greatly enriches the exotic properties and unusual physical phenomena of layered materials beyond graphene, such as field-effect transistors (FETs), spin- and valleytronics, thermoelectrics, topological insulators, and reaction catalyst, etc.

1.1.3 Structural defects in layered materials

Crystals are always imperfect and contain structural defects. As we learned from the field of semiconductor devices, defects can significantly alter the performance of materials [111]. When we look at the layered materials, their monolayer or a few layer structures have been proposed as candidates for the next-generation electronics [112]. Because of the nature of low-dimensionality, the properties should be more sensitive to the structural defects in 2D crystals. At the same time, their atomically thin structures make it easier to introduce defects, of either desirable or undesirable [113]. Next, according to their geometry and shape, the defects in the layered materials are categorized and discussed below.

Point defects

Point defects are unavoidable in any material according to the second law of thermodynamics, and are particularly remarkable in 2D materials epitaxially

grown [114]. The complete absence of point defects means reducing the entropy of the system to zero, which would requires an infinite amount of work. In graphene, by removing just one carbon atom, the simplest defect, a single vacancy (SV) is created. The resulting three dangling carbon atoms then undergo a Jahn-Teller distortion [115], which saturate two of the three dangling bonds, with one dangling electron remained [116]. Because of the high formation energy, SV is generally created by irradiation with energetic particles [117], or during high-temperature crystal growth [118], and has been identified by scanning tunneling microscope (STM) [119] or transmission electron microscopy (TEM) [120, 121]. Double vacancies (DV) is formed by removing two neighboring carbon atoms in graphene. Thermodynamically, DV are more favored than SV [11]. The removal of more than two atoms will result in larger and more complex defects, and a reconstruction is generally required at the edge of the defect site.

When one of the carbon-carbon bonds is rotated by 90° in-plane, four hexagons become two pentagons and two heptagons, and it is called the Stone-Wales (SW) defect [11] (Figure 1.5a). The creation doesn't require removal of any carbon atoms and no dangling electrons are created. The formation of SW defect is calculated to be 4.9 eV [4], and the kinetic barrier is about 10 eV. When graphene is under stress, this kinetic barrier is greatly reduced, and a large enough strain will result in a negative value of the formation energy [122].

Because of the structural similarity, the point defects in graphene all exist in h-BN. The energy of electron beams required to create a SV in h-BN is close to that in graphene, and the boron atoms are more likely to be ejected than nitrogen atoms [123]. When electrons are injected into h-BN, four-atom vacancies, with three boron and one nitrogen, are more favorable [113]. Moreover, the existence of SW defects is also suggested by theoretical calculations [124, 125].

The epitaxial grown MoS_2 is reported to have six different types of point defects: monosulfur vacancy (V_S), disulfur vacancy (V_{S2}), vacancy complex of Mo and nearby three sulfur (V_{MoS3}), vacancy complex of Mo and nearby three disulfur pairs (V_{MoS6}),

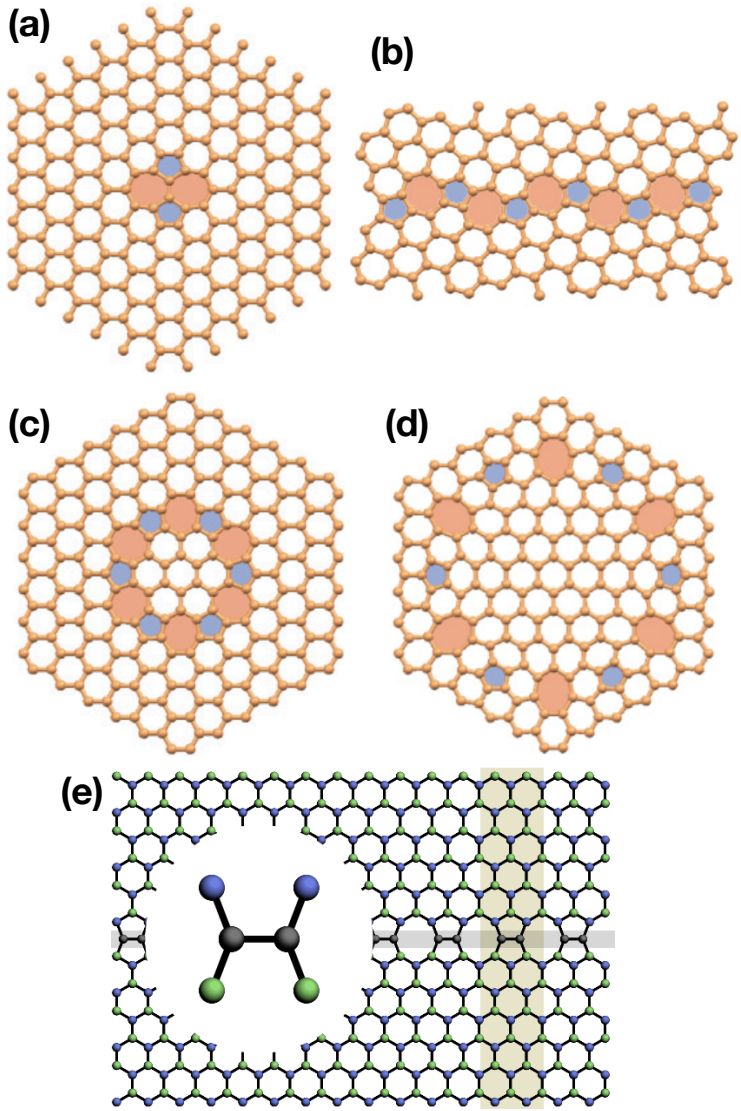

Figure 1.5: Schematic structures of (a) a SW defect, (b) a large-angle GB, (c) a flower defect (GB loop), (d) a larger GB loop, and (e) a 1D line defect in graphene. [4, 5]

and antisite defect where a Mo substituting a S_2 column (Mo_{S2}) or a S_2 column substituting a Mo atom ($S2_{Mo}$) [114, 126]. Meanwhile, these kinds of vacancies and antisite defects are also suggested to exist in Bi_2Se_3 [127, 128]. The formation energies of these defects depend on the chemical potential of the elements, which is determined by the experimental conditions [114, 127]. Different environments will result in the abundance of distinct defects.

GBs and line defects

The point defects in layered materials can be considered as zero-dimensional (0D) defects, while there are also 1D and 2D defects in the 2D crystals. In the epitaxial growth of graphene, when two domains with different lattice orientations merge, a GB is formed [11, 129]. As seen in Figure 1.5b, a large-angle GB can be regarded as a line consisted of alternating pentagons and octagons [4]. When the pentagons and octagons are incorporated into graphene in a closed loop, a closed GB loop can form. For example, in the structures of GB loops in Figure 1.5c and d, two different sizes of inner graphene domain are rotated away from their orientations in the pristine lattice [4, 130]. Indeed, even without misorientations between domains, a line defect can be formed by a translation of two half-lattices relative to one another, which consists of a pair of pentagons and one octagon periodically repeated along the dislocation line [5, 131] (Figure 1.5e).

The structures of GBs and/or line defects are also observed in the h-BN [132–134], MoS_2 [114, 135–137], and Bi_2Se_3 [138, 139]. Because of their differences in the crystalline symmetry and chemical elements, the local structures of the defects may be remarkably different in these 2D materials. For example, MoS_2 has three structural phases (1T, 2H, and 3R), therefore the line defect formed at the boundary between two phases cannot have its similarity in graphene and h-BN [137]. Also, the relative rotation between domains in a graphene GB can be $[0°, 30°]$, while in BN and MoS_2, the angles of GB range from 0° to 60°.

Although the GBs and line defects in 2D materials have shown unique properties and functions for potential applications [114, 131, 138, 140], to utilize them, precise control of their atomic structures are necessarily required, which seems to be difficult at the present time. Meanwhile, these defects mostly weaken the mechanical strength of 2D crystals [129], and sometimes severely affect their transport properties [42, 141]. Therefore, deeper understandings on their formation mechanisms in the epitaxial growth, such as the preference of angle distribution of GBs [129], are needed to suppress their formation, and one-step further, to control their creation for utilization. Some investigations on these issues are performed during my Ph.D., and they will be detailed in this thesis below.

1.2 Intrinsic and Desirable Properties of Layered Materials

Due to quantum confinement in the out-of-plane dimension, the 2D materials have displayed distinct properties from their bulk counterparts. The uniqueness is reflected in the novel physical phenomena demonstrated in the low-dimensional systems. As for functionality, extraordinary performance has also been shown in many of the nano-scale devices based on layered materials [81]. An exceptional advantage of utilizing the 2D crystal is that, the low-dimensionality nature makes it simpler and more accessible to realize desirable properties by design and modification. Large surface area on both sides is provided for surface construction and contact with other materials, such as doping by element substitution, molecule adsorption, or intercalation between layers. The simple structures and atomically thin thickness make it easier to cut 2D materials with desirable edge structures. They can be rolled, or applied with strain, and meanwhile interact more extensively with light, and pure electric or magnetic fields. In this session, I will introduce several novel properties that are related to the

layered materials, with more emphases put on the electronic, chemical, and magnetic aspects, and potential design strategies of the properties are also discussed below.

1.2.1 Electronic properties

Dirac electron systems

Graphene is a "wonder" material with many unique properties, however, what really makes graphene stand out from other layered materials is its Dirac-like electron behavior. Graphene is a semi-metal with zero band gap, in which the charge carriers show a linear dispersion in the vicinity of Fermi level where the Dirac points locate (the six corners of the 2D hexagonal Brillouin zone, see Figure 1.6a). Accordingly, graphene has zero effective mass for electrons and holes, which behave like relativistic particles described by Dirac equation for spin-1/2 particles. The electrons and hole can travel without scattering in the absence of defects, thus showing a remarkably high mobility in excess of 15000 $cm^2 \cdot V^{-1} \cdot s^{-1}$ at room temperature [6, 142]. Its electronic behaviors can be further tuned by applying external electric or magnetic fields, or by controlling the geometry or topology, such as edge termination (zigzag, armchair, or mixed) and stacking order. One example is that, because of graphene's massless Dirac electrons, quantum anomalous Hall effect was firstly observed in graphene in the presence of magnetic field at room temperature [143–145].

The Dirac electronic structure also exists in the surface states of 3D topological insulators [7, 146–148]. Topological insulators are materials which are insulating in bulk, but have conducting states on their surface or edge. The metallic surface states are results of the combination of spin-orbit coupling and time-reversal symmetry, and are robust against impurities and defects [149]. As shown in Figure 1.6b, unlike graphene, which has up and down spins at each point on the Fermi surface, the surface states of topological insulators have no spin degeneracy. By doping with magnetic elements, the quantum anomalous Hall effect was realized in topological insulators without applying external magnetic fields [150]. In addition to the fundamental

research, the surface states are also suggested for applications in the fields of spintronics and quantum computation [148]. There are several theoretical proposals in turning graphene into a 2D topological insulator, which has robust conducting states along the edges, by increasing the spin-orbit coupling to open a band gap at the Dirac points [151–154]. However, the difficulties lie in the stability of resulting systems, the size of the created band gap, and the position of Fermi level.

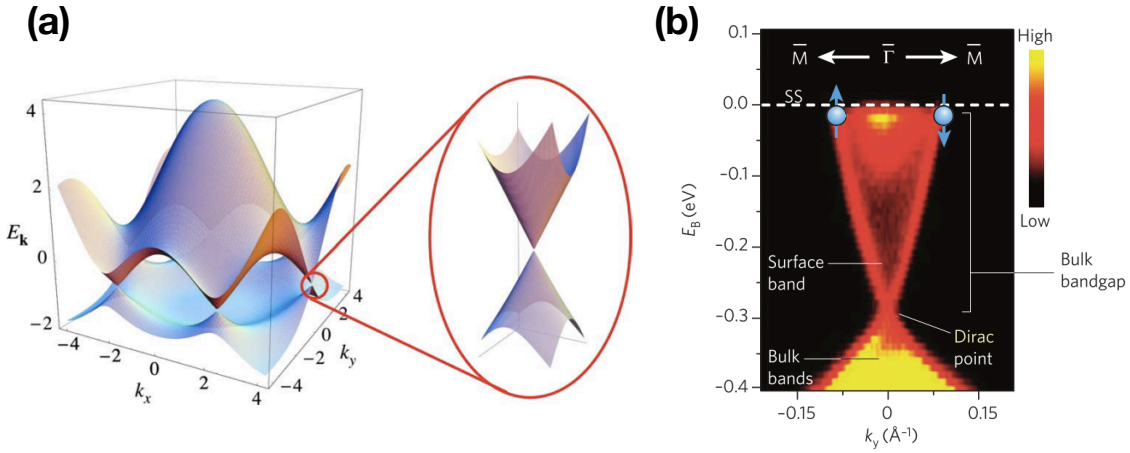

Figure 1.6: (a) Electronic dispersion of graphene in reciprocal space, with zoom in of the energy bands close to one of the Dirac points. (b) Electronic structures of Bi_2Se_3, measured by angle-resolved photoemission spectroscopy (ARPES). The blue arrows indicate the direction of electron spin. [6, 7]

Metal-semiconductor contacts

The transistor is the most basic building block in fabricating electronic devices. Graphene, by opening a sizeable band gap [155], and the single-layer MoS_2 [156], with an intrinsic band gap of 1.8 eV, both have been demonstrated to make FETs, and shown extraordinary performance. According to the structures and components of FETs, semiconductors are necessarily required to contact with metals. At the metal-semiconductor interfaces, phenomena including structural reconstruction, charge transfer, and alignment of electronic energy bands generally happen [157].

A metal-semiconductor contact can be divided into two types: one is ohmic contact, in which the electrical junction has a linear current-voltage (I-V) curve

described by Ohm's law; the other is Schottky contact, where a potential energy barrier for electrons is formed at the interface. The type of contact is determined by the alignment between the conduction and valence bands of the semiconductor, and the Fermi level of the metal [158]. If the Fermi level is above the conduction or below the valence band edge, ohmic contact formed; otherwise, the Fermi level is in the gap region of the semiconductor, forming a Schottky barrier with height ϕ_b. In practical applications, the ohmic contact is generally favored, and the Schottky-type can also be made into Schottky diode, Schottky transistors, etc.

The Schottky-Mott model predicts that $\phi_b = \Phi - \chi$, where Φ is the metal work function and χ is the semiconductor electron affinity [158]. It means by contacting with a metal having the proper work function, desired barrier height can be realized in the transistor. This simple model correctly point out the existence of band bending in the semiconductor, however, it commonly fails to predict the value of ϕ_b due to the Fermi level pinning effect [159, 160]. Because of the vacuum states in the semiconductor, or the metal-induced gap states resulting from chemical bonding at the interface, the Fermi level is usually pinned at the center of the band gap. Therefore, ϕ_b becomes insensitive to the work function of metal. In low-dimensional systems, the Fermi level pinning effect has shown a weaker impact, due to electrostatics at reduced dimensions [158]. For graphene-metal contacts, previous theoretical calculations suggest that Fermi level linearly depends on the metal work function, without any pinning effect [161]. However, in monolayer MoS_2, which is thicker than one atomic layer, a different behavior of Fermi level pinning is expected, and more details will be addressed in this thesis.

1.2.2 Chemical properties

Chemical stability and reactivity of 2D materials

Due to the absence of bulk and prevalence of surface area, 2D crystals are generally more chemically active than their bulk materials. Graphite is chemically inert

to almost all chemicals, however, graphene can adsorb and desorb various atoms and molecules, such as H, F, NO_2, OH, etc. [9] By complete adsorption of H or F at each carbon site, graphene is transformed into its derivatives: graphane or fluorographene. Thermal annealing and chemical treatment removes the adsorbates, and bring graphene back to its pristine state because of the structural stability against high temperature [51], which has been displayed in the epitaxial growth of graphene. Graphene is not strictly flat, and the resulting strain and curvature enhance the reactivity [162, 163]. Moreover, the defect and edge sites of graphene are shown to be more reactive locally [11, 164].

h-BN shows even higher chemical stability at high temperature than graphene [83], therefore widely used as dielectric layer and protective coating. The reactivity of its defect and edge sites still remain largely unexplored. In TMDC, the chemical properties are diverse, which depends on the composition and structure [165]. In particular, as shown in Figure 1.4, MoS_2, WS_2, $MoSe_2$, and WSe_2 are more stable among them. Even if the elements are given, there are structures with different phases, for example, in MoS_2, the 2H phase is more stable than 1T and 3R. The basal plane of MoS_2 overlayer is relatively inactive, while the edge sites are highly reactive, which serve as catalysts for hydrodesulfurization of petroleum and hydrogen evolution reaction (HER).

Design of new catalysts

Clean and renewable energy requires the search and development of novel catalysts. The basic guideline of designing materials is to change their original compositions and structures. Generally, the incorporation of noble metal atoms, or elements with excess electrons, and creation or increasement of active sites, will enhance the materials' chemical reactivity. There are successful examples among the 2D materials following this line: the substitutional doping of graphene by nitrogen provides more reactivity towards oxygen reduction reactions [166], because of introducing excess electrons; WS_2 in the stained metallic 1T phase (metastable)

is prepared by lithium intercalation chemical method, and show greatly increased catalytic activity for hydrogen evolution [167]; a mesoporous architecture of MoS_2 is demonstrated to be an excellent catalyst for hydrogen production, resulting from the abundant edge sites, which account for the reactivity [168].

Computational methods provide a powerful tool to investigate the catalytic properties of materials. In heterogeneous catalysis, the adsorption energies of intermediates are used as descriptors of catalytic activity. The volcano relations between the reaction rates and adsorption energies have been identified in many systems, such as CO methanation and hydrogen evolution. In the latter reaction process, one of the intermediates is the adsorbed hydrogen. If H binding on the catalytic surface is too weak, H^+ cannot effectively adsorb from the dissolved phase, and if the binding is too strong, the surface will be poisoned for further catalytic activity [169]. With the advances recently made in the accuracy of DFT calculations, the discovery or design of catalysts with desirable functions are getting cheaper and more effective.

1.2.3 Magnetic properties

Ferromagnetism in 2D materials

Ferromagnetism generally refers to the long-range magnetic ordering, in which unpaired electrons are aligned parallel to each other. This phenomena is the result of magnetic dipole-dipole and spin exchange interactions. The spins tend to align until a critical temperature is reached, called the Curie temperature, at which the entropy effect is more pronounced than the interactions. Usually, a Curie temperature higher than the room temperature is required for a material to be generalized. The 2D materials provide an ideal system to study the fundamental physical phenomena related to ferromagnetism, such as the quantum anomalous Hall effect [170], the Ruderman-Kittel-Kasuya-Yosida (RKKY) interaction [171], and moreover to realize

potential device applications, including spintronic, magnetoresistance, data storage, etc. [172]

The pristine 2D materials normally do not have ferromagnetically coupled spins. However, these systems have edge structures and are introduced with defect sites inevitably during preparation, both of which are shown be magnetic. Theoretical calculations and experimental measurements have provided supports to the existence of ferromagnetism arising from the uncoupled electrons at the edge and defect sites. For example, the uniform zigzag edges of graphene and MoS_2 exhibit ferromagnetic coupling [173–175]. The room temperature ferromagnetism is also established, due to the existence of point defects, or GBs in graphene or MoS_2 [176–179]. Ferromagnetism in graphene, formed only by light element of carbon without d electrons involved, is promising for fabricating low-cost devices; however, the control of local structures for magnetism are still quite demanding.

Magnetic doping and co-doping

Magnetic doping with transition metal, rare earth metal, or even non-metal elements is an effective approach to introduce ferromagnetic ordering in materials, such as the dilute magnetic semiconductors. The forms can be either substitutional doping, in which the original atoms are replaced by others, or doping by adsorption of atoms or molecules. Various elements and molecules have been proposed to magnetically dope graphene and the other 2D systems, but with almost all on the theory side [152, 180–183]. The reason is that a strong adsorption of adsorbate is required to stabilize the resulting 2D system, and the substitutional doping usually needs dopants with close atomic size to the original elements. Due to the absence of bulk, the 2D crystals can undergo structural reconstruction easily, therefore set high criteria for the design of magnetic systems.

Co-doping may provide a possible solution to this issue. This concept generally involves doping of the n-p pairs, in which the electrostatic interaction within the dopant pair effectively strengthens the thermodynamic and kinetic stability of the

system. A previous proposal of codoping method in TiO_2 has been demonstrated its application to tune the electronic band structure, thus the photoactivity [184]. In 2D crystals, doping of nickel-boron pairs is expected to functionalize graphene into a diluted ferromagnetic system, in which boron substitute carbon atoms due to their similar atomic sizes, and magnetic nickel atoms stably bond with the boron sites [185]. The idea of codoing offers more freedom and opportunities in the design of magnetic systems based on 2D crystals, further studies should be carried out to validate it, and in addition, to generalize it for other desirable properties, such as topological insulators.

1.2.4 Theoretical method: DFT

We use first-principle calculations within DFT to investigate the growth and functionality of layered materials. DFT was initiated from Hohenberg-Kohn theorems [186], which point out the unique relation of the external potential (arising from the positive charges of the nuclei) within a N-electron system and its electron density, and the density contains all the information of the system, including both ground states and excited states. Afterward, Kohn and Sham proposed a empirical methodology to construct the density functional by introducing the exchange-correlation potential [187].

For practical calculations, the exchange-correlation functional has to be treated on a approximate way. The local density approximation (LDA) [188, 189] is the basis of all the approximate functionals, which is based on the free electron gas model. LDA works very well for certain systems, however, the electron distribution in real materials is far from being uniform, therefore LDA is sometimes insufficient for accurate calculations. Beyond LDA, generalized gradient approximation (GGA) is widely used, taking account of the gradient of the charge density to supplement the uniform density. There are numerous functionals based on GGA, such as Perdew-Burke-Ernzerhof (PBE-GGA) [190], PW91 [190], and BLYP [191, 192].

In many of the real systems, the vdW interactions play a very important role [193]. The above density functionals cannot correctly describe vdW interactions, which result from the dynamical correlations between fluctuating charge distributions. Currently, two popular methods are used to include the vdW part: one is the vdW-DF functional, a non-local correlation functional that accounts for dispersion forces approximately [194, 195]; the other is a pragmatic method by adding a semi-empirical dispersion potential into the conventional Kohn-Sham DFT energy [196, 197]. The two methods are implemented in popular DFT packages, such as Vienna *ab initio* simulation package (VASP) [198].

1.3 Outline

The layered materials and their artificial siblings hold the promises to solve various fundamental problems, such as energy harvest, energy storage, next-generation nanoelectronics, etc. [3] In order to fully utilize the unique properties and maximize the possible functionality of layered materials, two aspects of development are necessarily required: one is the large-scale fabrication of high-quality layered materials without defects, but with controllable thickness starting from the monolayer limit; the other is the realization of layered materials-based devices with desirable properties or phenomena. From the theoretical point of view, it will be quite contributing to figure out the formation mechanism of defects in growth, propose new fabrication approaches to achieve single-crystal structures, and understand the interfacial properties in device application, which involve contacts with each other in heterostructure or with other materials such as noble metal electrodes.

In the following chapters of this thesis, I will present several projects on the above topics. Chapter 2 is on the graphene growth on Cu(111) and Ni(111) substrates, including the understanding of GB formation in graphene and a proposal to suppress its creation (Sec. 2.1), comparison of the growth mechanisms of bilayer graphene growth on Cu(111) and Ni(111), and prediction of the critical size in the adlayer

graphene growth (Sec. 2.2). Chapter 3 is on the contrasting alignment of h-BN and graphene grown on Cu(100). Chapter 4 covers the tuning of properties of MoS_2 basal plane by metal attachment. At last, conclusions and perspectives of this thesis are presented in Chapter 5.

Chapter 2

Graphene Growth on Cu(111) and Ni(111) Substrates

2.1 Suppression of GBs in Graphene Growth on Superstructured Mn-Cu(111) Surface

2.1.1 Introduction

Graphene is a one-atom-thick flat sheet of carbon atoms packed into a honeycomb structure. Because of its superb mechanical, electronic, optical, and thermal properties [9, 142], graphene has limitless potential for future device applications. To fully realize the functionality of graphene, it is highly desirable to fabricate large-scale monolayer graphene with no or minimal structural defects. Among the different fabrication avenues being explored, epitaxial growth on transition metal substrates using hydrocarbon or other carbon sources stands out as a highly appealing approach [30–37, 199], especially on Cu surfaces [37]. Cu has the merit of low carbon solubility, which leads to a self-limiting growth process confined to its surface [38], and diverse carbon sources can be used to grow graphene on Cu substrates [200–202]. The relatively weak carbon-copper interaction compared to carbon-carbon

interaction enables fast diffusion of carbon atoms and efficient nucleation of carbon islands across the whole surface [39], indicating the feasibility of mass production of epitaxial graphene. Indeed, it has been reported recently that the single-crystal domains of monolayer graphene grown on Cu can reach the dimensions of 0.5mm on a side [40]. Furthermore, transfer of epitaxial graphene to other substrates can be readily achieved via chemical etching [41, 42].

However, one standing obstacle facing the community of epitaxial graphene on Cu is the prevalence of GBs undesirably introduced during growth [42, 129, 140, 141, 203–206]. A GB refers to the junction region of two crystalline grains with different orientations. The detailed atomic structures of the GBs in epitaxial graphene have been investigated extensively [42, 129, 140, 141, 204–206], and their presence has been shown to severely degrade the electronic, transport, and mechanical properties of graphene [42, 129]. Experimental efforts have also been made to suppress their creation during growth [40, 42, 207], but so far with limited success, partly because the underlying formation mechanism of the GBs is still unclear. Existing experimental observations suggest that the GBs can form in the initial nucleation stage when several graphene grains emanate from one nucleation site [129]; alternatively, they can be formed in the later growth stage when different graphene grains with relative misorientations coalesce [42, 200, 206].

In this section, we first demonstrate that, because of the inherently weak C-Cu interaction, orientational disorders of carbon islands on Cu(111) will be abundant in the early stages of nucleation and growth. Such disorders cannot heal themselves with the enlargement of the islands, leading to the prevalence of graphene GBs upon island coalescence. Based on this understanding, we propose to use a functionalized Cu(111) surface to lift the energy degeneracy in the early stages of nucleation and growth, thereby suppressing orientational disorders of the islands and the subsequent GBs. Our proposed kinetic pathway invokes the steps of "seed and grow" [208]. In the seeding step, carbon clusters are initiated by depositing coronene [209] on a $(\sqrt{3} \times \sqrt{3})$ R30° Mn-Cu(111) alloyed surface [210, 211], which effectively helps the

islands to select predominantly only one orientation on the superstructurally alloyed surface. In the growing step, larger, monolayer graphene is formed by conventional CVD.

2.1.2 Methods

Our DFT calculations are carried out using VASP [198] with projector augmented wave (PAW) potentials [212, 213] and the PBE-GGA [190] for the exchange-correlation functional. The lattice constant of Cu is obtained via structural optimization. The generic Cu(111) surface is modeled by a slab of 5 atomic layers, and the Mn-Cu(111) surface is realized by substituting Cu atoms by Mn atoms at ordered positions in the first layer. The vacuum layers are more than 13 Å thick to ensure decoupling between neighboring slabs. During relaxation, atoms in the lower 2 atomic layers are fixed in their respective bulk positions, and all the other atoms are allowed to relax until the forces on them are smaller than 0.01 eV/Å. A 2×2×1 k-point mesh is used for the 6×6 surface unit cell and 3×3×1 for the 4×4 surface unit cell [214]. The calculations with Mn atoms are spin-polarized. We consider the ferromagnetic configuration of the Mn-Cu(111) surface, because of the triangular arrangement of the Mn atoms. The binding energies are calculated as $\Delta E = E_{\text{adsorbate}} + E_{\text{substrate}} - E_{\text{adsorbate+substrate}}$.

2.1.3 Formation of graphene GBs on Cu(111) surface

Crystalline Cu has a face-centered cubic (fcc) structure, and its (111) surface exhibits a hexagonal packing of surface atoms. As shown in Figures 2.1a and b, both the Cu(111) surface and graphene have atomic arrangements with six-fold symmetry. Therefore, if carbon clusters nucleated at different sites are all oriented at the *same* high-symmetry orientation (HSO) of the Cu(111) surface (e.g., Figure 2.1c *or* d), their structural coherence will be ensured by the Cu substrate and there will be no GBs when they merge. However, when a simple six-fold symmetric carbon cluster

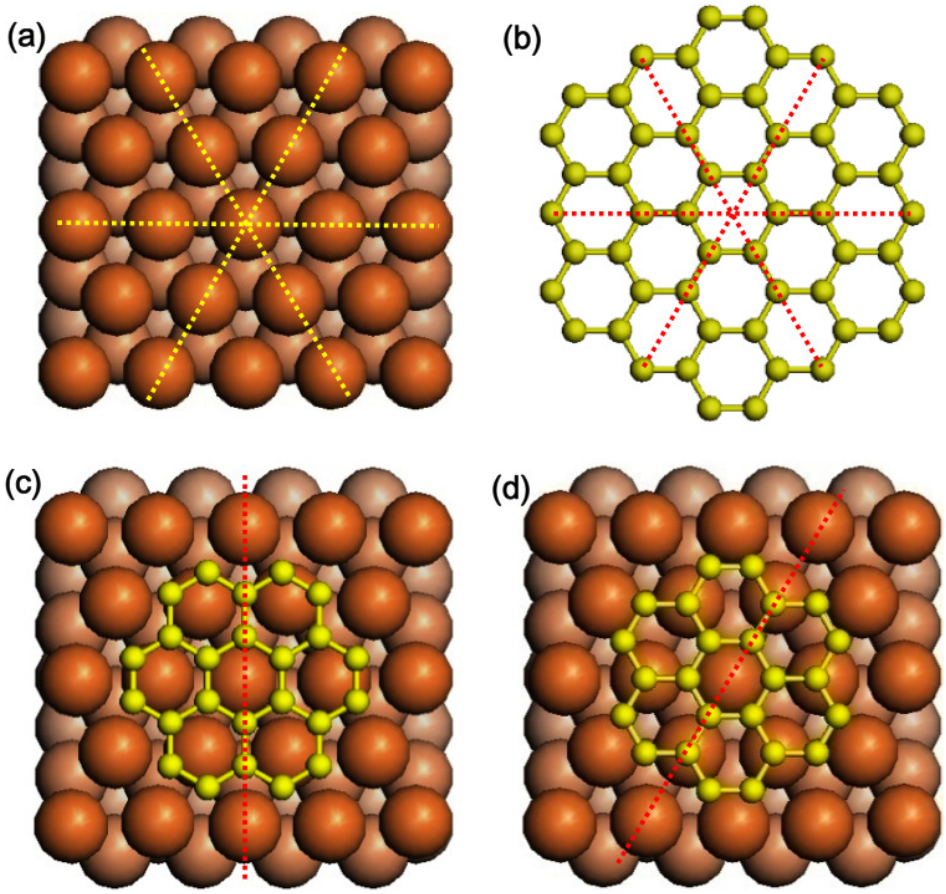

Figure 2.1: (a) and (b) Structural illustrations of the Cu(111) substrate and graphene, where the yellow and red dashed lines show their respective high-symmetry axes. (c) and (d) Illustrations of two geometries where a 7CR carbon cluster is at a HSO on the Cu(111) surface. In (c), the edge C atoms reside at the 3-fold hollow sites; in (d), the edge C atoms are at the bridge sites between two surface Cu atoms.

composed of seven 6-carbon rings (7CR) is placed on the Cu(111) surface, our detailed DFT calculations reveal that the energetically most stable geometry deviates from the HSO of Figure 2.1c by 11° (Figure 2.2b). We note that an earlier DFT study found that a C_{54} island was also located away from a HSO [215], and this result was soon discussed as a possible cause of domain misorientation and GB formation [216]. More accurate computations here indicate that such GBs may originate from even smaller, C_{24} clusters that deviate from HSO. The carbon cluster also has a dome-like structure (Figure 2.2a), with the central C atoms ∼2.30 Å from the Cu surface. Therefore, the cluster remains strongly bonded to the substrate only at the periphery while the interaction between the central C atoms and the substrate is rather weak, similar to the domed structure on Ir(111) [217]. Each of the 12 edge C atoms has two C neighbors, and prefers to reside at the bridge sites between two surface Cu atoms, because these edge atoms are closer to sp^3 hybridization than sp^2, thereby providing the driving force for the rotation of the island away from the HSO.

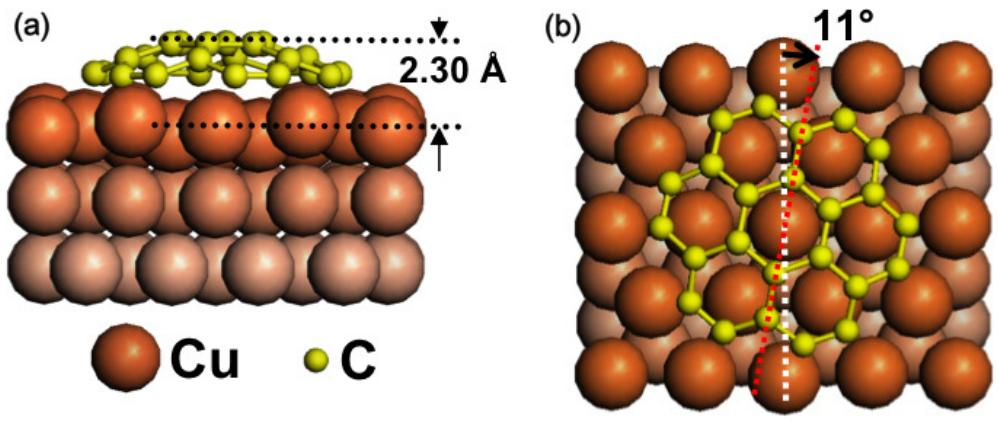

Figure 2.2: Side and top view of a 7CR on the Cu(111) surface, illustrating the domed nature (a) and the rotated nature (b) from the HSO of Figure 2.1c, respectively.

Now we go from the early stages of island nucleation and growth to island enlargement and coalescence. Since a small cluster such as the one shown in Figure 2.2 is not oriented at the HSO, there will be a degenerate mirror geometry with respect to the symmetry axis of Cu(111), indicating that islands with relative

misorientations can coexist. As a cluster grows larger, more edge C atoms will be involved in determining its preferred orientation by adjusting their bonds with the underlying Cu atoms. Therefore, there will be more nearly degenerate orientations, thus broadening the orientational disorder of the carbon clusters. When a cluster has grown large enough such that the edge atoms contribute only minimally to the total binding energy, the cluster is either still in an energetically stable orientation different from the HSO, or is too large to adjust its orientation to an energetically more favorable HSO. When two such clusters with a relative misorientation coalesce, a larger island containing a GB is formed, with a characteristic angle defined by the initial misorientations of the merging clusters and the local structural adjustment within the boundary [216]. This scenario is qualitatively consistent with existing experimental observations, and the detailed distribution of the GB angles may also depend on the specific growth conditions [129, 205, 206].

2.1.4 Suppression of GBs on Mn-Cu(111) surface

Next we search for ways to lift the energy degeneracy in island nucleation and growth via Cu(111) surface modification. Figure 2.3a illustrates a $(\sqrt{3} \times \sqrt{3})$ R30° X-Cu(111) superstructurally alloyed surface, which has transition metal atoms X substituting Cu at ordered positions. The choice of X is guided by the requirements that, (a) C binds more strongly to X than to Cu, so that the nucleated carbon clusters will prefer a HSO in maximizing their interaction with the X atoms; and (b) the alloyed X-X atoms are repulsive. As candidate systems, we find that a number of transition metals with unfilled d orbitals (X= Ru, Fe, Co, Ni, Mn) will bind more strongly with C [218]. We then compare the energies of different geometries where two such X atoms substitute two Cu atoms at the nearest-neighbor (NN) or next-nearest-neighbor (NNN) sites in the first layer of a Cu(111) surface. We find that, among all the transition metals considered, only the Mn atoms always stay mutually repulsive in the topmost Cu(111) surface, thereby ruling out clustering of

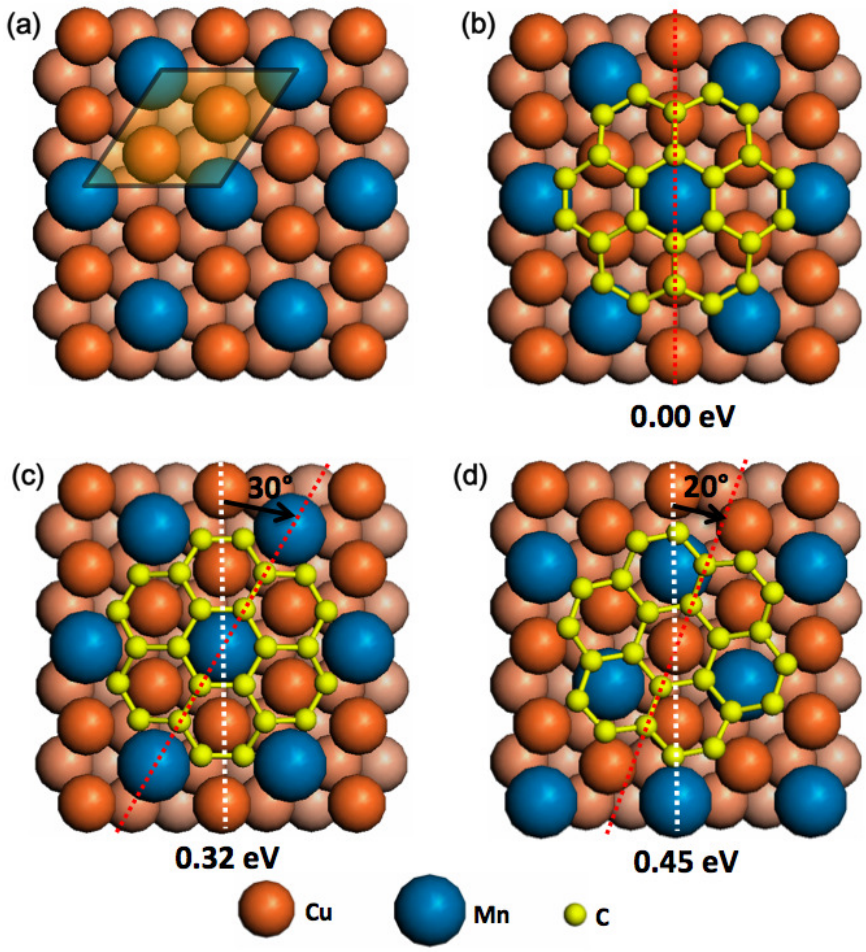

Figure 2.3: (a) Structure of the $(\sqrt{3} \times \sqrt{3})$ R30° Mn-Cu(111) superstructurally alloyed surface. (b-d) Three stable geometries of a 7CR adsorbed on the Mn-Cu(111) surface. As indicated by the red dashed lines, (b) and (c) illustrate two HSO configurations, while (d) is rotated from a HSO, and their relative stabilities are indicated by their total energy differences.

the alloyed Mn atoms. Separately, Bihlmayer, Kurz, and Blügel showed that, among the different compositions of Cu_xMn, the only thermodynamically stable configuration is the Cu_2Mn surface alloy at temperatures typical for epitaxial growth [211]. Taken together, these findings strongly support the feasibility of forming high-quality $(\sqrt{3} \times \sqrt{3})$ R30° superstructured Mn-Cu(111) surfaces. Indeed, experimentally the formation of a $(\sqrt{3}\times\sqrt{3})$ R30° superstructured Mn-Cu(111) surface has been observed at the Cu substrate steps [210], whereas the other metals only form islands or overlayers on Cu surfaces [219].

Still choosing 7CR as the testing baby graphene, we then calculate the total energies of 7CR with different orientations on the $(\sqrt{3}\times\sqrt{3})$ R30° Mn-Cu(111) alloyed surface. We find three stable or metastable configurations of a 7CR island through structural optimization, differentiated by placing the center of the 7CR above a Mn or Cu atom, as shown in Figure 2.3. Two of them (Figures 2.3b and c) are at HSO, but only the HSO in Figure 2.3b is the most stable, while the energy of the other two configurations is higher by 0.32 eV and 0.45 eV, respectively. Therefore, the Mn atoms alloyed into the Cu(111) surface indeed successfully help to pin the 7CR at the HSO. To see the underlying atomistic reason, we note that in all the three cases, the island has a dome-like geometry similar to that on a pure Cu(111) surface, indicating the predominant interaction with the substrate at its edge. Moreover, in the most stable configuration, the 7CR maximizes its contact with the Mn atoms at the periphery. The calculated binding energy per edge C atom of 7CR is 0.63 eV on Cu(111) and 0.89 eV on Mn-Cu(111).

To take advantage of the superstructural Mn-Cu(111) surface and effectively suppress the possible disorders induced in the initial nucleation process, we propose the use of coronene as a good candidate to seed the initial carbon clusters. As a polycyclic aromatic hydrocarbon, coronene [209] is just like the 7CR island, but with a hydrogen atom on each edge C atom. We have compared the dehydrogenation process of coronene to that of benzene, which has been used as carbon source to achieve low temperature graphene growth on Cu [202]. First, in gas phase, the C-H

bond dissociation energies of benzene and coronene are very close [220], as verified also by our present DFT calculations. Next, we consider the catalytic capability of the Mn-Cu patterned substrate. The energy difference between the initial state, where a coronene is adsorbed onto the Mn-Cu surface, and the final state, where all the edge hydrogen atoms are detached to form H_2 molecules, is 1.23 eV per H atom, which is to be compared with 1.39 eV for the case of benzene dehydrogenation on the Cu(111) surface. The relatively more stable final state is due to the enhanced binding of carbon clusters onto the Mn-Cu substrate than the Cu substrate. Therefore, from the energetic point of view, the alloyed surface would also be more catalytic in dehydrogenating coronene than Cu(111) in dehydrogenating benzene [202]. We therefore propose to use coronene as the first-step carbon source to seed carbon clusters on the patterned surface.

After the deposition and dehydrogenation of coronene on Mn-Cu(111) surface, all the adsorbed 7CR islands will have the same orientation. In particular, when two such 7CR islands coalesce to form a larger graphene cluster, no GB is formed (Figure 2.4). In order to achieve a continuous sheet of graphene, we invoke a second step of growth to supply C atoms to fill the openings between the carbon clusters. We notice that, in contrast to Cu(111), on which C adatoms are energetically much more favorable to nucleate than to stay apart [39], here on Mn-Cu(111) the carbon adatoms are less strongly inclined to nucleate. The energy difference between a C dimer and two C monomers on the substrate, calculated as $\Delta E = E_{\text{monomer+substrate}} \times 2 - E_{\text{substrate}} - E_{\text{dimer+substrate}}$ is 2.92 eV on Cu(111) and becomes 1.70 eV on Mn-Cu(111). Therefore, the conventional CVD growth using methane or ethylene could be applied here to supply carbon adatoms to diffuse and attach to the nearby coronene-seeded and correctly-oriented carbon islands (Figure 2.4), rather than to nucleate new islands, which is similar to the enhanced layer-by-layer growth of Ag on Ag(111) via a two-step kinetic pathway [208]. Eventually, the 7CR-seeded islands will be enlarged and connected to achieve a single-crystal graphene sheet with no or greatly suppressed GBs.

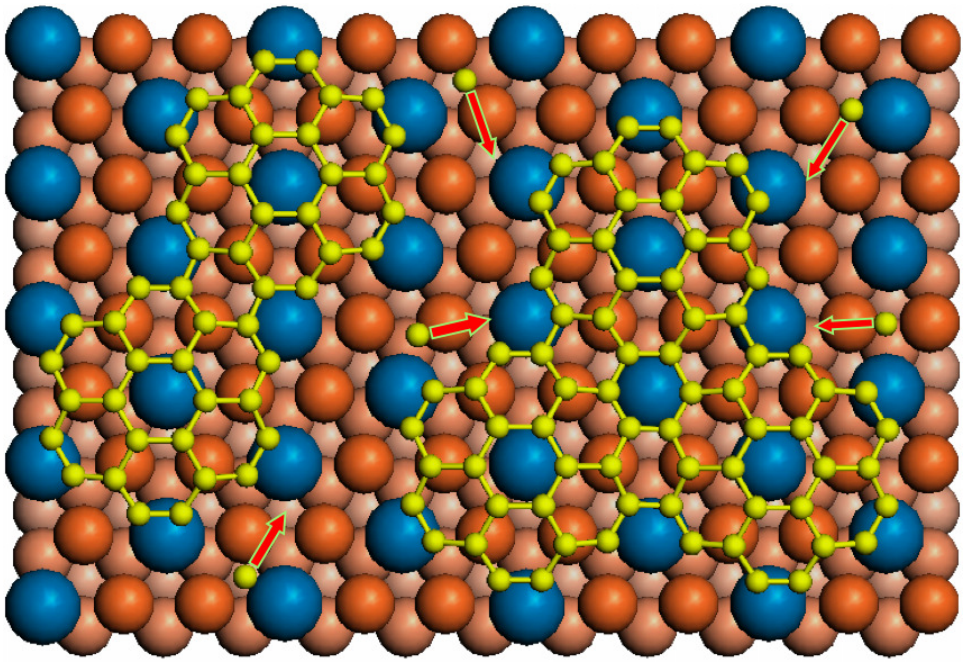

Figure 2.4: Enlargement of coronene-seeded carbon islands via conventional CVD growth. The individual C adatoms supplied in the second step of the "seed and grow" kinetic pathway diffuse and attach to the nearby islands to fill the opening spaces, resulting in a larger graphene sheet with no GBs.

2.1.5 Discussion and conclusion

It is important to note that, when a 7CR seed grows larger, the carbon clusters will still be at or close to the HSO, because an edge C atom prefers to reside at the bridge site between a Mn and a Cu atom. Because all the islands have nearly the same orientation and dome-like geometry, they will be able to make minimal local adjustments when they meet, and coalesce to form a single larger graphene sheet without GBs. Because of the lattice mismatch and its stronger interaction with the Mn-Cu(111) surface than with pure Cu(111), graphene may have a corrugated geometry, similar to that on Ru [221]. Finally, the playground of using patterned substrates is not necessarily limited to the Mn-Cu(111) surface; other superstructured surface alloys with different transition metals beyond the ones already considered here are also worth exploring. The present study of graphene growth on patterned substrates via a two-step kinetic process thus opens the door towards a new and viable approach for mass production of single crystalline monolayer graphene.

In conclusion, employing DFT calculations, we first identify that the misorientations of carbon islands nucleated on a Cu(111) surface lead to the formation of GBs as the islands coalesce. We then propose a two-step kinetic pathway to effectively suppress the formation of GBs. In the first step, large aromatic hydrocarbon molecules are deposited onto a $\sqrt{3} \times \sqrt{3}$ superstructured Cu-Mn alloyed surface to seed the initial carbon clusters of a single orientation; in the second step, the seeded islands are enlarged through normal CVD of methane to form a complete graphene sheet. The present approach promises to overcome a standing obstacle in large scale single-crystal graphene fabrication.

2.2 Contrast Mechanisms of Graphene Bilayer Growth on Cu(111) and Ni(111)

2.2.1 Introduction

Graphene has drawn tremendous research attention since its first experimental achievement by mechanical cleavage [9, 18]. To overcome its crucial shortcoming of band gap absence, bilayer or multilayer graphene has been proposed to open a tunable band gap and integrated to achieve applicable electronic devices, such as FETs [6, 222–224]. Therefore, it is highly desirable to acquire graphene with high-quality and controllable thickness. With remarkable success of large-area fabrication and easy transfer to other substrates, epitaxial growth of graphene on metal substrates outstands as an appealing approach, especially on Cu surfaces [36, 37]. Due to the low carbon solubility in Cu, the CVD growth of graphene on Cu substrates is considered as a self-limiting process confined to the surface only, resulting in graphene films of best quality over those achieved on the other metal substrates, but with predominantly only single layer. This growth mechanism of surface adsorption, in contrast to the segregation and precipitation growth of multilayer graphene on Ni, is also established by experiments using carbon isotope labeling method in a comparative study [38].

To achieve bilayer or multilayer graphene on Cu substrates, there have been two major attempts on the experimental side. One is to use Cu-Ni alloy as the catalytic substrate, instead of pure Cu, to increase the carbon solubility in bulk and enable the carbon segregation or precipitation [225–228]; the other is to substantially broaden the area of second-layer graphene on Cu by modifying the traditional growth procedures or conditions, such as substrate temperature, cooling rate, or gas pressure [229–234]. Despite these progresses made in experiments, rather than the widely-accepted surface adsorption growth of the first layer, the essential mechanism of adlayer graphene growth on Cu is still under debate, because of the divergences between reported observations: Kalbac et al. think that the second layer grows on top of the first

layer [231]; Nie et al. and Li et al. claim that the carbon species diffuse between Cu surface and the first graphene layer, then nucleate and grow adlayer at the interface [232, 233]. These physical pictures consider carbon behaviors only above the Cu surface, that completely disregard the subsurfaces of metal substrates. On the contrary, there exist strong indications of dissolution of carbon into Cu subsurfaces, and its significant interplay with the surface Cu atoms [234, 235]. A recent theoretical study [236] revealed the significant role of hydrogen in growing bilayer graphene, by investigating the behaviors of carbon monomers on the surface and in the first subsurface layer of Cu substrate. However, comprehensive theoretical examinations, including deeper subsurface sites and more kinetic processes, and more importantly on the nucleation behaviors of the second-layer graphene growth, from a carbon dimer to a compact island, are still necessary to nail down the growth mechanisms of bilayer graphene on Cu. Meanwhile, such considerations on Ni could provide an atomic-scale understanding of the experimentally discovered mechanism [38], and represent metals of high carbon solubility and stronger interaction to carbon, in comparison to Cu.

In this section, we first model the interfaces between a graphene overlayer and the Cu(111) or Ni(111) surface, with vdW interactions included. Within this framework, we extensively explore the adsorption and diffusion of carbon species in the metal-graphene systems, followed by the nucleation behaviors of a carbon dimer. We show that the existing graphene overlayer affects carbon adsorption and diffusion differently on the Cu and Ni substrates, as a result of the contrasting bonding nature of Cu-graphene and Ni-graphene. Meanwhile, nucleation of a carbon dimer under the first layer is proven to be much more effective on Cu than on Ni, thus providing physical origins to the different growth mechanisms of adlayer graphene. Based on results of thermodynamics and kinetics, we develop rate equations to analyze the second-layer graphene growth on Cu, and predict the critical size of the first layer for the nucleation of a compact island underneath. More importantly, we propose ways to substantially enhance the growth rate of the second layer, and point out the "inverse"

effect of "Ehrlich-Schwoebel (ES) barrier" [237, 238], which is beyond the traditional multilayer growth of thin films.

2.2.2 Methods

In our studies, we perform DFT calculations using VASP [198], with PAW pseudopotentials [212, 213] and GGA [190] for the exchange-correlation function. DFT-D2 [197, 239], a semi-empirical approach is used to include the vdW interactions. The lattice constants of metals are obtained via structural optimization. The metal (111) surfaces are modeled by slabs of five atomic layers, and the metal-graphene systems are modeled by placing a graphene overlayer on top of the metal surfaces. The vacuum layers are thick enough to ensure decoupling between neighboring slabs. During relaxation, atoms in the lower two atomic layers are fixed in their respective bulk positions, and all the other atoms are allowed to relax. A $3\times3\times1$ k-point mesh is used for the 3×3 surface unit cell of metals [214], similar to the setup in the previous studies of Ni systems [240, 241]. All the calculations are spin-polarized. We use the climbing image nudged elastic band (CI-NEB) method [242] to determine the energy barriers of carbon diffusion processes, with three to five intermediate images constructed along each pathway.

To investigate the growth mechanism of bilayer graphene, we first model the interfaces of a single-layer graphene adsorbed on metal substrates. Due to the small lattice mismatch between graphene and Cu(111), or Ni(111) [226, 243], as same as previous treatment [161, 244], we choose 3×3 graphene supercell, with the lattice length slightly stretched to match with the metal supercells (see Figure 2.5a). Regarding the description of interactions between graphene and Cu, or Ni, dispersion forces are quite important when exploring layered materials [243]. A previous study using vdW density functional (vdW-DF) [194, 245] method reports failure of predicting the metal-graphene spacings[244]; therefore, here DFT-D2, another approach to include the vdW correction is used here, and the results are quite

physical and also consistent with available experimental data. In particular, among the translational positions, the calculations show that graphene overlayer prefers to stay on Ni(111) surface with half of the carbon atoms on top site of the topmost Ni atoms, and the other half at the fcc hollow site (above Ni atoms in the third surface layer, which is labeled as "C" in Figure 2.5), and the spacing between graphene and Ni(111) is found to be 2.08 Å, in a perfect match with experiments [246]. For graphene on Cu(111), we find graphene to be located at the same translational position as graphene on Ni(111), and predict the spacing to be 2.91 Å. Experimentally there is no direct measurement of the spacing, and the interaction is determined to be weak [244]. Our calculation on Cu-graphene is physical because it shows the feature of much weaker interaction than Ni-graphene, and also the spacing is smaller than a previous DFT result of 3.26 Å [161], which predicts no band gap opening of graphene, but in conflicts with later experiments [247].

2.2.3 Adsorption and diffusion of carbon monomers

Given the interfacial structures, we then explore the presence of methane or other forms of carbon sources at the metal-graphene interfaces. When we place a methane molecule between Cu surface and graphene, the graphene overlayer is shifted up by more than 3 Å. For other decomposed methane molecules, CH_x ($x = 1, 2, 3$), they interact with Cu by forming C-Cu bonds, and the hydrogen atoms orient towards the graphene overlayer, interacted by vdW forces. The calculations show that all the CH_x molecules enlarge the Cu-graphene spacing to be more than 4.25 Å, while a single C adatom in-between does not change the original Cu-graphene distance of about 2.91 Å. Besides the necessarity of relatively large room between Cu and graphene for CH_x ($x > 0$) molecules to stay, as we learned before, the graphene edge usually forms stronger bonding with metal substrates than the graphene overlayer [217, 236, 248, 249], providing even more limited space for molecule incorporation; accordingly, the picture of CH_x ($x > 0$) molecules diffusion at interfacial region through graphene

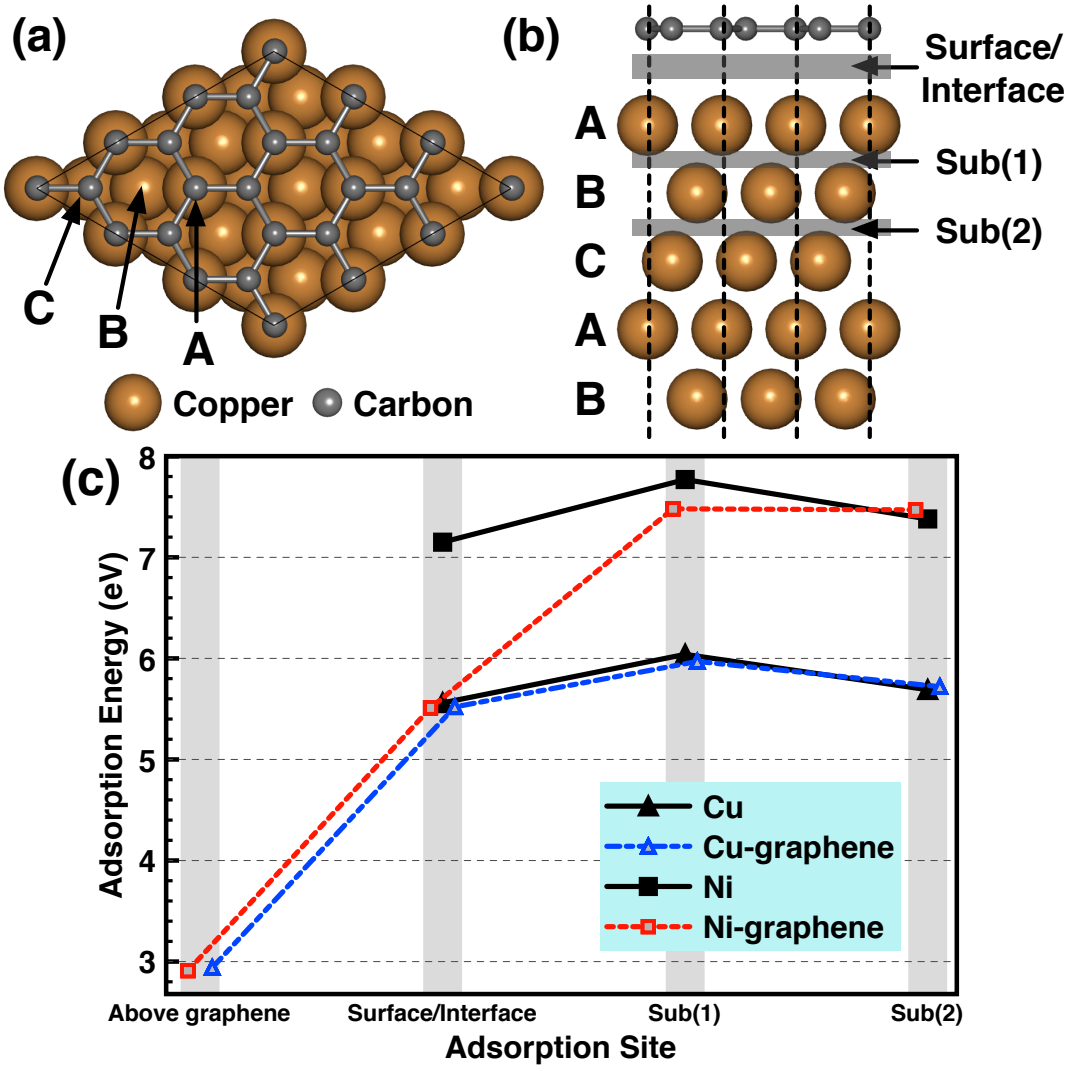

Figure 2.5: (a) Top and (b) side views of monolayer graphene on the Cu(111) or Ni(111) substrate, with half of the carbon atoms positioned on the top of metal atoms and the other half on hollow sites. The ABC stacking of (111) surface layers are labeled in both plots. The surface (without graphene adsorbed) or interface (with graphene on top) regions, and the first and second subsurface layers (represented by Sub(1) and Sub(2)) are indicated by arrows in (b). (c) The adsorption energies of carbon atoms located at different sites at the interface, surface, or subsurfaces of Cu(111) and Ni(111), in the cases with and without an existing graphene overlayer covering. We slightly shift the curves of Cu-graphene and Ni-graphene horizontally for clarify purpose.

edge [233] may not be dominant. Due to the closer contact with graphene, the immobility of CH_x molecules at the metal-graphene interface remains valid for Ni. Therefore, we think that, instead of hydrocarbon molecules, carbon adatoms are the active species in the growth of second layer graphene at the interfaces [232].

Next we focus on carbon adatoms, and investigate the adsorption of carbon monomers in the metal and metal-graphene systems. As indicated in Figure 2.5b, we consider the regions of adsorption sites on the bare metal surface, on top of graphene adsorbed on metal, at the metal-graphene interface, and in the first and second subsurface layers. The explored surface/interface positions include fcc hollow, hcp hollow (above a metal atom in the second layer), bridge (between fcc and hcp), and top sites, and for the subsurface layers, we consider both tetrahedral and octahedral sites. By comparing the different sites in the same region, we find that on a bare Cu surface, carbon adatom prefers the fcc hollow sites; while on a bare Ni surface, it prefers hcp hollow sites. Once a graphene overlayer forms on the metal surfaces, either Cu or Ni, the interfacial carbon monomers are more likely to be at fcc positions. Because of more neighboring metal atoms to bond with and larger interstitial space to stay, the octahedral sites are always more preferred for carbon adsorption than the tetrahedral ones in the same subsurface layer.

To have a quantitative comparison between the stable positions at different regions, we calculate the corresponding adsorption energies, defined by $E_{ads} = E_{carbon} + (E_{metal} \text{ or } E_{metal/graphene}) - E_{total}$, and the results of the most stable structure at each region are summarized in Figure 2.5c. For bare metal substrates, because of more coordination to metal atoms and elastic relaxation of surface layers close to vacuum, both of the first and second subsurface layers provide more stable adsorption sites for carbon than the surface region, consistent with previous calculations [39, 240]. As to the effect of existence of graphene on the adsorption, we notice the previous report on Ni was obtained from weakly interacted Ni-graphene, and the graphene overlayer was artificially fixed at a large distance from Ni surface [240], which did not coincide with experiments [243]. In our framework with a more physical description

and treatment of the interfaces, we show that carbon monomers do not prefer to adsorb on top of graphene compared to other sites, indicating that the second layer, or multilayer growth should start below the existing graphene layers for both Cu and Ni [38, 232, 233]. Graphene on Cu has almost no influence on the carbon adsorption energies of the stable positions, due to the relatively weaker Cu-graphene interaction and larger interfacial space; on the other side, the stronger interaction and closer distance between Ni and graphene make the interfacial sites much less stable than a bare Ni surface. Unlike Cu-graphene, the first and second subsurface sites become equally stable in Ni-graphene, which may reflect the fact that much more carbon atoms dissolve into Ni bulk than Cu. Above all, our results clearly point out that the first subsurface layers serve the most stable sites for carbon adsorption in metal and metal-graphene systems, which should play an important role in the graphene growth processes, and the contrasting influence of graphene on the carbon adsorption at the interfaces implies a different growth mechanism of adlayer graphene between Cu and Ni.

The carbon behaviors in the Ni subsurface and bulk were known to be vital [38], while in the Cu subsurface, they were not emphasized as key factors in the growth mechanism of graphene on Cu surface. One of the most important reasons is the low carbon solubility in Cu, so that people assumed carbon sources cannot penetrate into Cu. However, we expect the first several layers of subsurface should behave quite differently from the bulk of Cu substrates. The subsurface layers are closer than bulk to the supply of carbon sources, and the subsurface Cu atoms are more flexible to undergo elastic relaxation for easier incorporation of carbon atoms [234]. Indeed, thermodynamically, our calculations on carbon adsorption already suggest that, Cu atoms in the topmost surface layer relax outward by about 0.2 Å, making carbon adsorption more comfortable in the subsurface, meanwhile providing driving forces to push the carbon adatoms from surface into subsurface. Nonetheless, the remaining puzzle is about kinetics; in particular, what are the energy barriers for carbon incorporation, and its diffusion in the subsurface region.

We then calculate the carbon diffusion barriers both within and between different regions. As illustrated in Figure 2.6a, we investigate the diffusion paths (1) on the surface (of bare metal substrate) or at the interface (of metal-graphene system), (2) from surface/interface to the first subsurface, (3) between two octahedral sites in the first subsurface, (4) from the first to the second subsurface, and (5) on the second subsurface. The relatives energies of the stable adsorption states and the transition states of the minimum energy path between them are plotted in Figures 2.6b-e, for each of the studied systems respectively. The total energies of carbon adsorbed on the surface or at the interface are set to zero as the reference points, and each number close to the saddle point gives the diffusion barrier of the path, whose corresponding number in Figure 2.6a can be found in the horizontal axis.

On the bare Cu(111) surface, the fcc hollow site is most stable, and the hcp hollow site is found to be a local minimum, which connects two fcc sites. The calculated diffusion barriers are 0.10 eV from fcc to hcp, 0.51 eV from fcc to the first subsurface, and 0.55 eV within the first subsurface, and further penetration from the first to the second subsurface layer needs to overcome a high barrier of more than 2 eV. When graphene is placed on Cu, we mentioned that in Figure 2.5c, adsorption energies at the fcc site, and the octahedral sites of the first and second subsurface layers do not change. However, this statement is not valid for the adsorption at hcp site, because the carbon atom at the interfacial fcc site actually directly bonds with an atom in the above graphene overlayer, while the hcp site faces the hollow position of graphene lattice. Therefore, the existing graphene overlayer enlarges the energy difference between fcc and hcp sites, leading to a larger diffusion barrier of 0.58 eV at the Cu-graphene interface, in which hcp site serves as a transition state. To penetrate into subsurface, carbon atoms diffuse from the interfacial fcc site to the octahedral subsurface position right below. The interaction between interfacial carbon atoms and the graphene overlayer causes the downward diffusion slightly harder, compared to the situation of bare Cu substrate. Meanwhile, consistent with a recent study [236], we find that with graphene on top, the energy barrier for hopping between octahedral

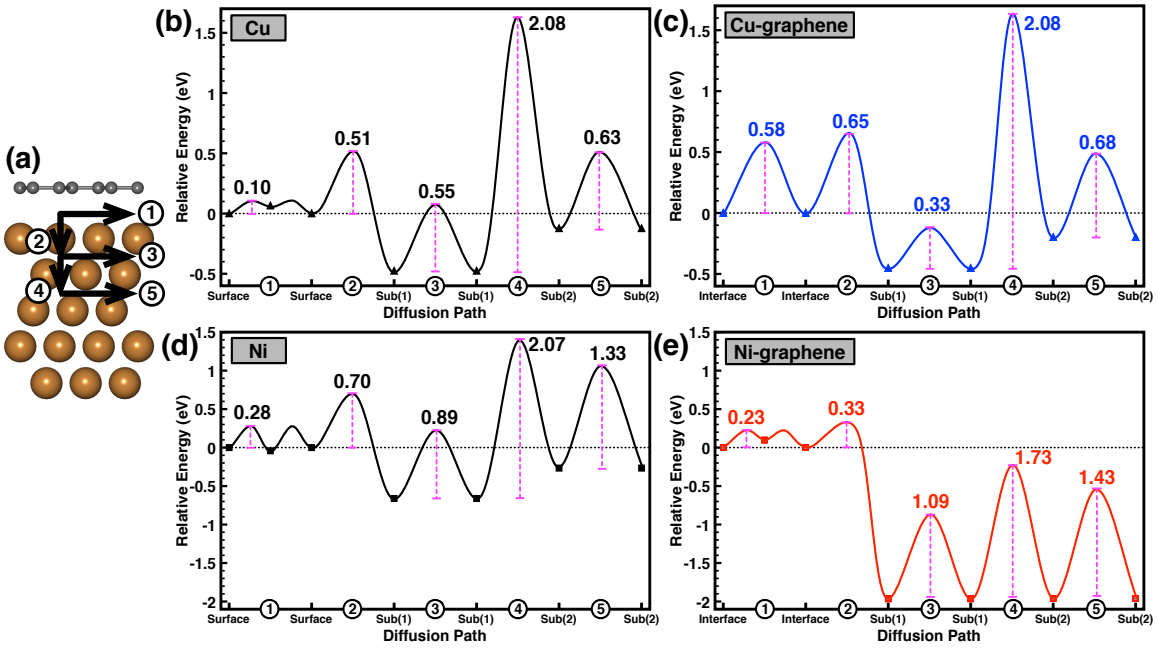

Figure 2.6: (a) Directions of carbon diffusion paths within and between different regions. (b-e) Relative energies of the initial, final, and transition states of the minimum energy paths in Cu (b), Cu-graphene (c), Ni (d), Ni-graphene (e) systems, respectively. The numbers in the horizontal axes correspond to the numbers in (a). The vertical dashed line measures the energy difference between initial and transition states, whose value is placed close to the saddle point.

subsurface sites in the first layer is decreased by 0.22 eV, thus becoming even smaller than the interfacial diffusion barrier. We then carefully compare the structures of the saddle points of the subsurface diffusion between bare Cu substrate and graphene-coved Cu surface. In fact, carbon diffusion within the first subsurface region results in a large displacement outwards of a surface Cu atom, and due to the relatively large Cu-graphene spacing, this Cu atom could steadily bond with a nearest carbon atom in graphene, without disturbing the other part of it. Therefore, the graphene overlayer stabilizes the saddle point of the subsurface diffusion by bonding with the Cu atom pushed outwards by carbon diffusion, and drags the carbon flow at the interfacial region, resulting in a faster diffusion path in the first subsurface than interface.

The horizontal diffusion paths 3 and 5 require the upward relaxation of surface metal atoms, while the downward paths 2 and 4 depend upon the horizontal expansion of the triangle formed by three close-packed metal atoms in the first and second topmost surface layers respectively. Generally speaking, Ni binds stronger to carbon than Cu, and Ni-Ni has a more robust metallic bonding than Cu-Cu, so that Ni surface allows less elastic relaxation. These bonding nature results in a higher diffusion barrier of each path in bare Ni substrate, excluding the nearly same values of path 4. This exception is probably because that the elastic stress due to diffusion is released without outward relaxation of surface atoms, and is dispersive owing to more coordination of metal atoms in the subsurface. When we deposit a graphene overlayer on top of Ni(111), they interact strongly, and the interfacial sites become quite unstable in thermodynamics, even though the diffusion barrier is found to be small. Graphene pushes carbon monomers into the subsurface, and kinetically facilitate easier diffusion of the downward paths 2 and 4. In contrast to Cu-graphene systems, the carbon mobility in the Ni first subsurface layer is decreased by graphene, because graphene already closely contacts with Ni surface atoms, thereby cannot further stabilize the outward relaxation of a single Ni atom.

2.2.4 Carbon nucleation in the second layer growth

Next we explore the formation of carbon dimers. Beyond the previous consideration on Cu and Ni surfaces [39], here we also take subsurface sites into account. For all the examined systems, we simply place two carbon atoms on the surface, or at the interface, and in the first subsurface region, separate them by varying distances, and compare the total energies (the most stable one is set to zero as the reference point for each plot). In Figure 2.7, the leftmost point of each curve corresponds to the formation of carbon dimer, except for the subsurface region of Ni-graphene, where carbon dimers cannot steadily exist. It should be noted that the rightmost point of each curve corresponds to the structure, in which the closest distance between carbon atoms in the neighboring supercells is about 4.5 Å, however, this should make minor effect on the energy preference of dimerization or separation in the curve. In the bare Cu substrate, unlike the preferred subsurface adsorption of carbon monomers, two carbon atoms effectively nucleate on the surface, with a quite strong C-C bond formed. Upon deposition of graphene on Cu, the interfacial nucleation is slightly less favorable than a subsurface dimerization. Indeed, carbon dimers in the subsurface deviate upwards from their original position, with one carbon at the height of topmost Cu layer. We therefore expect carbon atoms of more than dimer, will prefer nucleation at the interface than in the subsurface. The curves of bare Ni substrate and Ni-graphene system are quite similar, with graphene enlarging the energy difference between surface/interface and subsurface regions. Opposite to Cu, carbon atoms always urge to dissolute into Ni and stay separate in the subsurface or bulk. However, if confined to the surface or interface region, carbon sources tend to nucleate rather than being apart.

According to the above results, we now discuss about the growth mechanisms of bilayer or multilayer graphene on Cu and Ni substrates, comparatively. The formation mechanisms of the first-layer graphene are similar: on Cu, carbon atoms dissolve into the subsurface layers, and meanwhile effectively nucleate on the surface; on Ni, at

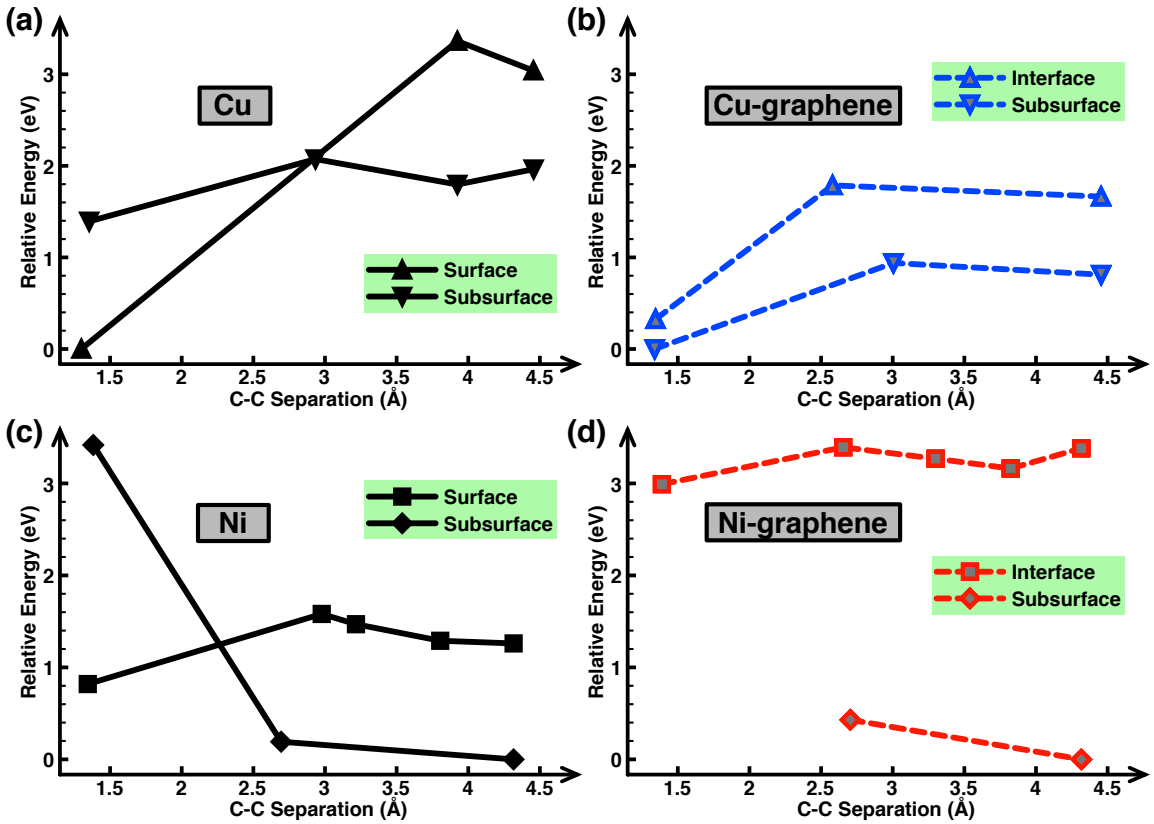

Figure 2.7: Relative energy vs. carbon-carbon distance in the surface/interface and first subsurface layer of Cu (a), Cu-graphene (b), Ni (c), and Ni-graphene (d) systems, respectively.

high growth temperatures, more carbon sources diffuse into Ni deeper layers, and excess carbon atoms steadily segregate from the substrate, and nucleate to form only one layer without a sharp change in temperature. The growth mechanisms of second-layer graphene are quite different on Cu and Ni: carbon adatoms stably adsorb and fast diffuse in the first subsurface layer of Cu, and then form the second layer at the interfacial region between Cu and the above graphene, although the nucleation is less effective than the first layer; while for Ni, the adsorption and nucleation behaviors of carbon atoms at the interface and subsurface cannot initiate the formation of second layer graphene. Only if the substrate temperature is dramatically cooled down, carbon sources precipitate from Ni due to decrease in solubility, and usually grow multilayer graphene below the existing first layer afterwards. The above pictures coincide with the established growth mechanism of graphene on Ni by previous experiments [38], and also provide atomic-scale evidence and understanding to the formation of adlayer graphene on Cu from below [232–234].

2.2.5 Prediction of the critical size of graphene for the second layer growth underneath

Now the question is how to grow uniform bilayer or multilayer graphene on Cu substrates, whose key point is to acquire carbon atoms under the first layer, because unlike growth on Ni, not enough sources are pre-dissolved into the Cu substrates. Next, beyond the nucleation of a carbon dimer, we investigate the dependence of the adlayer graphene growth on the size of the above layer, and provide possible solutions to enhance the enlargement of adlayers. We begin by considering an existing monolayer graphene island on the Cu surface, growing under a flux of hydrocarbon gas, catalyzed by the bare Cu atoms. With time, the external active carbon adatoms close to the edge can either be reflected away from the edge, attach to enlarge the first-layer graphene, or incorporate into the region under the first layer through its

edge. The accumulation of the carbon adatoms underneath will later results in the formation and growth of an adlayer graphene island.

We assume that the first-layer graphene has a circular shape as an approximation, with its periphery more strongly interacted with Cu than the center. Since covered by the first layer, the underneath region does not acquire carbon resources directly from the catalyzed flowing gas on top. The adatom density under the first layer, $\eta(r,\ t)$ (r is the distance from the center of the first-layer graphene), is defined as the number of adatoms per Cu surface cell of area a^2. The first-layer graphene edge is supposed to apply additional barriers to carbon penetration into the region under graphene, because the diffusing adatom is required to push related Cu atoms and Cu-bonded graphene edge together, which lead to the slow growth rate of the adlayer graphene. Meanwhile, the diffusion barrier of carbon in the first subsurface layer of graphene-coverd Cu substrate is as small as 0.33 eV, we therefore could safely assume that there is enough diffusion to maintain an even distribution of carbon adatoms under the first-layer graphene: $\eta(r,\ t) = \eta(0,\ t) = \eta(t)$.

At the boundary $r = R$ (R is the radius of the first-layer island), active carbon sources under the first-layer graphene ($r < R$) exchange with the external carbon adatoms ($r > R$). As we showed in Figure 2.5c, the graphene overlayer does not change the adsorption energies of the carbon adatoms. We therefore assume that the carbon exchange in both directions (in and out of the region under the first layer) endures the same effective barrier, as their initial and final states are equally stable in energetics. Per unit time, active carbon adatoms closest to the graphene boundary with distance Na (within $R - Na \leq r \leq R + Na$, N is an integer number) have a proportion of P to move towards or through the boundary, which means either attaching to enlarge the first layer or diffusing to the other side of the boundary.

Now we calculate the change in the adatom density $\eta(t)$ under the first layer ($r < R$). For the growth of the first-layer graphene:

$$\left(\frac{d[\pi R^2(t)]}{a^2 \cdot dt} = (\eta_{ext} + \eta(t)) \cdot \frac{P \cdot 2\pi R(t) \cdot Na}{a^2} \cdot (1-\alpha) \right) \Bigg|_{r=R}, \tag{2.1}$$

and for the carbon adatoms under the first layer:

$$\left(\frac{d[\eta(t) \cdot \pi R^2(t)]}{a^2 \cdot dt} = (\eta_{ext} - \eta(t)) \cdot \frac{P \cdot 2\pi R(t) \cdot Na}{a^2} \cdot \alpha \right) \Bigg|_{r=R}, \tag{2.2}$$

where η_{ext} is the external active adatom density on the bare Cu substrates, which depends on the growth conditions, such as substrate temperature, flux rate of hydrocarbon molecules, etc. Here we roughly choose a^2 as the surface area per carbon in graphene, due to the small lattice mismatch between graphene and Cu(111) surface. α is the probability that a carbon adatom which is around the graphene edge will diffuse to the other side of the boundary, other than attaching to the graphene island. A carbon adatom crossing the the first-layer graphene boundary, will endure an extra barrier by an amount E_e, than carbon diffusion towards the edge for attachment, whose barrier is E_d. Therefore,

$$\alpha = \frac{exp(-E_e/kT)}{exp(-E_e/kT)+1}, \tag{2.3}$$

where k is the Boltzmann constant.

To study the dependence of η on R, instead of time, we then calculate Eq.(1) / Eq.(2):

$$R\,\frac{d\eta}{dR} = 2\,(\frac{\eta_{ext}-\eta}{\eta_{ext}+\eta} \cdot \frac{\alpha}{1-\alpha} - \eta), \tag{2.4}$$

by integral, we get:

$$\begin{aligned} d\Bigg[& \frac{(c-b)-\sqrt{c^2+b^2+6cb}}{2} \ln\left(\eta + \frac{(c+b)+\sqrt{c^2+b^2+6cb}}{2}\right) \\ & -\frac{(c-b)+\sqrt{c^2+b^2+6cb}}{2} \ln\left|\eta - \frac{\sqrt{c^2+b^2+6cb}-(c+b)}{2}\right| - \ln(R^2)\Bigg] = 0, \end{aligned} \tag{2.5}$$

with $c = \eta_{ext}$, and $b = exp(-E_e/kT)$. We then define function:

$$f(\eta) = \frac{(\eta + \frac{(c+b) + \sqrt{c^2+b^2+6cb}}{2}) \frac{(c-b) - \sqrt{c^2+b^2+6cb}}{2}}{\left|\eta - \frac{\sqrt{c^2+b^2+6cb} - (c+b)}{2}\right| \frac{(c-b) + \sqrt{c^2+b^2+6cb}}{2}}, \tag{2.6}$$

assume that $\eta = 0$ at $R = R_0$, and determine the formula for the relation between adatom density η and radius R of the first layer graphene:

$$R = \sqrt{\frac{f(\eta)}{f(0)}} R_0. \tag{2.7}$$

The formula for the relation depends on two parameters: one is η_{ext}, which is mainly determined by the flux rate F of hydrocarbon supply, and in particular, $\eta_{ext} \approx k \cdot F$ before reaching its maximum value (k represents the catalytic capability of the Cu substrate over dehydrogenation of hydrocarbon molecules); the other is the additional barrier E_e of carbon diffusion through the first-layer graphene boundary. Next, we plot the dependence of η on R in Figure 2.8a at different values of parameters. We set $R_0 = 20$ Å as a reasonable value to begin with the investigation, $T = 1300$ K that is around the growth temperature of graphene, and the four curves in the figure correspond to $\eta_{ext} = 0.005$ (solid) or 0.05 (dashed), and $E_e = 0.3$ eV (blue) or 0.6 (red) eV, respectively. In all the curves, as R increases from R_0, η quickly accumulates from 0, and converges to different values, separately. At the same value of E_e, the smaller η_{ext} (solid lines) leads to faster increase in η at the very beginning, because of the slower growth of the first layer graphene island; however, the difference is negligible on the length scale of graphene growth. Meanwhile, the larger E_e curves (red) reach the converged values of adatom density (defined as η_{in}) faster, as η_{in} is relatively smaller.

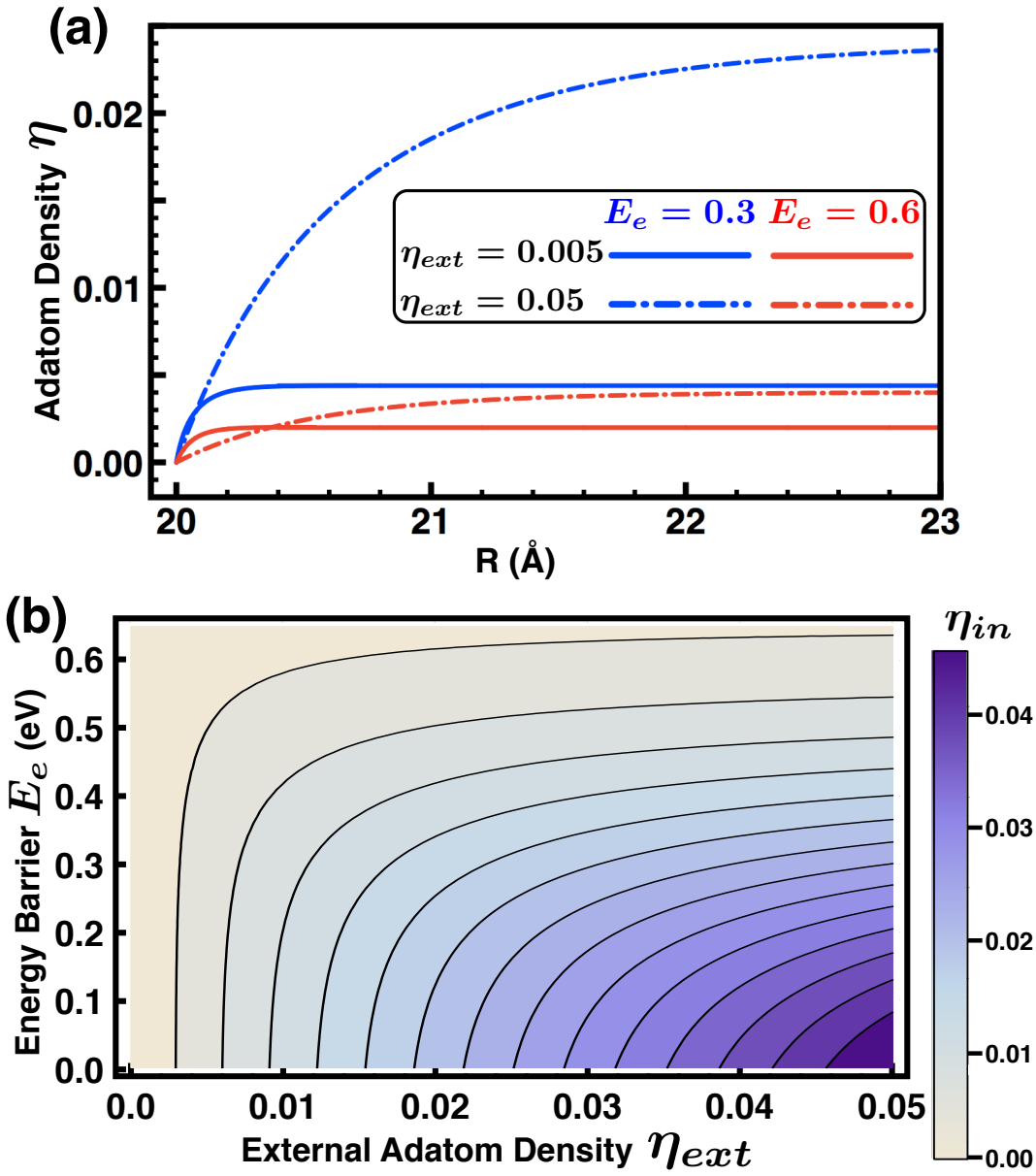

Figure 2.8: (a) The dependence of η on the radius R of the first-layer graphene island at $\eta_{ext} = 0.005$ (solid) or 0.05 (dashed), and $E_e = 0.3$ eV (blue) or 0.6 eV (red), respectively. (b) The contour plot of the dependence of the converged adatom density η_{in} on the external adatom density η_{ext} and the additional energy barrier E_e. The above results are all calculated at $R_0 = 20$ Å and $T = 1300$ K.

According to Figure 2.8a, and Eqs. (6) and (7), we can obtain the expression for the adatom density under the first-layer graphene at given growth conditions:

$$\eta_{in} = \left\{ \sqrt{\eta_{ext}^2 + [exp(-E_e/kT)]^2 + 6\eta_{ext}\, exp(-E_e/kT)} - [\eta_{ext} + exp(-E_e/kT)] \right\} /2. \tag{2.8}$$

The dependence of η_{in} on η_{ext} and E_e is illustrated in Figure 2.8b. As can be clearly seen, to maximize η_{in}, higher flux rate F should be employed to increase η_{ext}, and lower E_e is required. At relatively small E_e or large η_{ext}, the value of η_{in} changes sensitively to the other parameter. On the contrary, once E_e is larger than ~ 0.5 eV, or η_{ext} is smaller than ~ 0.01, η_{in} gets quite tiny, regardless of the other parameter. Therefore, both F and E_e should be properly chosen, to maintain adequate carbon supply for the second-layer graphene growth; obtaining a fairly negative effect from either parameter, the adatom density under the first layer will be close to zero. The reciprocal of temperature, $1/T$, has the same effect as E_e on η_{in}; hence a high temperature is also mandatory in the second-layer graphene growth, which gets consistent with the experimental setup [233].

Our previous studies [250] revealed that the critical size for 1D chain to 2D compact island transition on Cu(111) is $\sim$ 10 - 13 atoms. Next, we investigate the nucleation of a compact island of the second-layer graphene. The nucleation rate can be expressed [251] as: $\omega = \gamma a^{-4} D \eta_{in}^{\nu}$, where D is the surface diffusion coefficient, and ν is the number of carbon atoms in the smallest compact island stably exists. In our situation, $\gamma = \sigma_\nu\, exp(E_v/kT)$, in which σ_ν is the capture number within the range of 2 - 4 as an approximation [252, 253], and E_v is the energy difference between a compact island and a linear chain, both with ν carbon atoms. The surface diffusion coefficient depends on the diffusion barrier (E_{d_2}) under the first layer: $D = D_0\, exp(-E_{d_2}/kT)$, where D_0 generally lies between 10^{-2} and 10^{-3} $cm^2\, s^{-1}$ [23, 254, 255]. The rate that a compact island nucleates under the first-layer graphene then can be determined: $\Omega = \int_0^R \omega 2\pi r\, dr = \omega \pi R^2$.

We now roughly estimate the critical size R_c of the first-layer island, at which the probability to nucleate a compact island underneath Ω is close to 1. We choose $a \sim 10^{-10}\ m$, $T = 1300\ K$, $D_0 = 10^{-6}\ m^2\ s^{-1}$, $E_{d_2} = 0.33$ eV, $\sigma_\nu = 3$, $\nu = 10$, and $E_v \sim -1.5$ eV [250]. A recent study [236] reported $E_e = 0.64$ eV at the bare graphene edge, and when we set $\eta_{ext} = 0.03$ or 0.05, Ω is found to be quite small, and R_c is on the order of centimeter. This explains the fact that at traditional growth conditions, second-layer graphene is highly suppressed, and the graphene overlayer is single-layer dominated [37]. The value of η_{in} depends heavily on E_e; therefore, tuning E_e will effectively influence the nucleation rate of the second-layer graphene island. It was demonstrated that the passivation of hydrogen at the graphene edge will decrease E_e to 0.33 eV [236]. When we employ this value in the equation, R_c is estimated to be $\sim 10\ \mu m$ at $\eta_{ext} = 0.03$, and $\sim 2\ \mu m$ at $\eta_{ext} = 0.05$. Based on these rough estimations, we learn that the nucleation rate of a stable compact island under the first-layer graphene depends sensitively on the hydrocarbon flux rate F and the additional carbon diffusion barrier through the graphene edge E_e. In particular, higher F and smaller E_e will lead to faster growth of the adlayer graphene. Meanwhile, as discussed above, a high substrate temperature T is necessary to maintain enough carbon supply under the first-layer graphene.

2.2.6 Discussion and conclusion

During growth processes, as R expands, η rapidly converges to η_{in}, and the nucleation rate of a compact island increase quadratically. When R reaches close to R_c, a compact island forms, which is more probable to locate under the center of the first layer, because this spot exists longer than the other locations. After nucleation of the island, carbon adatoms will attach to its edge, same as the growth of the first layer. The carbon adatom density underneath is smaller than η_{ext}, but the diffusion barrier (0.33 eV) is smaller than that in bare Cu subsurface (0.55 eV); therefore, reducing E_e by decorating the edge of the first-layer graphene, and increasing the

flux rate F will possibly enable a comparable growth rate of the adlayer graphene as the first layer. The decoration of graphene edge to reduce E_e is not necessarily limited to hydrogen passivation; other elements or molecules are also worth exploring to further alter the growth rate of adlayer graphene, which should be addressed in a future study.

Before closing, it is important to emphasize that, here we exhibit a growth model of thin films that is counter to the conventional multilayer growth [251]. Traditionally, the higher the additional diffusion barrier at the step edge ("ES barrier" [237, 238]), the higher probability to nucleate the second-layer thin film on top; in our situation, the higher the edge additional barrier (E_e), the lower the growth rate of the adlayer graphene from underneath. Therefore, here E_e serves as an "inverse" ES barrier in the multilayer growth of graphene. The contrasting nature is due to the fact that, in traditional growth of thin films, the second layer forms on top, whose atom sources are directly deposited; while in the multilayer graphene growth, the adlayer acquires carbon adatoms by atom incorporation through the edge of the first-layer graphene.

In summary, we have investigated the thermodynamics and kinetics of carbon behaviors in the metal substrates, with emphases on understanding the growth mechanisms of bilayer or multilayer graphene on Cu and Ni. We show that the existing graphene overlayer affects carbon adsorption and diffusion differently on the Cu and Ni substrates, as a result of the contrasting bonding nature of Cu-graphene and Ni-graphene. Meanwhile, nucleation of a carbon dimer under the first layer is proven to be much more effective on Cu than on Ni, thus providing physical origins to the different growth mechanisms of adlayer graphene. Based on results of thermodynamics and kinetics, we develop rate equations to analyze the second-layer graphene growth on Cu, and predict the critical size of the first layer for the nucleation of a compact island underneath. More importantly, we propose ways to substantially enhance the growth rate of the second layer, and point out the "inverse" effect of "ES barrier", which is beyond the traditional multilayer growth of thin films. The present study presents a qualitative picture to explain the experimental

observations in bilayer graphene growth on Cu and Ni, and should be instrumental to the realization of large-scale bilayer graphene on metal substrates.

Chapter 3

Contrasting Alignment of h-BN and Graphene Grown on Cu(100) Surface

3.1 Introduction

Research on vdW heterostructures formed by stacking up various 2D crystals is an emerging field [3] because the numerous possible interfaces may lead to new physics not necessarily associated with the constituent 2D materials and, therefore, to novel applications. Most of the pioneering works on vdW heterostructures are based on mechanical transfer and placement of exfoliated 2D crystal flakes [96, 108, 256], where uncertainty in the orientational relation between layers is inevitable. For some purposes, e.g. to enhance graphene transport by placing it on h-BN [96], the orientational relation does not play a role. In other cases, however, the properties of the vdW heterostructures will be impacted. For example, Feenstra *et al.* predicted resonant tunneling in a graphene-insulator-graphene junction with orientationally aligned graphene sheets [257]. Although resonant tunneling has been experimentally demonstrated without orientational alignment [256], the reported current vs. voltage

characteristics differ from those predicted for aligned devices, exhibiting less sharp resonance peaks, a temperature dependence, and device-to-device variations. As another example, the band structure of graphene placed on top of BN, with new Dirac points induced by the superstructure periodic potential, is rotation dependent [108]. Therefore, a definitive orientational relation in a vdW heterostructure is necessary for certain desired physical properties to arise.

The only practical way to achieve certainty in orientational relation, i.e. orientational order, in vdW heterostructures is epitaxial growth. Actually, vdW epitaxy has been studied for decades as a method to overcome lattice mismatch [258, 259] enabled by the relatively weak and flexible vdW interactions between the epilayer and the substrate. Here, vdW epitaxy refers to the general case where a vdW gap [259] exists between the epilayer and the substrate, which can be a 3D crystal or a 2D sheet; we do not differentiate between epitaxy and quasiepitaxy [260]. Although vdW epitaxy is typically incommensurate, there can be orientational, or azimuthal, order [260], which has been observed in many examples of vdW epitaxy [103, 258, 259, 261, 262]. Recently, Yang *et al.* grew graphene on top of BN with orientational alignment and observed new Dirac points resulting from the fixed orientational relation [103], in contrast to the uncertainty inherent to the placement method [108]. In some cases, however, a definitive epilayer-substrate orientational relation is lacking [104, 263]. At the moment when vdW epitaxy is shaping into a new thrust area in 2D crystal research, it is imperative to uncover the mechanisms that determine the orientational relation.

Superficially, one would expect crystallography and symmetry similarities between the epilayer and substrate to be important, if not determining, factors to orientational alignment. Graphene has been grown with orientational alignment on closely lattice matched BN [103, 262]. Lattice constant mismatched transition metal chalcogenides are orientationally aligned to each other in vdW epitaxial heterostructures [259], presumably because they share the three-fold symmetry. In this chapter, we show that three-fold symmetric BN exhibits definitive orientational alignments when grown

on the four-fold symmetric Cu(100) surface. This is in stark contrast to the graphene/Cu(100) epitaxy, which exhibits a distribution of rotations [264], in spite of the close crystallographic similarity between graphene and BN. First-principles calculations reveal that the difference between the two systems arises from epilayer-substrate interactions.

It is conventional wisdom that, in epitaxy, strong epilayer-substrate interactions will enhance registry, which naturally leads to orientational alignment between the epilayer and the substrate. We show here that, in vdW epitaxy, where the epilayer-substrate interaction is of the vdW nature, stronger epilayer-substrate interactions may lead to reduced orientational alignment. This surprising finding sheds light on the determination of orientational relation in vdW epitaxy of 2D materials.

3.2 Methods

3.2.1 Experiment

Synthesis and transfer

BN crystallites were grown by APCVD on 25 μm thick Cu foils (Alfa Aesar, # 46986), which were sequentially washed by dilute nitric acid and deionized water, dried by a N_2 gun, and immediately loaded into the furnace. For growth on oxygen contaminated foils, the foils were kept in air for more than one day before loading. Prior to the growth, $H_3N{-}BH_3$ was loaded in a boat located in the upstream region of the tube. The furnace was gradually heated to 1050 °C over 60 min in Ar:H_2 (400 sccm : 100 sccm), followed by annealing at the same temperature and gas flow rates for 10 min. To start the growth procedure, BN precursor was heated to sublime at $\sim$ 120 °C by a heating tape wrapped around the tube. The typical growth time was 10 to 30 min, followed by rapid cooling.

The electrochemical polishing treatment was accomplished in a homemade electrochemial cell using orthophosphoric acid electrolyte and a Cu cathode. A 2.0 -

2.5 V DC voltage was applied for 10 - 20 min. After polishing, the foils was washed by deionized water and dried by N_2.

BN crystallites were transferred on to TEM grids or other substrates for characterization. To facilitate the transfer, a thin layer of poly (methyl methacrylate) (PMMA, 2% in anisole) was spin coated on the Cu foil sample (4000 rpm. for 1 min), and the copper was etched away by floating the foil in a copper etchant (CE-100, Transene). The PMMA/BN membrane was transferred onto the surface of a 10% HCl solution to remove residual metal particles and then washed by deionized water several times. Finally, the film was scooped out by the desired substrate (Quantifoil TEM grid with 1.2 μm diameter holes from Ted Pella, SiO_2/Si, or optical quartz plate). The PMMA layer was removed by acetone vapor, followed by thermal annealing (350 °C for 2 hours in a Ar:H_2 forming gas).

LEEM and LEED characterizations

Copper foils with APCVD-grown BN domains were transferred through air into an Elmitec LEEM III instrument, where they were outgassed in ultrahigh vacuum at about 300 °C. Bright-field LEEM images were formed from the specularly reflected (00) beam. Micro LEED patterns were obtained from areas either 0.5 or 2 μm in diameter.

3.2.2 Theory

DFT calculations

The lattice constant of Cu was obtained via structural optimization. The generic Cu(100) surface was modeled by a slab of four atomic layers, and the BN or graphene clusters were placed on top of the metal surfaces. A vacuum region more than 11 Å was used to ensure decoupling between neighboring slabs. During structural relaxation, the atoms in the bottom two layers were fixed in their respective bulk positions, with all the other atoms fully relaxed until the force on any given atom is

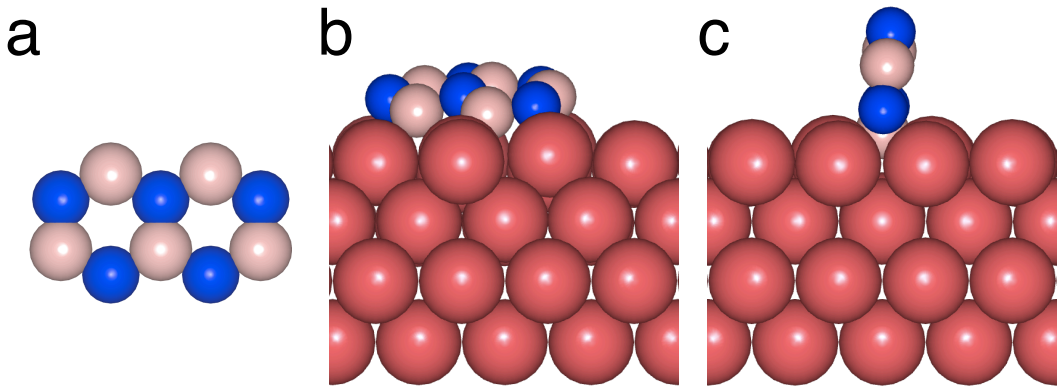

Figure 3.1: Structural illustrations of (a) a two-ring BN cluster, and clusters staying (b) planar (preferred when vdW is included) or (c) vertical (preferred without considering vdW) on the Cu(100) substrate.

smaller than 0.03 eV/Å. A $2 \times 2 \times 1$ k-point mesh was used for a 7×7 Cu surface unit cell. The effect of spin polarization was examined. As a sanity check, we first placed a two-ring BN cluster on Cu(100). The PBE approach led to an unphysical picture, where the cluster stands up on the surface. After the vdW interaction is included, the physically reasonable picture was arrived at (Figure 3.1).

3.3 Observations of BN Growth and Alignment

3.3.1 Monolayer BN single crystal growth

The Methods section describes the growth by atmospheric-pressure chemical vapor deposition (APCVD) on cold rolled copper foils. The wide thermal decomposition window and the violent decomposition behavior of the precursor ammonia borane ($H_3N{-}BH_3$) hinder the synthesis of monolayer BN crystallites with well-defined, energetically favored edges [43, 44]. We leverage the diffusion-limited kinetics of APCVD to achieve a low feedstock arrival rate, which was further controlled by the precursor charge. Analogous to graphene APCVD using highly diluted methane [42, 265], the method results in monolayer single crystals with energetically favored edges, commonly believed to be nitrogen terminated zigzag edges, and

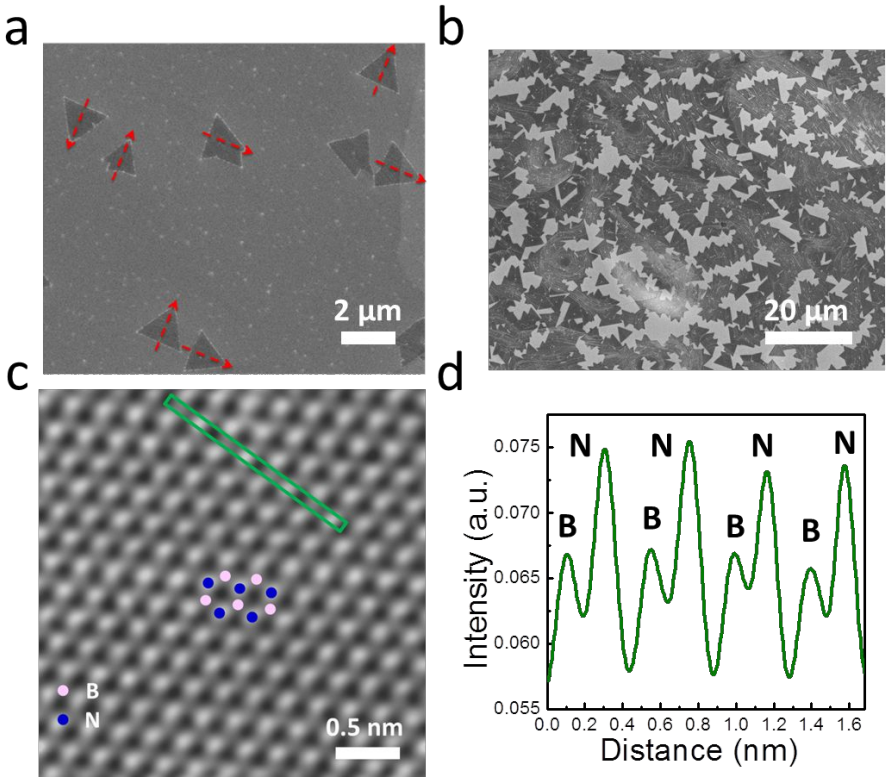

Figure 3.2: Monolayer BN crystals obtained by APCVD. (a, b) Representative SEM images of BN crystals on Cu foils with different film coverages. Spatially isolated equilateral triangles (a) and complex structures (b) are achieved by controlling the amount of precursor. Red arrows in (a) indicate orientations of crystallites. (c) Z-contrast ADF-STEM image of a BN crystallite, showing single layer character. Pink and blue circles denote B and N atoms, respectively. (d) Intensity profile along the green line in (c), identifying B and N atoms.

therefore exhibiting the distinctive equilateral triangle shape [44, 266] (Figure 3.2a). The scanning electron microscopy (SEM) image Figure 3.2a shows isolated, equilateral triangle-shaped BN domains grown with a low precursor charge. Arrows overlaid on the BN domains in Figure 3.2a suggest that these triangles are oriented only in several directions, a result that warrants an in-depth investigation. With increased precursor charge, crystallites coalesced into islands of complex shapes, such as butterflies and stars (Figure 3.2b).

Moreover, samples were characterized by X-ray photoemission spectroscopy (XPS) and UV-visible spectroscopy for chemical analysis and optical band gap

measurement, respectively. On the atomic scale, the element-contrast (Z-contrast) annular dark-field scanning transmission electron microscopy (ADF STEM) image and the corresponding intensity line profile (Figures 3.2c,d) show clear distinction between individual B and N atoms, which, considering the stacking of bulk h-BN [267], unambiguously confirm that the crystallites are monolayer.

3.3.2 h-BN on Cu(100): strict alignment

To understand the limited number of allowed orientations of the BN crystallites suggested by Figure 3.2a, low-energy electron microscopy (LEEM) and selected-area low-energy electron diffraction (μ-LEED) were performed to determine the relative crystallography of the BN domains on the Cu foil substrate. Every diffraction pattern acquired across millimeter length scales of the surface indicated a Cu(100) surface termination, consistent with the fact that the cold rolled Cu foil surface consists predominantly of large, (100)-oriented grains [264]. Figure 3.3a displays a representative μ-LEED pattern of a BN island, showing diffraction spots corresponding to Cu(100), BN, and a moiré formed between the BN and the underlying Cu(100). Since this pattern is rather complicated, we present a schematic illustration of it in Figure 3.3b. The four first-order diffraction spots of the Cu(100) surface lattice are marked by brown arrows in Figure 3.3a, and are colored brown in Figure 3.3b. Similarly, the six first-order diffraction spots corresponding to the BN overlayer are marked in blue. The moiré spots are circled and colored in green, and we note that many of the circles in Figure 3.3a contain two or three diffraction spots; these are represented by single green dots in Figure 3.3b. The BN island exhibits only one set of diffraction spots, which confirms its monocrystallinity. At the selected electron energy, the pattern in Figure 3.3a shows a clear three-fold symmetry: higher and lower intensity BN spots are marked by thicker and thinner blue arrows, respectively.

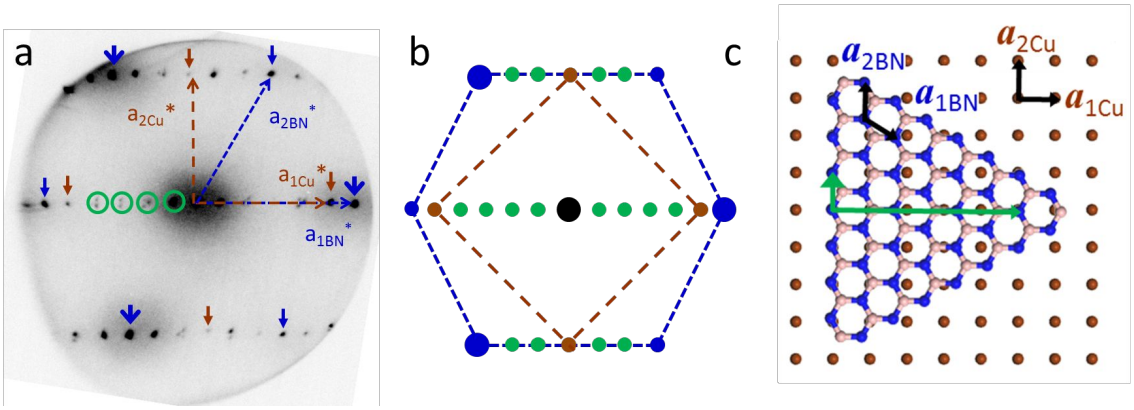

Figure 3.3: BN/Cu(100) Superstructure. (a) μ-LEED pattern (63 V) obtained on a triangular BN crystallite on a Cu(100) grain. First-order diffraction spots of Cu are marked by brown arrows, and the brighter and dimmer BN spots are marked by thicker and thinner blue arrows, respectively. Reciprocal primitive vectors of BN and Cu are drawn as blue and brown dashed arrows, respectively. Selected moiré spots are marked by green circles. (b) Schematic of the diffraction spots arising from BN and Cu. (c) Atomic model of BN on Cu(100) derived from the diffraction pattern. A superstructure cell, marked by green arrows, is formed between BN and Cu(100) lattices. The two lattices match well at spacings of 5 Cu cells or 6 BN cells. Lateral registry shown is arbitrary. Primitive vectors of the BN and Cu lattices are also shown.

To account for the moiré pattern, we first note that the overall diffraction pattern has two high symmetry directions: a horizontal direction with many closely spaced diffraction peaks from the superstructure (moiré); and a vertical direction where the separation between each of these rows of closely-spaced superstructure peaks is the Cu(100) reciprocal lattice constant. In the vertical direction, the vertical components of the BN and Cu(100) reciprocal lattices roughly align, i.e. $a^*_{Cu} \approx a^*_{BN}\sin 60^\circ$, where a^*_{Cu} and a^*_{BN} are the reciprocal lattice constants of the BN and the Cu(100) 2D lattices, respectively, leading to each Cu spot being collinear with a pair of first-order BN spots (blue). The close match between the BN and Cu(100) real-space lattice constants ($a_{Cu} \approx a_{BN} \approx 0.25$ nm) and the relationships $a^*_{Cu} = 2\pi/a_{Cu}$ and $a^*_{BN} = 4\pi/(\sqrt{3}\, a_{BN})$ explain this coincidence and why there are no moiré spots along the vertical direction. In the horizontal direction, the ratio of the Cu(100) to BN reciprocal lattice constants is very close to 5:6, which leads to a supercell that in real space is 5 times the Cu unit cell or 6 times the BN unit cell. In reciprocal space this match creates four moiré spots (marked by green circles) equally spaced at 1/5 the separation between the (00) spot and the first-order Cu spot, or 5 diffraction spots (including the first-order Cu spot) spaced at 1/6 the separation between the (00) beam and the first-order BN spot.

An atomic model (Figure 3.3c) is constructed based on these coincidences observed in the diffraction pattern: While $a_{Cu} \approx a_{BN}$ (within +2.1%) along the vertical direction, the supercell is 5 times the Cu unit cell or 6 times the BN unit cell projected along the horizontal direction, i.e. $5a_{Cu} \approx 6a_{BN}\sin 60^\circ$ (within −1.8%). We point out that this model is an illustration of the orientational relation and periodicity; any lateral translation is allowable. As a consequence of small lattice mismatches (+2.1% and −1.8% in the two directions), each moiré spot marked by a green circle in Figure 3.3a actually is comprised of three closely spaced spots.

Unlike the graphene/Cu(100) system [264], μ-LEED analysis on multiple BN crystallites surprisingly shows that only four equivalent orientations occur for BN on Cu(100), i.e., BN crystallites are well aligned to the underlying Cu(100) lattice.

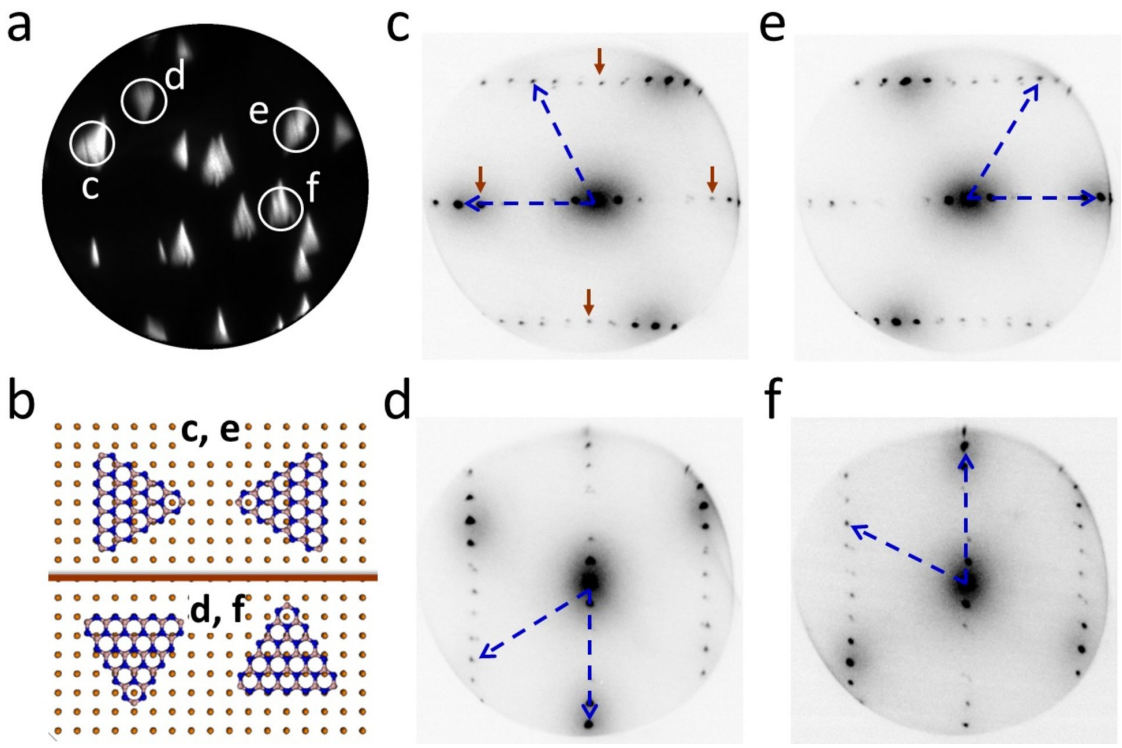

Figure 3.4: Alignment between BN crystallites and Cu(100) surface lattice. (a) LEEM image (25 V, 15 μm diameter field of view) of BN islands (bright) on a single Cu(100) grain. White circles denote regions where μ-LEED patterns (c-f) were obtained. (b) Real-space atomic model of four equivalent orientations of triangular BN crystallites on Cu(100). (c-f) μ-LEED patterns acquired at locations marked in (a). Blue arrows mark the reciprocal primitive vectors of BN. Brown arrows in (c) mark the first-order diffraction spots of Cu(100). The BN crystals exhibit 3-fold symmetry in the diffraction pattern at the chosen electron energy.

Figure 3.4a shows a bright-field LEEM image, where BN islands are imaged as bright triangular regions. The entire field of view is a single Cu(100) grain. Figures 3.4c-f displays μ-LEED patterns acquired on four BN islands that are circled and labeled in Figure 3.4a. These four diffraction patterns correspond to four orientations of the BN on top of the Cu(100) surface. In each pattern, one BN reciprocal primitive vector aligns with one reciprocal primitive vector of the Cu(100) surface. Thus, by symmetry there are four equivalent orientations of BN crystals on Cu (100). Furthermore, dark-field imaging of the same region imaged in Figure 3.4 shows that four and only four orientations account for all the BN islands in the entire field of view. Figure 3.4b schematically illustrates the four equivalent BN orientations in real space.

In Figure 3.5, we show another set of LEEM/LEED data with a better-resolved bright-field image, which reveals the equilateral triangle shape of the BN crystallites. (In Figure 3.4a the crystallites are incompletely imaged, possibly due to the non-planarity of the Cu foil.) The LEED patterns of Figure 3.5 more simply document the epitaxial relationships shown in Figure 3.4 since only the first-order Cu and BN diffraction spots are visible. In addition, these diffraction patterns together with the image (Figure 3.5a) allow us to confirm that the edge orientations of the BN triangles are indeed zigzag.

With the four allowed orientations accurately identified by LEEM and μ-LEED, SEM provides statistics over large areas. Figure 3.6a shows a representative SEM image of BN islands grown on an as-received Cu foil. The orientations of triangular crystallites are carefully examined and analyzed, exploiting the distinctive equilateral triangle shape and the fact that their sides are zigzag edges. Four and only four possible orientations are observed, in good agreement with the LEEM/LEED measurement. The uneven distribution between the orientations shown in the histogram (Figure 3.6c) may be due to the vicinal surface of the Cu grain. Interestingly, on electrochemically polished foils (Figures 3.6b,d) one orientation dominates, perhaps because the polishing resulted in a surface whose steps and terraces were preferentially aligned along one direction.

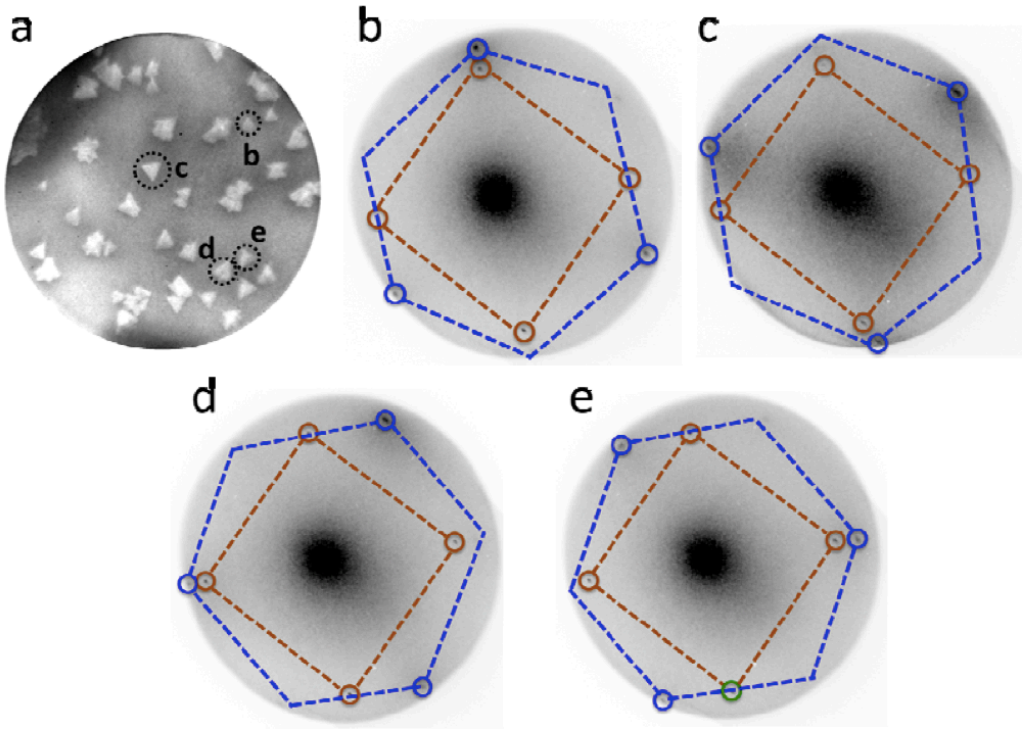

Figure 3.5: Additional LEEM/LEED characterization of BN/Cu(100) epitaxy. (a) Bright-field LEEM image (25 μm diameter field of view) showing the equilateral triangle BN crystallites. The four dashed circles mark the regions analyzed by μ-LEED in panels (b-e). (b-e) Corresponding μ-LEED patterns, showing the four equivalent orientations of BN islands. Only the first-order diffraction spots of BN and Cu are visible, which are blue and brown circled, respectively.

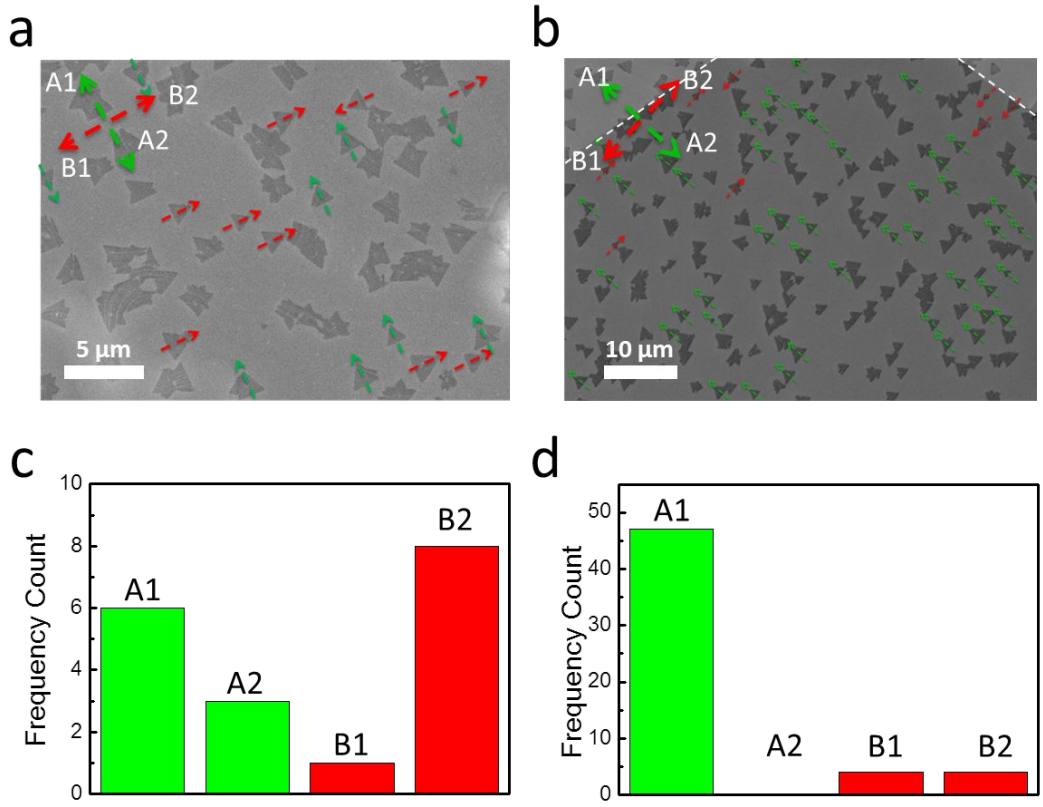

Figure 3.6: Statistics of BN/Cu (100) rotational orientations. (a,b) Representative SEM images of BN islands on (a) an unpolished Cu foil and (b) an electrochemically polished Cu foil. Four possible orientations of BN crystals are denoted A1, A2, B1, and B2 shown by legends. (c,d) Orientation histograms of triangular BN crystallites within individual Cu grains. Cu GBs are clearly identifiable in SEM, as delineated by dashed lines in (a) and (b).

3.3.3 Oxygen impurity induced misalignment

To further investigate the BN/Cu(100) orientational alignment mechanism, we grew BN on oxygen contaminated Cu foils without changing the recipe. In the LEED pattern (Figure 3.7a) acquired from a region free of BN, appear four diffraction spots that are not present in a simple Cu(100) surface. These additional spots are attributed to the c(2×2) reconstruction of Cu(100) caused by adsorbed oxygen [268]. We then placed the electron beam spot within individual BN islands to perform μ-LEED. Figure 3.7b displays a diffraction pattern obtained in one island, showing the Cu, BN, and c(2×2) reconstruction spots; some of the BN/Cu(100) moiré spots present in Figures 3.3 and 3.4 are faintly visible. More importantly, new moiré spots (circled in cyan) appear, corresponding to double diffraction from the c(2×2) and BN lattices. This moiré formed by the BN and the c(2×2) provides strong evidence that the oxygen impurity is underneath the BN island. Due to the oxygen, the BN crystallites no longer lock into the four aligned orientations on Cu(100). The large-area LEED pattern in Figure 3.7c shows multiple rotation angles on a single Cu(100) grain. This wide angular distribution, along with the weak BN/Cu moiré spots, again indicates that the intercalation of oxygen atoms between the BN crystallite and the Cu substrate weakens the interaction and therefore the alignment between the two lattices.

To obtain statistics of BN crystallite orientations on the oxygen-contaminated Cu(100) surface, we obtained LEED patterns by moving a 2 μm diameter electron beam in 10 μm steps over a distance of 1.25 mm. The angle between each diffraction spot of the BN domains and one Cu(100) spot was measured for each pattern. Figure 3.7d displays a histogram of the rotation angles. This histogram does not distinguish between BN domains that have an antiphase (twin) relationship. We also examined an SEM image (Figure 3.7e) of a similar sample and obtained orientation statistics (Figure 3.7f). These histograms show that BN crystallites still prefer the aligned orientations, but exhibit a distribution of rotations. This observation provides

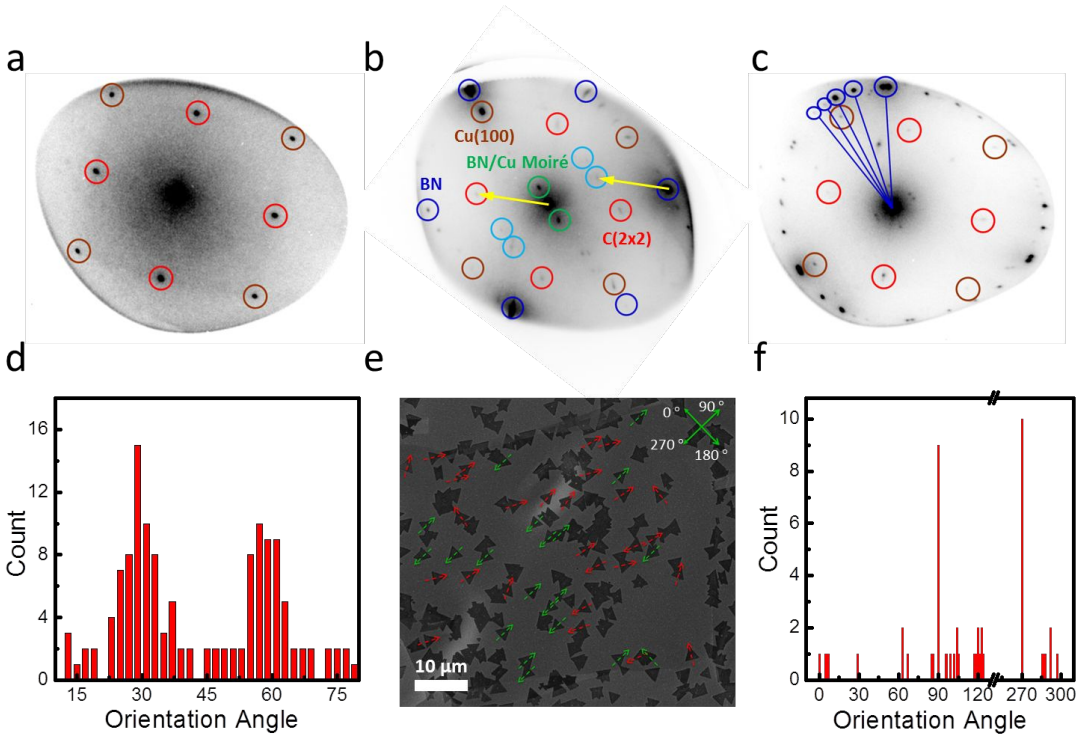

Figure 3.7: Oxygen impurity induced misalignment. (a) Selected-area LEED pattern of a BN-free region of an oxygen-contaminated Cu foil, showing Cu(100) (1×1) and c(2×2) spots, distinguished by brown and red circles, respectively. (b) μ-LEED pattern from a single BN island. The blue circles indicate the first-order diffraction spots from BN. Moiré diffraction spots (circled in cyan) due to multiple scattering by a c(2×2) and BN reciprocal lattice vectors (as exemplified by yellow arrows) prove the presence of oxygen impurity underneath the BN. BN/Cu(100) moiré spots are circled in green. (c) LEED pattern with multiple sets of BN diffraction spots, highlighted by blue circles, which reveal the misalignment of BN grains on the O/Cu(100) surface. (d) Histogram of angles between BN diffraction spots and a Cu(100) spot in a 60° range. (e) Representative SEM image of BN islands grown on oxygen-contaminated Cu foils. (f) Orientation angle histogram of triangular BN domains marked in (e), showing a random distribution of BN orientations.

strong corroborating evidence that the BN-Cu interaction is essential for the observed alignment of BN on pristine Cu(100).

3.4 Energy Dependence on the Rotation: h-BN vs. Graphene

To understand why BN rigorously aligns on Cu(100) while graphene does not, we performed a comparative DFT study to calculate the total energy vs. rotation angle of BN and graphene clusters on Cu(100) (Figure 3.8), which simulate the initial nucleation stage [248, 249]. We used VASP [198] with PAW pseudopotentials [212, 213] and the PBE-GGA [190], as well as DFT-D2, a semi-empirical approach that includes vdW interactions [197, 239]. The investigated structures were first relaxed using PBE-GGA functionals without vdW interactions to search for stable or metastable geometries around initial translational positions and rotational orientations, followed by DFT-D2 calculations for a second-step relaxation.

The relaxed BN cluster exhibits a domed structure, similar to graphene clusters on Cu(111) and Ir(111) [217, 248], indicating that the cluster interacts with the substrate predominantly at the periphery. Due to the three- and four-fold symmetries of BN and Cu(100), respectively, a rotation angle $\theta = \Theta$ is equivalent to $\theta = \Theta + 30°$. Meanwhile, due to reflection symmetry, the total energy $E_{total}(\Theta) = E_{total}(-\Theta)$. Therefore, we only need to consider $\theta \in [0°, 15°]$, and thus set the initial rotational angles to be $\theta = 0°, 5°, 10°$, and $15°$. Figure 3.8a shows two of the stable or metastable geometries after relaxation by DFT-D2, $\theta = 0°$ and $6.2°$. Figure 3.8b displays the total energy vs. rotation angle plot for all the stable/metastable configurations discovered by relaxation using PBE and DFT-D2. The total energy at $\theta = 0°$ was set to zero as the reference for both methods, which resulted in the same trend, suggesting that the effect of the net corrections due to vdW interactions between the cluster and the Cu substrate is quite close for all orientations and therefore plays a

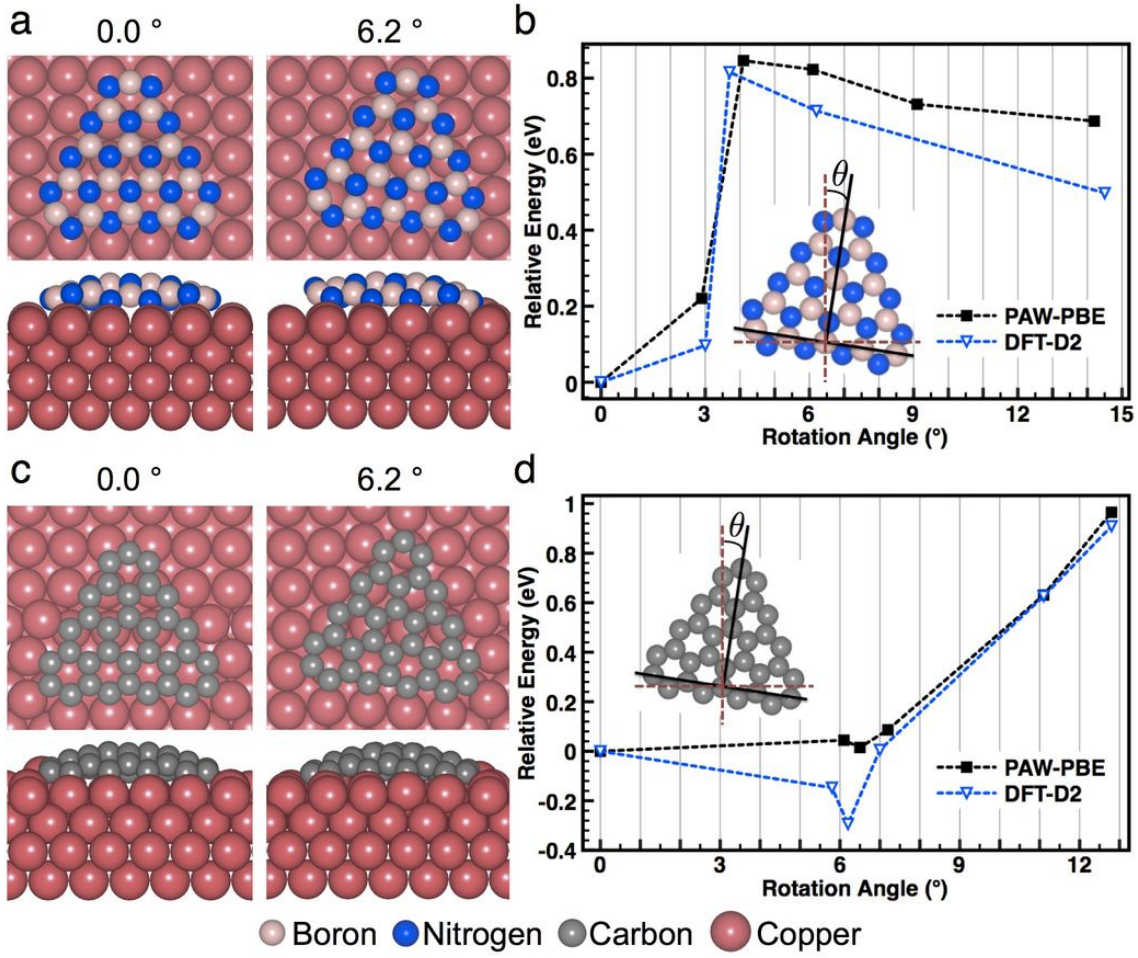

Figure 3.8: DFT calculated stable and metastable BN/Cu(100) and graphene/Cu(100) geometries. (a,c) Top and side views of BN (a) and graphene (c) clusters on Cu(100) with rotation angles 0.0° and 6.2°. (b,d) Total energy vs. rotation angle plots for BN (b) and graphene (d) clusters on Cu(100) calculated by PAW-PBE (vdW not included; black) and DFT-D2 (vdW included; blue). Dashed line segments connecting data points for visual guidance signifies that data points represent discrete stable or metastable configurations; kinetic pathways between these data points remain to be explored.

minimal role in determining the relative stability. One exception is that the $\theta = 9.1^\circ$ geometry obtained by PBE relaxed into $\theta = 6.2^\circ$ for DFT-D2, probably due to vdW interactions between edge atoms and Cu atoms underneath. The calculations support the experimentally observed alignment between the BN and Cu(100) lattices. The alignment of one edge of the cluster with the substrate lattice (see Figure 3.8a) substantially enhances the cluster-substrate interaction, and any rotation away from this high-symmetry configuration will make the cluster less stable.

For comparison, we calculated the total energy vs. rotation angle for a graphene cluster with the same geometry. (While graphene clusters should be equiangular hexagons, our clusters can be considered as six-sided with three edges of the shortest possible zigzag geometry.) The results are summarized in Figures 3.8c,d. Within the PBE, a few orientations in the neighborhood of $\theta = 6.5^\circ$ have nearly equal total energies to that of $\theta = 0^\circ$. By adding vdW interactions, some of these configurations even become more stable than $\theta = 0^\circ$. Moreover, other metastable orientations between $\theta = 0^\circ$ and 6.5° are very likely to exist, although the present DFT study did not find any due to the stringent criteria used for force convergence in ionic relaxation. Therefore, in contrast to the strict alignment of BN on the Cu(100), the graphene cluster can rotate away from the HSO $\theta = 0^\circ$, consistent with the previous reported experiments [264], where the diffraction intensity is high for $\theta \in [0^\circ, \sim 6.5^\circ]$ although nonzero elsewhere.

Although the narrow rotation angle window of low total energy for BN/Cu(100) and a much wider one for graphene/Cu(100) are qualitatively consistent with experiments, the DFT obtained data points *per se* cannot explain why BN/Cu(100) strictly aligns while graphene/Cu(100) exhibits nonzero diffraction intensity at all angles. All data points in Figure 3.8 are total energy local minima in structural relaxation. Without considerably more intensive computation we do not know the exact energy landscape between these local minima. This is a question about how stable these local minima, i.e. metastable configurations, are in the two systems,

which might be answered by exploring the rotation barriers between these local minima at a significantly higher computational cost than in the present work.

Beyond the qualitative consistency with experiments, the DFT calculations gained insights into the alignment mechanism. By inspecting the Cu atoms in the top view models of Figures 3.8a,c, we see that the graphene cluster induce more Cu atom rearrangement than does the BN cluster, making the Cu(100) substrate more reconstructed at the cluster periphery. At a growth temperature close to the melting point of bulk Cu, these Cu atoms are pulled by a rotated cluster from their original positions in the Cu lattice to maximize cluster edge-substrate binding and therefore minimize the cluster-substrate system total energy. (The domed shape of clusters in Figure 3.8 indicates that edge-substrate interactions dominate over interior-substrate interactions.) A graphene zigzag edge, if away from a Cu$< 100 >$ direction, induces appreciable rearrangement of surface Cu atoms, due to strong C-Cu interactions. This action blurs the distinctiveness of a high-symmetry, i.e. aligned, configuration as a total energy minimum. For BN/Cu(100), on the other hand, the surface Cu atom rearrangement is negligible, thus the HSO $\theta = 0^{\circ}$ remains a distinctive total energy minimum. The origin of this difference is that the graphene zigzag edge-Cu interaction is much stronger than the BN zigzag edge-Cu interaction, revealed by the present DFT calculations using the same method as in previous work [39]. To compare the strengths of graphene-Cu and BN-Cu interactions, we define the adsorption energy of a cluster as the total energy of the separate cluster and the Cu substrate minus that of the combined system. The adsorption energy of the graphene cluster is higher than that of the BN cluster by 4.19 eV, calculated by DFT-D2. This difference can be traced to the higher adsorption energy of C compared to B and N monomers. Carbon monomer adsorption energy on Cu(100) is larger than that of B and N by 0.71 eV and 1.65 eV, respectively. Interestingly, this notion that stronger epilayer-substrate interactions can lead to reduced orientational alignment runs counter to conventional wisdom.

The vdW epilayer orientation is determined at the early nucleation stage, when the edge atoms with dangling bonds interact strongly with the substrate, steering the cluster into the lowest energy orientation. When the crystallite grows larger than a critical size, the vdW interaction between the interior atoms and the substrate dominates over the edge-substrate interactions due to the increased area-perimeter ratio, and the orientation is nailed down. Indeed, we have shown that the energetic preference toward alignment with the underlying Cu(100) is overridden when BN growth is templated by a fresh edge of a pre-existing graphene crystallite that is not aligned to the Cu lattice [79]. There, the present finding was asserted to lay down the groundwork for the claim of heteroepitaxy in 2D space.

3.5 Discussion and Conclusion

The picture that edge-substrate interactions steer the orientation of initial nuclei applies in general to vdW epitaxy of 2D crystals. The choice of the BN/ and graphene/Cu(100) systems for this study amplifies this effect due to stronger interactions of the edge atoms with the metal substrate than, say, with a covalent 2D material substrate, signifying that the subject is beyond merely shared symmetry between the epilayer and substrate. The vdW epitaxy are usually incommensurate, therefore registry is lacking, even for epilayer-substrate pairs with shared symmetry. In absence of registry, orientational alignment leads to total energy minima by maximizing epilayer-substrate interaction. Our BN growth on oxygen-contaminated Cu(100) supports the role of direct BN-Cu interaction in achieving alignment. Stronger cluster-substrate interactions in the case of graphene/Cu(100), however, cause substrate surface atom movements, obscuring the aligned orientations as distinctive total energy minima, and therefore reduce orientational order. The fact that BN or graphene is of different symmetry than Cu(100) can lead to more general conclusions not limited to epilayer-substrate pairs with shared symmetry. We nonetheless point out that energetics is not the only factor. Notice that in

early work by molecular beam epitaxy, alignment was observed in all experimented systems [258, 259, 261]. In recent experiments where alignment is lacking [104, 263], kinetics might have led to misalignment for a relatively flat energy-rotation angle landscape that only slightly prefers alignment.

Chapter 4

Electronic and Chemical Properties of Monolayer MoS_2 on Metal Substrates

4.1 Introduction

As a transition-metal dichalcogenide semiconductor, MoS_2 is a commonly used dry lubricant, whose low-dimensional structures are receiving much research attention because of their distinctive electronic [61, 175, 269], optical [61, 65, 66, 270], and catalytic properties [271–275]. Bulk MoS_2 has a layered structure, each layer consisting of a covalently bonded S-Mo-S hexagonal quasi-2D network [276, 277], with weak vdW attraction between the layers. Owing to the relatively weak interlayer interaction, a monolayer of MoS_2 can be mechanically exfoliated from a MoS_2 crystal [10]. Such monolayer systems not only have a direct band gap with highly desirable optical properties [61], but also possess sufficiently high carrier mobility for potential applications in nanoelectronics [156]. In exploring the device potential of monolayer MoS_2, it is vital to understand how such systems interface with metallic contacts, similar to recent developments in other areas of nanomaterials such as

semiconductor wires, carbon nanotubes [278, 279], and graphene [158]. In particular, it was found recently that both the barrier height for electron tunneling and the nature of contact between MoS_2 and an electrode can be drastically altered when using different types of metal contacts [280]. Furthermore, on a different front, monolayer-high MoS_2 islands adsorbed on different metal substrates have been shown to be highly catalytic in HER [272–275], with the reactivity largely attributed to the edge sites of the islands.

In this chapter, we use first-principles calculations within DFT to investigate the electronic and chemical properties of a single-layer MoS_2 adsorbed on Ir(111), Pd(111), or Ru(0001), three representative transition metal substrates having varying work functions but each with minimal lattice mismatch with the MoS_2 overlayer. We find that for each of the metal substrates, the contact nature is of Schottky-barrier type, and the dependence of the barrier height on the work function establishes a partial Fermi-level pinning picture [281]. Using hydrogen adsorption as a testing example, we further demonstrate that the introduction of a metal substrate can substantially alter the chemical reactivity of the adsorbed MoS_2 layer. Our detailed analysis of the electron density redistribution reveals that the enhanced binding of hydrogen, by as much as $\sim$0.4 eV, is attributed in part to a stronger H-S coupling enabled by the transferred charge from the substrate to the MoS_2 overlayer, and in part to a stronger MoS_2-metal interface by the hydrogen adsorption. These findings may prove to be instrumental in future design of MoS_2-based electronics, as well as in exploring novel catalysts for hydrogen production and related chemical processes.

4.2 Methods

Our DFT calculations were carried out using VASP [198] with PAW pseudopotentials [212, 213] and the Ceperley-Alder LDA [282] as parametrized by Perdew and Zunger [188] for the exchange-correlation functional. Unless otherwise specified, the results presented were from LDA calculations. For Pd and Ru as substrates, we have

also compared the LDA results with those from DFT-D2 [197, 239], a semi-empirical approach that includes vdW interactions, to cross check on the accuracy as well as the overall trends of the LDA results [283]. The lattice constants of the metals and the monolayer MoS_2 were obtained via structural optimization. The metal substrates were modeled by slabs of 8 atomic layers, and the MoS_2-metal systems were modeled by placing a single-layer MoS_2 on top of the metal surfaces. A vacuum region more than 15 Å was used to ensure decoupling between neighboring slabs. During structural relaxation, only the bottom layer atoms were fixed in their respective bulk positions, with all the other atoms fully relaxed until the force on any given atom is smaller than 0.01 eV/Å. A $6 \times 6 \times 1$ k-point mesh was used for the 2×2 surface unit cell of metals [214]. When H adsorption was considered, we also examined the effect of spin polarization in our calculations. The spin-orbit coupling effect has also been checked for the heaviest element of Ir, and the detailed results indicate that it has only negligible influence on the energetics.

4.3 Metal-MoS_2 Interfaces

We choose Ir(111), Pd(111), and Ru(0001) as substrates mainly because a $(\sqrt{3} \times \sqrt{3})$ R30° unit cell of MoS_2 can nicely match with a 2×2 unit cell of Ir(111), Pd(111), or Ru(0001), as illustrated in Figure 4.1. The maximum mismatch is ∼1.2% for Ru(0001), with varying work functions of 5.86 eV, 5.74 eV, and 5.42 eV for Ir(111), Pd(111), and Ru(0001), respectively. In our calculations, the surface lattices of the metal substrates were fixed to their optimized values and the in-plane lattice of MoS_2 was adjusted to match the metal substrates accordingly. The most stable contact geometries were obtained by optimizing the structures from different initial configurations. For all the systems, the top layer of the metal substrates and the bottom S layer of MoS_2 essentially stay planar after relaxation, with the MoS_2-metal distances listed in Table 4.1. However, the relative positions between MoS_2 and the substrates along the interface directions are different for different metals. On Ir(111),

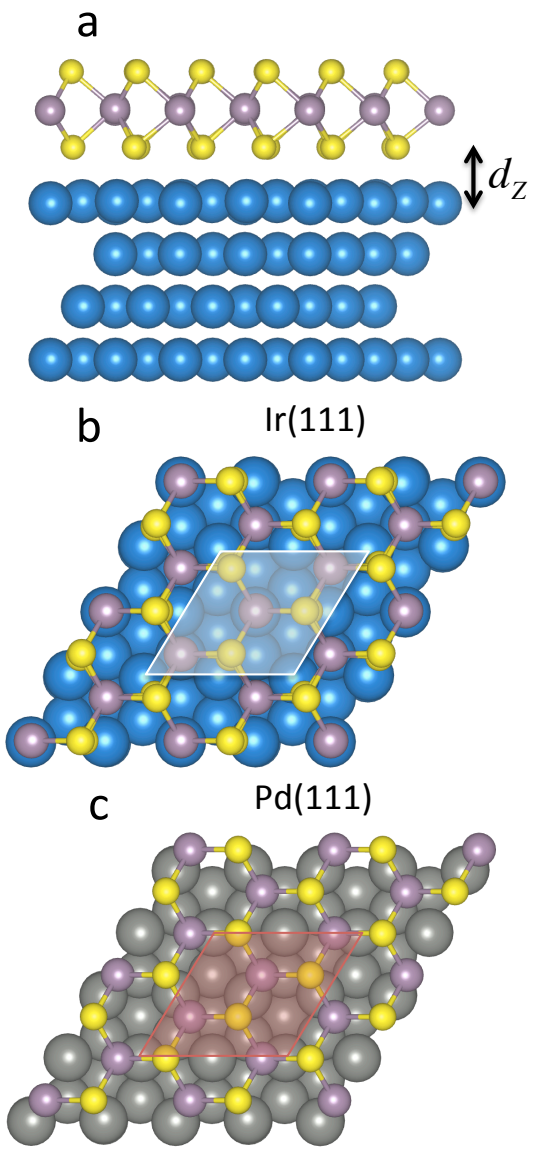

Figure 4.1: (a) Side and (b) top views of monolayer MoS_2 on the Ir(111) substrate. (c) Top view of MoS_2 on the Pd(111) substrate. In (b) and (c), the white- and red-shaded areas show the unit cells in the calculations, respectively.

Table 4.1: Structural and energetic results for all the free-standing MoS_2 and MoS_2-metal systems. E_b is the binding energy per sulfur atom between MoS_2 and a given substrate; d_z^0 and d_z^H are the distances between MoS_2 and a given metal substrate without and with H adsorption, respectively; E_a is the H binding energy on the planar surface of a free-standing MoS_2 or a MoS_2 overlayer on a given substrate; L_{H-S} is the H-S bond length; θ is the angle between the H-S bond and the planar surface of MoS_2.

	E_b(eV)	d_z^0(Å)	d_z^H(Å)	E_a(eV)	L_{H-S}(Å)	θ(°)
Free-standing MoS_2				1.07	1.46	40.2
MoS_2/Ir(111)	0.62	2.23	2.20	1.44	1.43	37.2
MoS_2/Pd(111)	0.74	2.17	2.09	1.39	1.39	89.1
MoS_2/Ru(0001)	0.82	2.25	2.20	1.33	1.46	38.2

the three Mo atoms in the supercell sit above the fcc hollow, hcp hollow, and top sites, respectively (Figure 4.1b); while on Pd(111), the Mo atoms are all above the centers of the triangles formed by the fcc, hcp, and top sites (Figure 4.1c). The registry of MoS_2 relative to the top layer of Ru(0001) is similar to that of Ir(111), and is therefore omitted in Figure 4.1. The MoS_2-metal binding energies per interfacial sulfur atom, calculated as $E_b = (E_{\mathrm{MoS_2}} + E_{\mathrm{metal}} - E_{\mathrm{MoS_2/metal}})/3$, range from 0.62 eV to 0.82 eV as listed in Table 4.1. The inclusion of the vdW interaction increases the binding energy by 0.16 eV for Pd and 0.19 eV for Ru; furthermore, the GGA-vdW results also reduce the interfacial distances between the MoS_2 overlayer and the metal substrates to be close to the LDA results. The even stronger binding energies of the vdW results over LDA, which tends to overestimate the binding [284], should be attributed to the significant attractive contributions of vdW interactions.

4.4 Schottky Barrier Formation

To identify the energy level alignment at the interface between MoS_2 and the metal substrates, we have calculated the band structures of MoS_2 and the combined systems. As seen in Figure 4.2a, the original K point of the 1×1 unit cell where the band edge is located, is folded to the Γ point in the reciprocal space of the $\sqrt{3} \times \sqrt{3}$

superlattice of single-layer MoS_2. The calculated band gap is ∼1.8 eV, consistent with previous results [61, 269]. In the combined systems, although the energy bands of MoS_2 hybridize with those of the metals to a certain extent, the majority of the MoS_2 bands can still be identified, as marked in red in Figures 4.2b-d. The Fermi levels of the combined systems always lie in the band gap region of MoS_2, resulting in the formation of a Schottky barrier at the interface for each case. The calculated n-type Schottky barrier heights (SBHs) corresponding to the energy differences between the conduction band minimum and the Fermi levels are 0.66 eV, 0.79 eV, and 0.72 eV for Ir, Pd, and Ru, respectively (Figure 4.2e). The maximal work function difference is 0.44 eV, while the maximal difference in the SBH is 0.13 eV; we therefore observe a *partial* Fermi level pinning picture [281] when the three metals form contacts with monolayer MoS_2. As for likely pinning mechanisms, the picture of metal-induced gap states is typically operative deep in the semiconductor [159], suggesting that a single layer of MoS_2 is unlikely to cause strong Fermi level pinning, consistent with the present study. Alternatively, we expect that the sufficiently strong chemical bonding at the interface, the other pinning mechanism [160], may have also contributed to the pinning effects.

There is another angle to view the electronic properties and contact nature at the MoS_2-metal interfaces. If the Fermi level pinning effects were absent, we would have expected SBHs of roughly 1.5 eV, 1.4 eV, and 1.1 eV for Ir, Pd, and Ru, respectively, given by the separations between the conduction band minimum and the Fermi level of the monolayer MoS_2 subtracted by the respective work function differences of MoS_2 and Ir, Pd, or Ru. The observed SBHs indicate that there exist pronounced Fermi level shifts of the adsorbed MoS_2, given by ∼1.11 eV, 0.98 eV, and 1.05 eV for Ir, Pd, and Ru, respectively. Similarly, additional Fermi level shifts of up to ∼0.5 eV were also observed in a previous study of graphene-metal contacts [161, 285]. In both cases, such Fermi level shifts can be induced by the resultant effects of charge transfer at the interfaces and chemical bonding effects; the larger and nonlinear Fermi level

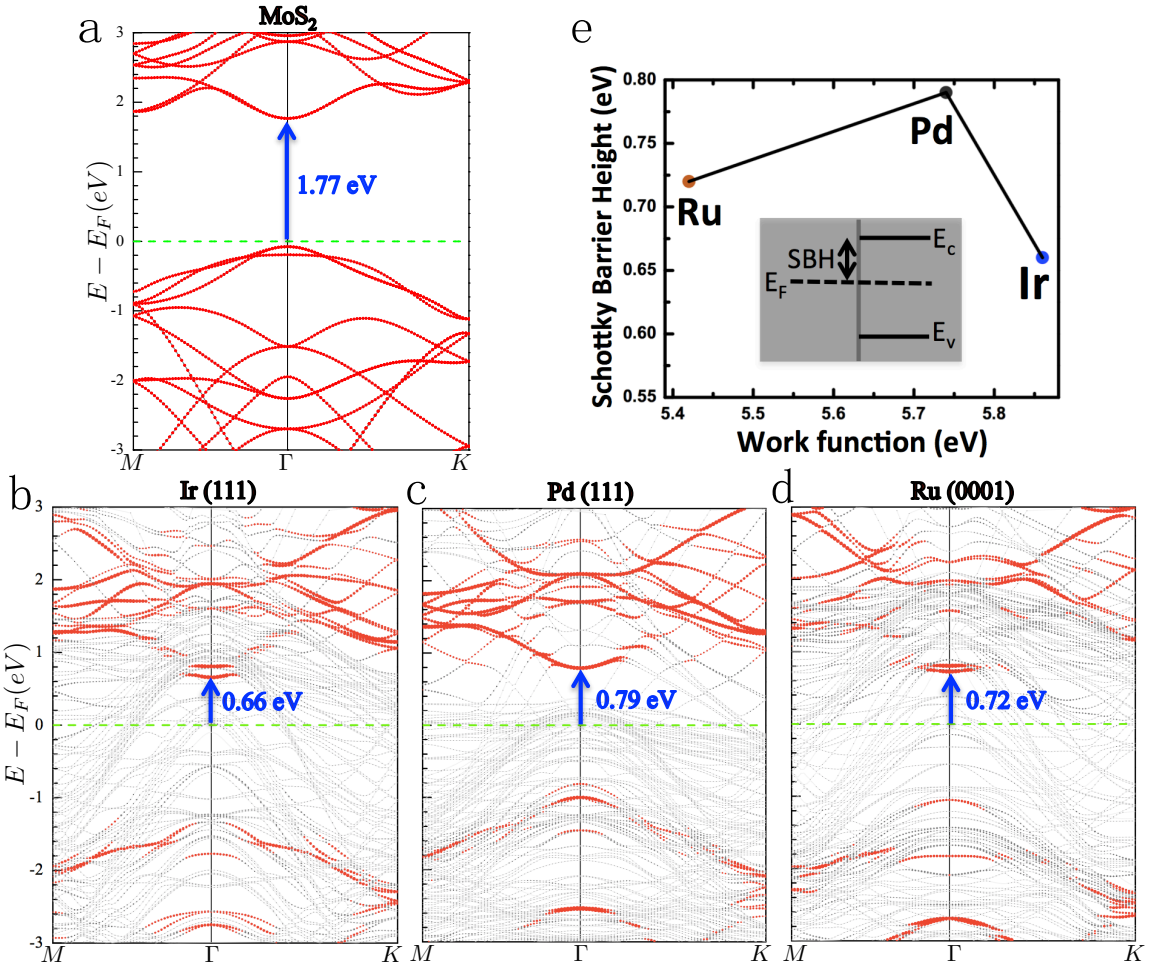

Figure 4.2: Band structures of (a) a $\sqrt{3} \times \sqrt{3}$ superlattice of monolayer MoS_2, (b) the MoS_2-Ir(111), (c) MoS_2-Pd(111), and (d) MoS_2-Ru(0001) interface. The Fermi energy E_F is set to zero in all the four panels and is indicated by the green dashed lines. In (b)-(d), the red lines correspond to the energy bands of the monolayer MoS_2, and the numbers in blue are the SBHs, whose dependence on the work function of the metal substrate is plotted in (e).

shifts are also consistent with the much stronger and varying chemical bondings in the present systems.

To further illustrate the detailed nature of the charge transfer at the MoS_2-metal interfaces, we show in Figure 4.3a the charge difference between the combined MoS_2-Ir(111) system and the sum of the isolated MoS_2 and Ir substrate. The electronic structures of the isolated MoS_2 and Ir substrate were calculated by freezing the atomic positions of the respective components as obtained in the combined system. The red regions represent accumulation and the blue regions represent depletion of electrons in the combined system relative to the two isolated components. To have a quantitative picture, we plot in Figures 4.3b-d the plane-averaged electron density difference $\Delta\rho_z$ along the perpendicular direction to the interface. Several charge transfer oscillations are observed at the interfacial region and some extra charge is found to accumulate around the Mo atoms. Since the position of MoS_2 on Pd(111) is different from that on Ir(111) or Ru(0001), there is a net charge accumulation in the first layer of the Pd substrate closest to MoS_2 (Figure 4.3c), while the first layer of the Ir and Ru substrates is located at places where the net charge transfer is negligible (Figures 4.3b and d). Overall, the oscillatory nature of the charge transfer at the interfaces is complex, but our analysis on the Fermi level shifts given above indicates that the adsorbed MoS_2 is net n-type doped by the three investigated metals.

4.5 Tuning of Chemical Reactivity of MoS_2 Basal Plane

Aside from the transport properties for potential electronic device applications, the significant charge transfer at the MoS_2-metal contacts is also expected to affect the chemical properties of the MoS_2 overlayer. To explore the possibility of tuning the chemical reactivity on the planar surface of MoS_2 through metal substrates, we consider HER as a testing case, which is fundamentally important in a variety of

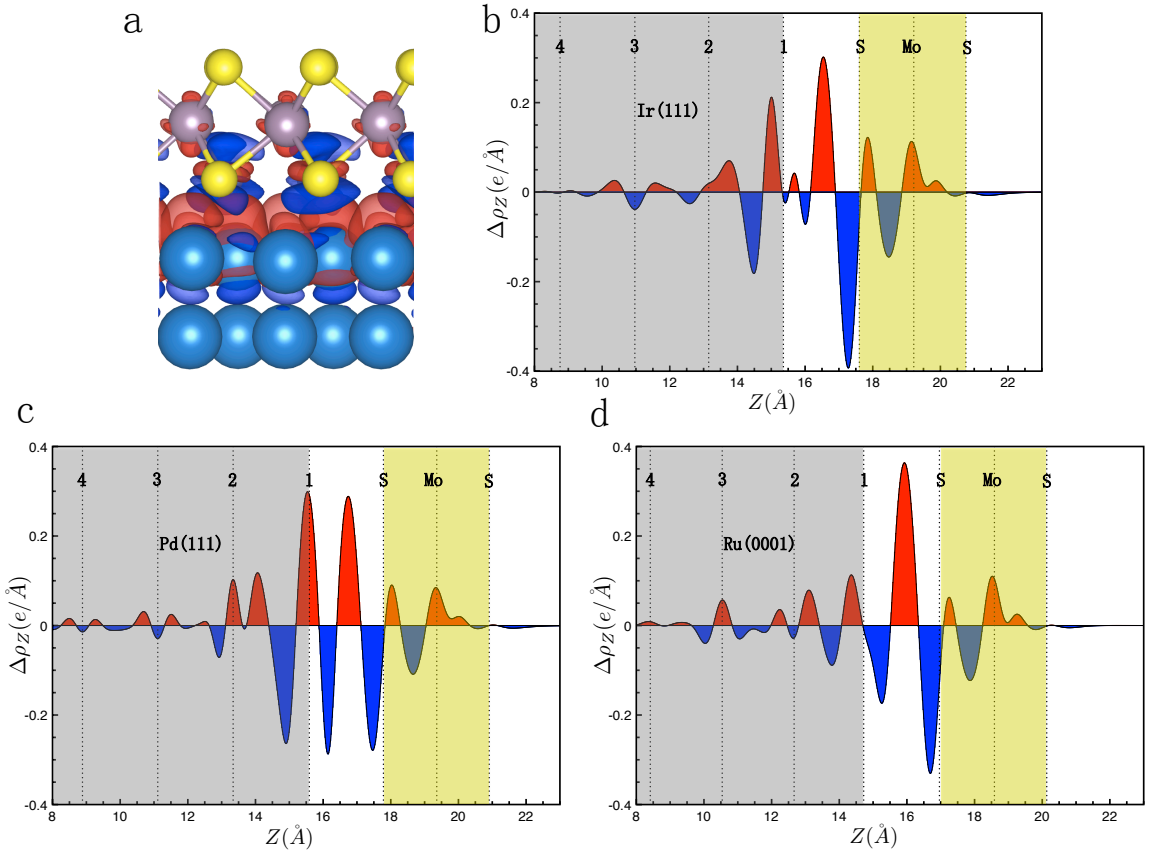

Figure 4.3: (a) Side view of the charge difference between the combined MoS_2-Ir(111) system and the sum of the isolated MoS_2 and Ir substrate. (b)-(d) Plots of the plane-averaged electron density difference along the direction perpendicular to the interface ($\Delta\rho_z$) of MoS_2-Ir(111) (b), MoS_2-Pd(111) (c), and MoS_2-Ru(0001) (d). For each case, the reference location Z = 0 Å is taken to be the position of the bottom layer of the metal substrate in the slab. The red and blue colors indicate electron accumulation and depletion, respectively.

electrochemical processes of technological significance. Currently the most efficient HER catalyst is Pt, which is a precious metal, making it highly desirable to find alternative catalysts based on materials that are abundant and of low-cost. MoS_2 has been demonstrated to be able to function as a HER catalyst, but only the edge sites of the monolayer MoS_2 clusters were identified to be chemically reactive while the planar surface is rather inert [274]. Due to the small lattice mismatches between MoS_2 and the metal substrates considered here, it is expected that large-scale monolayer MoS_2 sheets can be grown on these substrates. Although the planar surface of MoS_2 cannot be as catalytic as the edge sites, considering the large area of the planar surfaces, it is appealing to gain stronger overall reactivity by making the whole planar surfaces sufficiently catalytic. A critical step in HER is that an H^+ ion gains an electron from the electrode, becoming an atomic H, whose binding energy on the catalytic MoS_2 overlayer placed on the electrode is yet another vital energy scale determining the overall HER efficiency. For this important reason and also for simplicity, we study the influence of different metal substrates on the adsorption energy of atomic H on the MoS_2 overlayer, leaving the electron capture process of H^+ for a future study.

To find the most stable adsorption site of H on the surface of a given MoS_2 overlayer, we have examined all possible initial positions based on symmetry considerations. Figure 4.4 depicts the top and side views of the most stable H adsorption geometries on the three metal substrates. The corresponding adsorption energies, calculated as $E_a = E_{\text{hydrogen}} + E_{\text{substrate}} - E_{\text{hydrogen/substrate}}$, are 1.44 eV, 1.39 eV, and 1.33 eV for Ir, Pd, and Ru, respectively (Table 4.1), all of which are substantially enhanced from the value of 1.07 eV on a free-standing MoS_2. We have verified that the DFT-D2 calculations yield only slightly enhanced binding energies over the LDA results (by less than 0.02 eV). In addition to the binding energy differences, we also observe geometrical differences between the considered systems, as measured by θ, the angle between the H-S bond and the planar surface of MoS_2. As shown in Figure 4.4 and Table 4.1, for the systems of MoS_2-Ir(111) and MoS_2-Ru(0001), θ is 37.2° and 38.2°, similar to the angle of 40.2° on the free-standing MoS_2.

In contrast, the H adatom prefers an atop position on MoS_2-Pd(111), with $\theta \approx 90^\circ$, caused by the dramatically different atomic registry between the MoS_2 overlayer and the first layer of the Pd substrate when compared with the other two substrates. Collectively, these results show that both the H binding energy and binding geometry can be tuned with a proper choice of the metal electrode; such tunabilities, in turn, can significantly affect the HER efficiency of the planar MoS_2 overlayer.

To reveal the physical origin of the substrate-enhanced H binding energy, we have calculated the charge transfer between H and the surfaces measured by $\Delta\rho = \rho_{\mathrm{H/MoS_2/metal}} - \rho_{\mathrm{H}} - \rho_{\mathrm{MoS_2/metal}}$. The panels shown in the lower row of Figure 4.4 display the side views of the contour plots of $\Delta\rho$, taken in the plane normal to the interface and across the H-S bond. We see a clear indication that more charge is involved in the covalent H-S bonds on the Ir(111) and Pd(111) substrates, which is also consistent with the shortened bond lengths shown in Table 4.1. In contrast, little change is observed in the H-S bond on Ru(0001) from the free-standing MoS_2 case, consistent with the observation that the enhancement in the adsorption energy is the smallest among the three metals. Aside from the charge redistribution between the H adatom and the MoS_2 overlayer, we can also investigate the effect of H adsorption on the coupling between the MoS_2 and the substrate. Such effects could be quantified by variations in d_z^H, defining the maximum separation of the sulfur atoms in the lower layer of MoS_2 from the topmost layer of the metal substrate. When compared with d_z^0, the separation without the presence of H, d_z^H becomes smaller by 0.03 Å, 0.08 Å, and 0.05 Å for Ir, Pd, and Ru, respectively. These results demonstrate that the enhancements in the adsorption energy arise from two aspects: one is the stronger H-S covalent bonding enabled by the transferred charge from the metal substrates to MoS_2, the other is associated with the stronger MoS_2-metal interfaces caused by the H adatom serving as a "nail" to pin the MoS_2 and substrate together.

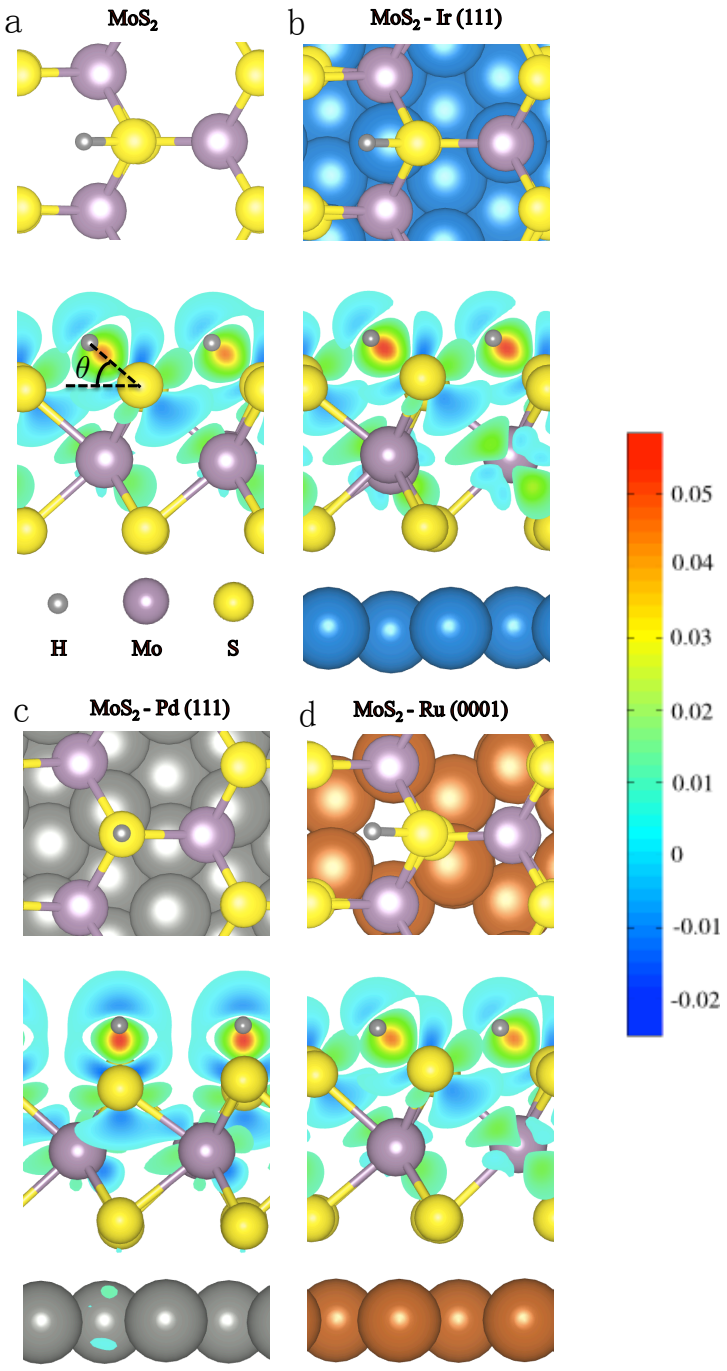

Figure 4.4: Top views of the bonding geometries (upper row) and cross-sectional views of the charge transfer density (lower row) between a H atom and (a) a free-standing MoS_2, (b) the MoS_2/Ir(111), (c) MoS_2/Pd(111), and (d) MoS_2/Ru(0001) system. The red and blue colors represent the maximum charge accumulation and maximum charge depletion, respectively.

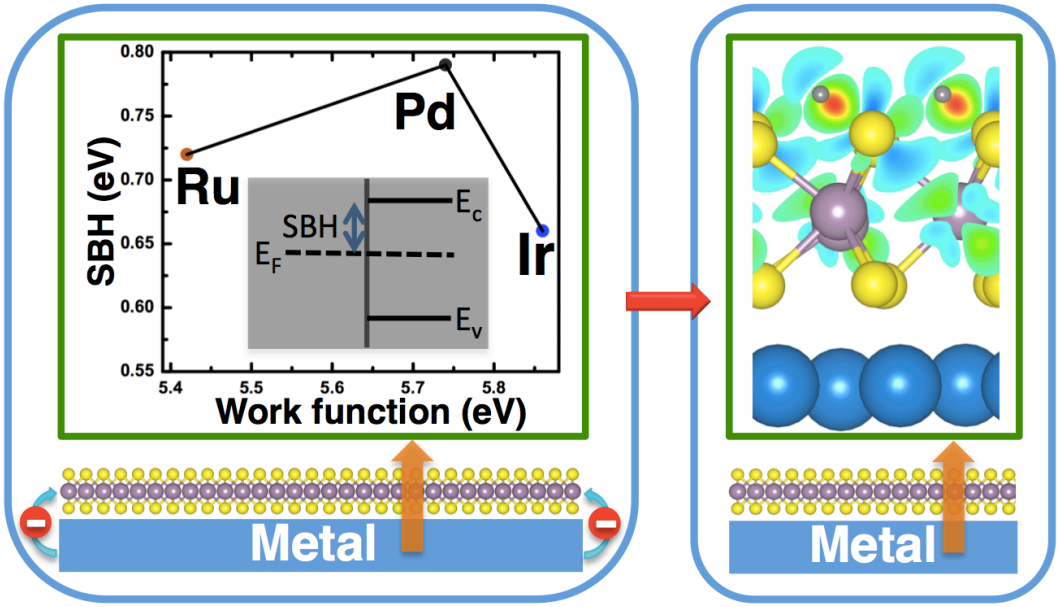

Figure 4.5: Overview: tuning the electronic and chemical properties of monolayer MoS_2 adsorbed on metal substrates through the charge transfer at the interfaces.

4.6 Discussion and Conclusion

Before closing, we note that the significant net charge transfer from the metal substrates to the MoS_2 overlayer will likely have an even stronger effect on the electron capture process of H^+ ion. This intriguing possibility will be examined in a future study of a more complete HER cycle.

In conclusion, as seen in Figure 4.5, we have investigated the electronic and chemical properties of a single-layer MoS_2 adsorbed on Ir(111), Pd(111), or Ru(0001). We found that for each of the metal substrates, the contact nature is of Schottky-barrier type, and the dependence of the SBH on the work function establishes a partial Fermi-level pinning picture for these systems. We have further demonstrated that the introduction of a metal substrate can substantially alter the H binding energy on the MoS_2 overlayer. A detailed analysis of the electron density redistribution revealed that the enhanced binding of hydrogen is the result of a stronger H-S coupling enabled by the transferred charge from the substrate to the MoS_2 overlayer, and a stronger MoS_2-metal interaction caused by the hydrogen adsorption. These findings may prove

to be instrumental in future design of MoS_2-based electronics, as well as in searching for novel catalysts for hydrogen production and related chemical processes.

Chapter 5

Conclusion and Perspective

In this thesis, we investigated the growth and functionality of various layered materials, including graphene, h-BN, and MoS_2, which currently are the most widely used 2D crystals for fundamental research and practical applications. We mainly focused on their monolayer and bilayer structures. Our works not only covered the understanding of growth mechanism and exploration of properties, but also proposed to realize controllable growth processes and desirable properties of layered materials using different design strategies.

Using DFT methods, we understood the formation mechanism of GBs on the Cu(111) substrate, the contrasting mechanisms of bilayer graphene growth on Cu(111) and Ni(111), and the distinct alignment of h-BN and graphene with Cu(100). The interaction between the nucleated graphene or h-BN cluster and the substrate is important, which determines the orientation of the island, and at later stages of growth, results in the formation of GBs when islands coalesce. We therefore proposed to modify the substrate to break the orientational degeneracy, and pin the island at the high symmetry by introducing stronger interactions, that effectively suppress the GB creation. This proposal has recently stimulated our colleagues to grow a new 2D atomic layer without GBs. For multilayer growth, the thermodynamics and kinetics of carbon behaviors determines the growth mode of graphene. We further

performed rate equation analysis, predict the critical size of graphene for adlayer growth underneath, and suggest effective approaches to alter the kinetic processes, thus enhancing multilayer growth.

The electronic and chemical properties of monolayer MoS_2 contacted with metal substrates were investigated. A partial Fermi level pinning picture was discovered, and charge transfer at the interface was found to change the intrinsic properties of MoS_2. By choosing different substrates with varying work functions, SBH can be tuned to different values, and meanwhile the chemical reactivity is enhances in varying degrees, which is reflected in the adsorption of hydrogen.

The present thesis presented several novel pictures, in contrast to the conventional wisdom: in the multilayer growth of graphene, the ES barrier plays an inverse effect, compared to the traditional growth of thin films; in the alignment of h-BN and graphene on Cu(100), stronger epilayer-substrate interactions result in reduced alignment; MoS_2-metal interfaces exhibit a partial Fermi level pinning picture, in contrast to the no pinning effect in graphene-metal contact.

Besides the finished projects presented in this thesis, we are working on the realization of magnetic ordering and topological insulator in a graphene-based atomic layer, with ordered nitrogen substituting carbon atoms (called "graphenne"). This structure has been successfully grown on the metal substrates recently. We propose to choose appropriate metal elements to stably form pairs with the nitrogen dopants, and these pairs are ferromagnetically coupled between each other. Meanwhile, metal adatoms of strong spin-orbit coupling can be introduced to open a band gap of graphene, and further tenability of the Fermi level could result in a graphenne-based topological insulator. Our preliminary results show that Ti or Ir strongly bonds to N, in which Ti exhibits magnetism and Ir introduces strong spin-orbit coupling. In the next stage, the coupling between Ti-N pairs will be examined to search for the ferromagnetic ordering, and the band structures of Ir-graphenne systems are to be calculated at different concentration of adsorption, for the discovery of structurally

robust 2D topological insulator. Meanwhile, adsorption of other elements close to Ti or Ir in the periodic table is also worth exploring.

There are also several projects, or research topics, that I put efforts for months on each of them, but were not finished due to lack of highlights. I definitely learn a lot from trying these topics, and I wish the benefit could produce in the future. Here I list these research topics:

(1) Analyze the band structures of monolayer MoS_2 using group theory, to figure out the contribution of electron orbitals to the bands close to the Fermi level and their corresponding symmetry;

(2) Compare the friction behaviors of water molecules on graphene and MoS_2, using methods combining DFT and molecular dynamics, to explore the failure mechanism of MoS_2 lubricant in humid environments;

(3) Discover the size dependence of magnetism in triangular shaped MoS_2 cluster, using DFT+U method, for potential memory storage application.

After completion of this thesis, I expect to develop capabilities and expand research area in two aspects in my future academic career: one is to be more "abstract", in particular, involving more phenomenological modeling and mathematical derivations; the other is to become more "practical", which seems literally an antonym to the former, but indeed not. I personally find it interesting to model or understand the mesoscopic and macroscopic phenomena in nature or in engineering, whose essence necessarily involves the fundamentals in condensed matter physics.

Bibliography

[1] K. Oura, V. G. Lifshits, A. Saranin, A. V. Zotov, and M. Katayama, *Surface Science: An Introduction*, January 2003 (Springer, 2003).

[2] A. Kumar and C. Lee, in *Adv. Graphene Sci.*, edited by M. Aliofkhazraei (InTech, 2013).

[3] A. K. Geim and I. V. Grigorieva, Nature **499**, 419 (2013).

[4] E. Cockayne, G. M. Rutter, N. P. Guisinger, J. N. Crain, P. N. First, and J. A. Stroscio, Phys. Rev. B **83**, 195425 (2011).

[5] D. Gunlycke and C. T. White, Phys. Rev. Lett. **106**, 136806 (2011).

[6] A. H. Castro Neto, F. Guinea, N. M. R. Peres, K. S. Novoselov, and A. K. Geim, Rev. Mod. Phys. **81**, 109 (2009).

[7] J. E. Moore, Nature **464**, 194 (2010).

[8] S. Z. Butler, S. M. Hollen, L. Cao, Y. Cui, J. A. Gupta, H. R. Gutiérrez, T. F. Heinz, S. S. Hong, J. Huang, A. F. Ismach, et al., ACS Nano **7**, 2898 (2013).

[9] A. K. Geim, Science **324**, 1530 (2009).

[10] K. S. Novoselov, D. Jiang, F. Schedin, T. J. Booth, V. V. Khotkevich, S. V. Morozov, and A. K. Geim, Proc. Natl. Acad. Sci. **102**, 10451 (2005).

[11] F. Banhart, J. Kotakoski, and A. V. Krasheninnikov, ACS Nano **5**, 26 (2011).

[12] P. R. Wallace, Phys. Rev. **71**, 476 (1947).

[13] J. W. McClure, Phys. Rev. **104**, 666 (1956).

[14] D. P. DiVincenzo and E. J. Mele, Phys. Rev. B **29**, 1685 (1984).

[15] G. W. Semenoff, Phys. Rev. Lett. **53**, 2449 (1984).

[16] O. A. Shenderova, V. V. Zhirnov, and D. W. Brenner, Crit. Rev. Solid State Mater. Sci. **27**, 227 (2002).

[17] J. Sakamoto, J. van Heijst, O. Lukin, and A. D. Schlüter, Angew. Chem. Int. Ed. Engl. **48**, 1030 (2009).

[18] K. S. Novoselov, A. K. Geim, S. V. Morozov, D. Jiang, Y. Zhang, S. V. Dubonos, I. V. Grigorieva, and A. A. Firsov, Science **306**, 666 (2004).

[19] J. C. Meyer, A. K. Geim, M. I. Katsnelson, K. S. Novoselov, T. J. Booth, and S. Roth, Nature **446**, 60 (2007).

[20] X. Lu, M. Yu, H. Huang, and R. S. Ruoff, Nanotechnology **10**, 269 (1999).

[21] H. Lüth, *Solid Surfaces, Interfaces and Thin Films*, Graduate Texts in Physics (Springer Berlin Heidelberg, Berlin, Heidelberg, 2010), ISBN 978-3-642-13591-0.

[22] H. Ibach, *Physics of Surfaces and Interfaces* (Springer, 2006), ISBN 3540347097.

[23] Z. Y. Zhang and M. G. Lagally, Science **276**, 377 (1997).

[24] Z. Zhang and M. G. Lagally, *Morphological Organization In Epitaxial Growth And Removal*, vol. 14 of *Series on Directions in Condensed Matter Physics* (World Scientific, 1999), ISBN 978-981-02-3471-3.

[25] Z. Y. Zhang and M. G. Lagally, Phys. Rev. Lett. **72**, 693 (1994).

[26] A. R. Ubbelohde, D. A. Young, and A. W. Moore, Nature **139**, 571 (1962).

[27] P. Sutter, Nat. Mater. **8**, 171 (2009).

[28] K. V. Emtsev, A. Bostwick, K. Horn, J. Jobst, G. L. Kellogg, L. Ley, J. L. McChesney, T. Ohta, S. a. Reshanov, J. Röhrl, et al., Nat. Mater. **8**, 203 (2009).

[29] N. C. Bartelt and K. F. McCarty, MRS Bull. **37**, 1158 (2012).

[30] J. Coraux, A. T N'Diaye, M. Engler, C. Busse, D. Wall, N. Buckanie, F.-J. Meyer zu Heringdorf, R. van Gastel, B. Poelsema, and T. Michely, New J. Phys. **11**, 023006 (2009).

[31] P. W. Sutter, J.-I. Flege, and E. A. Sutter, Nat. Mater. **7**, 406 (2008).

[32] P. Sutter, J. T. Sadowski, and E. Sutter, Phys. Rev. B **80**, 245411 (2009).

[33] S.-Y. Kwon, C. V. Ciobanu, V. Petrova, V. B. Shenoy, J. Bareño, V. Gambin, I. Petrov, and S. Kodambaka, Nano Lett. **9**, 3985 (2009).

[34] S. Roth, J. Osterwalder, and T. Greber, Surf. Sci. **605**, L17 (2011).

[35] T. Oznuluer, E. Pince, E. O. Polat, O. Balci, O. Salihoglu, and C. Kocabas, Appl. Phys. Lett. **98**, 183101 (2011).

[36] K. S. Kim, Y. Zhao, H. Jang, S. Y. Lee, J. M. Kim, K. S. Kim, J.-H. Ahn, P. Kim, J.-Y. Choi, and B. H. Hong, Nature **457**, 706 (2009).

[37] X. Li, W. Cai, J. An, S. Kim, J. Nah, D. Yang, R. Piner, A. Velamakanni, I. Jung, E. Tutuc, et al., Science **324**, 1312 (2009).

[38] X. Li, W. Cai, L. Colombo, and R. S. Ruoff, Nano Lett. **9**, 4268 (2009).

[39] H. Chen, W. Zhu, and Z. Zhang, Phys. Rev. Lett. **104**, 186101 (2010).

[40] X. Li, C. W. Magnuson, A. Venugopal, R. M. Tromp, J. B. Hannon, E. M. Vogel, L. Colombo, and R. S. Ruoff, J. Am. Chem. Soc. **133**, 2816 (2011).

[41] X. Li, Y. Zhu, W. Cai, M. Borysiak, B. Han, D. Chen, R. D. Piner, L. Colombo, and R. S. Ruoff, Nano Lett. **9**, 4359 (2009).

[42] Q. Yu, L. A. Jauregui, W. Wu, R. Colby, J. Tian, Z. Su, H. Cao, Z. Liu, D. Pandey, D. Wei, et al., Nat. Mater. **10**, 443 (2011).

[43] L. Song, L. Ci, H. Lu, P. B. Sorokin, C. Jin, J. Ni, A. G. Kvashnin, D. G. Kvashnin, J. Lou, B. I. Yakobson, et al., Nano Lett. **10**, 3209 (2010).

[44] K. K. Kim, A. Hsu, X. Jia, S. M. Kim, Y. Shi, M. Hofmann, D. Nezich, J. F. Rodriguez-nieva, M. Dresselhaus, T. Palacios, et al., Nano Lett. **12**, 161 (2012).

[45] D. Kim, D. Sun, W. Lu, Z. Cheng, Y. Zhu, D. Le, T. S. Rahman, and L. Bartels, Langmuir **27**, 11650 (2011).

[46] L. Jiao, L. Zhang, X. Wang, G. Diankov, and H. Dai, Nature **458**, 877 (2009).

[47] D. V. Kosynkin, A. L. Higginbotham, A. Sinitskii, J. R. Lomeda, A. Dimiev, B. K. Price, and J. M. Tour, Nature **458**, 872 (2009).

[48] S. Eigler, M. Enzelberger-Heim, S. Grimm, P. Hofmann, W. Kroener, A. Geworski, C. Dotzer, M. Röckert, J. Xiao, C. Papp, et al., Adv. Mater. **25**, 3583 (2013).

[49] A. K. Geim, Rev. Mod. Phys. **83**, 851 (2011).

[50] L. Liu, S. Ryu, M. R. Tomasik, E. Stolyarova, N. Jung, M. S. Hybertsen, M. L. Steigerwald, L. E. Brus, and G. W. Flynn, Nano Lett. **8**, 1965 (2008).

[51] D. C. Elias, R. R. Nair, T. M. G. Mohiuddin, S. V. Morozov, P. Blake, M. P. Halsall, A. C. Ferrari, D. W. Boukhvalov, M. I. Katsnelson, A. K. Geim, et al., Science **323**, 610 (2009).

[52] A. S. Mayorov, R. V. Gorbachev, S. V. Morozov, L. Britnell, R. Jalil, L. A. Ponomarenko, P. Blake, K. S. Novoselov, K. Watanabe, T. Taniguchi, et al., Nano Lett. **11**, 2396 (2011).

[53] A. S. Mayorov, D. C. Elias, I. S. Mukhin, S. V. Morozov, L. A. Ponomarenko, K. S. Novoselov, A. K. Geim, and R. V. Gorbachev, Nano Lett. **12**, 4629 (2012).

[54] W. Bao, J. Velasco, F. Zhang, L. Jing, B. Standley, D. Smirnov, M. Bockrath, A. H. MacDonald, and C. N. Lau, Proc. Natl. Acad. Sci. U. S. A. **109**, 10802 (2012).

[55] T. Taychatanapat, K. Watanabe, T. Taniguchi, and P. Jarillo-Herrero, Nat. Phys. **9**, 225 (2013), `arXiv:1301.1969v1`.

[56] L. A. Ponomarenko, A. K. Geim, A. A. Zhukov, R. Jalil, S. V. Morozov, K. S. Novoselov, I. V. Grigorieva, E. H. Hill, V. V. Cheianov, V. I. Falko, et al., Nat. Phys. **7**, 958 (2011).

[57] I. Meric, C. Dean, A. Young, J. Hone, P. Kim, and K. L. Shepard, in *Electron Devices Meet. (IEDM), 2010 IEEE Int.* (2010), pp. 23.2.1–23.2.4, ISBN 9781424474196.

[58] G.-H. Lee, Y.-J. Yu, C. Lee, C. Dean, K. L. Shepard, P. Kim, and J. Hone, Appl. Phys. Lett. **99**, 243114 (2011).

[59] L. Britnell, R. V. Gorbachev, R. Jalil, B. D. Belle, F. Schedin, M. I. Katsnelson, L. Eaves, S. V. Morozov, A. S. Mayorov, N. M. R. Peres, et al., Nano Lett. **12**, 1707 (2012).

[60] C. R. Dean, A. F. Young, I. Meric, C. Lee, L. Wang, S. Sorgenfrei, K. Watanabe, T. Taniguchi, P. Kim, K. L. Shepard, et al., Nat. Nanotechnol. **5**, 722 (2010).

[61] K. F. Mak, C. Lee, J. Hone, J. Shan, and T. F. Heinz, Phys. Rev. Lett. **105**, 136805 (2010).

[62] W. Jin, P.-C. Yeh, N. Zaki, D. Zhang, J. T. Sadowski, A. Al-Mahboob, A. M. van der Zande, D. A. Chenet, J. I. Dadap, I. P. Herman, et al., Phys. Rev. Lett. **111**, 106801 (2013).

[63] Z. Y. Zhu, Y. C. Cheng, and U. Schwingenschlögl, Phys. Rev. B **84**, 153402 (2011).

[64] D. Xiao, G.-B. Liu, W. Feng, X. Xu, and W. Yao, Phys. Rev. Lett. **108**, 196802 (2012).

[65] H. Zeng, J. Dai, W. Yao, D. Xiao, and X. Cui, Nat. Nanotechnol. **7**, 490 (2012).

[66] K. F. Mak, K. He, J. Shan, and T. F. Heinz, Nat. Nanotechnol. **7**, 494 (2012).

[67] T. Cao, G. Wang, W. Han, H. Ye, C. Zhu, J. Shi, Q. Niu, P. Tan, E. Wang, B. Liu, et al., Nat. Commun. **3**, 887 (2012).

[68] C. Mai, A. Barrette, Y. Yu, Y. Semenov, K. W. Kim, L. Cao, and K. Gundogdu, Nano Lett. **14**, 202 (2014).

[69] M. H. Sluiter and Y. Kawazoe, Phys. Rev. B **68**, 085410 (2003).

[70] R. Zboil, F. Karlický, A. B. Bourlinos, T. A. Steriotis, A. K. Stubos, V. Georgakilas, K. Šafáová, D. Jančík, C. Trapalis, and M. Otyepka, Small **6**, 2885 (2010).

[71] J. T. Robinson, J. S. Burgess, C. E. Junkermeier, S. C. Badescu, T. L. Reinecke, F. K. Perkins, M. K. Zalalutdniov, J. W. Baldwin, J. C. Culbertson, P. E. Sheehan, et al., Nano Lett. **10**, 3001 (2010).

[72] R. R. Nair, W. Ren, R. Jalil, I. Riaz, V. G. Kravets, L. Britnell, P. Blake, F. Schedin, A. S. Mayorov, S. Yuan, et al., Small **6**, 2877 (2010).

[73] W. S. Hummers and R. E. Offeman, J. Am. Chem. Soc. **80**, 1339 (1958).

[74] H. He, J. Klinowski, M. Forster, and A. Lerf, Chem. Phys. Lett. **287**, 53 (1998).

[75] D. R. Dreyer, S. Park, C. W. Bielawski, and R. S. Ruoff, Chem. Soc. Rev. **39**, 228 (2010).

[76] F. Karlický, K. K. R. Datta, M. Otyepka, and R. Zboil, ACS Nano **7**, 6434 (2013).

[77] Z. Jin, J. Yao, C. Kittrell, and J. M. Tour, ACS Nano **5**, 4112 (2011).

[78] L. Ci, L. Song, C. Jin, D. Jariwala, D. Wu, Y. Li, A. Srivastava, Z. F. Wang, K. Storr, L. Balicas, et al., Nat. Mater. **9**, 430 (2010).

[79] L. Liu, J. Park, D. A. Siegel, K. F. McCarty, K. W. Clark, W. Deng, L. Basile, J. C. Idrobo, A.-P. Li, and G. Gu, Science **343**, 163 (2014).

[80] M. Osada and T. Sasaki, Adv. Mater. **24**, 210 (2012).

[81] R. Mas-Ballesté, C. Gómez-Navarro, J. Gómez-Herrero, and F. Zamora, Nanoscale **3**, 20 (2011).

[82] Q. H. Wang, K. Kalantar-Zadeh, A. Kis, J. N. Coleman, and M. S. Strano, Nat. Nanotechnol. **7**, 699 (2012).

[83] M. Xu, T. Liang, M. Shi, and H. Chen, Chem. Rev. **113**, 3766 (2013).

[84] C. Mattevi, H. Kim, and M. Chhowalla, J. Mater. Chem. **21**, 3324 (2011).

[85] S. Bae, H. Kim, Y. Lee, X. Xu, J.-S. Park, Y. Zheng, J. Balakrishnan, T. Lei, H. R. Kim, Y. I. Song, et al., Nat. Nanotechnol. **5**, 574 (2010).

[86] V. P. Verma, S. Das, I. Lahiri, and W. Choi, Appl. Phys. Lett. **96**, 203108 (2010).

[87] W. H. Lee, J. W. Suk, J. Lee, Y. Hao, J. Park, J. W. Yang, H.-W. Ha, S. Murali, H. Chou, D. Akinwande, et al., ACS Nano **6**, 1284 (2012).

[88] J. Kang, D. Shin, S. Bae, and B. H. Hong, Nanoscale **4**, 5527 (2012).

[89] J. Rafiee, X. Mi, H. Gullapalli, A. V. Thomas, F. Yavari, Y. Shi, P. M. Ajayan, and N. A. Koratkar, Nat. Mater. **11**, 217 (2012).

[90] I. Jung, M. Pelton, R. Piner, D. A. Dikin, S. Stankovich, S. Watcharotone, M. Hausner, and R. S. Ruoff, Nano Lett. **7**, 3569 (2007).

[91] P. Blake, E. W. Hill, A. H. Castro Neto, K. S. Novoselov, D. Jiang, R. Yang, T. J. Booth, and A. K. Geim, Appl. Phys. Lett. **91**, 063124 (2007).

[92] S. Neubeck, Y. M. You, Z. H. Ni, P. Blake, Z. X. Shen, A. K. Geim, and K. S. Novoselov, Appl. Phys. Lett. **97**, 053110 (2010).

[93] Y. Y. Wang, R. X. Gao, Z. H. Ni, H. He, S. P. Guo, H. P. Yang, C. X. Cong, and T. Yu, Nanotechnology **23**, 495713 (2012).

[94] G. F. Schneider, V. E. Calado, H. Zandbergen, L. M. K. Vandersypen, and C. Dekker, Nano Lett. **10**, 1912 (2010).

[95] A. M. van der Zande, R. A. Barton, J. S. Alden, C. S. Ruiz-Vargas, W. S. Whitney, P. H. Q. Pham, J. Park, J. M. Parpia, H. G. Craighead, and P. L. McEuen, Nano Lett. **10**, 4869 (2010).

[96] C. Dean, A. F. Young, L. Wang, I. Meric, G.-H. Lee, K. Watanabe, T. Taniguchi, K. Shepard, P. Kim, and J. Hone, Solid State Commun. **152**, 1275 (2012).

[97] X.-D. Chen, Z.-B. Liu, W.-S. Jiang, X.-Q. Yan, F. Xing, P. Wang, Y. Chen, and J.-G. Tian, Sci. Rep. **3**, 3216 (2013).

[98] S. J. Haigh, A. Gholinia, R. Jalil, S. Romani, L. Britnell, D. C. Elias, K. S. Novoselov, L. A. Ponomarenko, A. K. Geim, and R. Gorbachev, Nat. Mater. **11**, 764 (2012).

[99] T. Georgiou, R. Jalil, B. D. Belle, L. Britnell, R. V. Gorbachev, S. V. Morozov, Y.-J. Kim, A. Gholinia, S. J. Haigh, O. Makarovsky, et al., Nat. Nanotechnol. **8**, 100 (2013).

[100] C. H. Lui, L. Liu, K. F. Mak, G. W. Flynn, and T. F. Heinz, Nature **462**, 339 (2009).

[101] Z. Liu, L. Song, S. Zhao, J. Huang, L. Ma, J. Zhang, J. Lou, and P. M. Ajayan, Nano Lett. **11**, 2032 (2011).

[102] G. H. Han, J. A. Rodríguez-Manzo, C.-W. Lee, N. J. Kybert, M. B. Lerner, Z. J. Qi, E. N. Dattoli, A. M. Rappe, M. Drndic, and A. T. C. Johnson, ACS Nano **7**, 10129 (2013).

[103] W. Yang, G. Chen, Z. Shi, C.-C. Liu, L. Zhang, G. Xie, M. Cheng, D. Wang, R. Yang, D. Shi, et al., Nat. Mater. **12**, 792 (2013).

[104] Y. Shi, W. Zhou, A.-Y. Lu, W. Fang, Y.-H. Lee, A. L. Hsu, S. M. Kim, K. K. Kim, H. Y. Yang, L.-J. Li, et al., Nano Lett. **12**, 2784 (2012).

[105] L. A. Ponomarenko, A. K. Geim, A. A. Zhukov, R. Jalil, S. V. Morozov, K. S. Novoselov, I. V. Grigorieva, E. H. Hill, V. V. Cheianov, V. I. Falko, et al., Nat. Phys. **7**, 958 (2011).

[106] R. V. Gorbachev, A. K. Geim, M. I. Katsnelson, K. S. Novoselov, T. Tudorovskiy, I. V. Grigorieva, A. H. MacDonald, S. V. Morozov, K. Watanabe, T. Taniguchi, et al., Nat. Phys. **8**, 896 (2012).

[107] Q. L. He, H. Liu, M. He, Y. H. Lai, H. He, G. Wang, K. T. Law, R. Lortz, J. Wang, and I. K. Sou, eprint arXiv:1309.6040 (2013).

[108] M. Yankowitz, J. Xue, D. Cormode, J. D. Sanchez-Yamagishi, K. Watanabe, T. Taniguchi, P. Jarillo-Herrero, P. Jacquod, and B. J. LeRoy, Nat. Phys. **8**, 382 (2012).

[109] C. R. Dean, L. Wang, P. Maher, C. Forsythe, F. Ghahari, Y. Gao, J. Katoch, M. Ishigami, P. Moon, M. Koshino, et al., Nature **497**, 598 (2013).

[110] B. Hunt, J. D. Sanchez-Yamagishi, A. F. Young, M. Yankowitz, B. J. LeRoy, K. Watanabe, T. Taniguchi, P. Moon, M. Koshino, P. Jarillo-Herrero, et al., Science **340**, 1427 (2013).

[111] J. S. Im, R. S. Sposili, and M. A. Crowder, Appl. Phys. Lett. **70**, 3434 (1997).

[112] K. J. Koski and Y. Cui, ACS Nano **7**, 3739 (2013).

[113] Q. Peng, J. Crean, A. K. Dearden, C. Huang, X. Wen, S. P. A. Bordas, and S. De, Mod. Phys. Lett. B **27**, 1330017 (2013).

[114] W. Zhou, X. Zou, S. Najmaei, Z. Liu, Y. Shi, J. Kong, J. Lou, P. M. Ajayan, B. I. Yakobson, and J.-C. Idrobo, Nano Lett. **13**, 2615 (2013).

[115] R. Singh and P. Kroll, J. Phys. Condens. Matter **21**, 196002 (2009).

[116] O. V. Yazyev and L. Helm, Phys. Rev. B **75**, 125408 (2007).

[117] L. Tapasztó, G. Dobrik, P. Nemes-Incze, G. Vertesy, P. Lambin, and L. P. Biró, Phys. Rev. B **78**, 233407 (2008).

[118] M. Ugeda, D. Fernández-Torre, I. Brihuega, P. Pou, A. Martínez-Galera, R. Pérez, and J. Gómez-Rodríguez, Phys. Rev. Lett. **107**, 116803 (2011).

[119] M. M. Ugeda, I. Brihuega, F. Guinea, and J. M. Gómez-Rodríguez, Phys. Rev. Lett. **104**, 096804 (2010).

[120] M. H. Gass, U. Bangert, A. L. Bleloch, P. Wang, R. R. Nair, and A. K. Geim, Nat. Nanotechnol. **3**, 676 (2008).

[121] J. C. Meyer, C. Kisielowski, R. Erni, M. D. Rossell, M. F. Crommie, and A. Zettl, Nano Lett. **8**, 3582 (2008).

[122] M. Buongiorno Nardelli, B. I. Yakobson, and J. Bernholc, Phys. Rev. B **57**, R4277 (1998).

[123] J. Kotakoski, C. H. Jin, O. Lehtinen, K. Suenaga, and A. V. Krasheninnikov, Phys. Rev. B **82**, 113404 (2010).

[124] W. Chen, Y. Li, G. Yu, Z. Zhou, and Z. Chen, J. Chem. Theory Comput. **5**, 3088 (2009).

[125] J. Ma, D. Alfè, A. Michaelides, and E. Wang, Phys. Rev. B **80**, 033407 (2009).

[126] H.-P. Komsa, S. Kurasch, O. Lehtinen, U. Kaiser, and A. V. Krasheninnikov, Phys. Rev. B **88**, 035301 (2013).

[127] D. West, Y. Y. Sun, H. Wang, J. Bang, and S. B. Zhang, Phys. Rev. B **86**, 121201(R) (2012).

[128] F.-T. Huang, M.-W. Chu, H. H. Kung, W. L. Lee, R. Sankar, S.-C. Liou, K. K. Wu, Y. K. Kuo, and F. C. Chou, Phys. Rev. B **86**, 081104(R) (2012).

[129] P. Y. Huang, C. S. Ruiz-Vargas, A. M. van der Zande, W. S. Whitney, M. P. Levendorf, J. W. Kevek, S. Garg, J. S. Alden, C. J. Hustedt, Y. Zhu, et al., Nature **469**, 389 (2011).

[130] H. I. Rasool, E. B. Song, M. Mecklenburg, B. C. Regan, K. L. Wang, B. H. Weiller, and J. K. Gimzewski, J. Am. Chem. Soc. **133**, 12536 (2011).

[131] J. Lahiri, Y. Lin, P. Bozkurt, I. I. Oleynik, and M. Batzill, Nat. Nanotechnol. **5**, 326 (2010).

[132] Y. Liu, X. Zou, and B. I. Yakobson, ACS Nano **6**, 7053 (2012).

[133] A. L. Gibb, N. Alem, J. H. Chen, K. J. Erickson, J. Ciston, A. Gautam, M. Linck, and A. Zettl, J. Am. Chem. Soc. **135**, 6758 (2013).

[134] O. Cretu, Y.-C. Lin, and K. Suenaga, Nano Lett. **14**, 1064 (2014).

[135] A. M. van der Zande, P. Y. Huang, D. A. Chenet, T. C. Berkelbach, Y. You, G.-H. Lee, T. F. Heinz, D. R. Reichman, D. A. Muller, and J. C. Hone, Nat. Mater. **12**, 554 (2013).

[136] S. Najmaei, Z. Liu, W. Zhou, X. Zou, G. Shi, S. Lei, B. I. Yakobson, J.-C. Idrobo, P. M. Ajayan, and J. Lou, Nat. Mater. **12**, 754 (2013).

[137] A. N. Enyashin, M. Bar-Sadan, L. Houben, and G. Seifert, J. Phys. Chem. C **117**, 10842 (2013).

[138] Y. Liu, Y. Y. Li, S. Rajput, D. Gilks, L. Lari, P. L. Galindo, M. Weinert, V. K. Lazarov, and L. Li, Nat. Phys. **10**, 294 (2014).

[139] Y. Liu, M. Weinert, and L. Li, Phys. Rev. Lett. **108**, 115501 (2012).

[140] R. Grantab, V. B. Shenoy, and R. S. Ruoff, Science **330**, 946 (2010).

[141] O. V. Yazyev and S. G. Louie, Nat. Mater. **9**, 806 (2010).

[142] A. K. Geim and K. S. Novoselov, Nat. Mater. **6**, 183 (2007).

[143] K. S. Novoselov, A. K. Geim, S. V. Morozov, D. Jiang, M. I. Katsnelson, I. V. Grigorieva, S. V. Dubonos, and A. A. Firsov, Nature **438**, 197 (2005).

[144] Y. Zhang, Y.-W. Tan, H. L. Stormer, and P. Kim, Nature **438**, 201 (2005).

[145] V. P. Gusynin and S. G. Sharapov, Phys. Rev. Lett. **95**, 146801 (2005).

[146] L. Fu and C. L. Kane, Phys. Rev. B **76**, 045302 (2007).

[147] X.-L. Qi and S.-C. Zhang, Rev. Mod. Phys. **83**, 1057 (2011).

[148] M. Z. Hasan and C. L. Kane, Rev. Mod. Phys. **82**, 3045 (2010).

[149] H. Chen, W. Zhu, D. Xiao, and Z. Zhang, Phys. Rev. Lett. **107**, 056804 (2011).

[150] C.-Z. Chang, J. Zhang, X. Feng, J. Shen, Z. Zhang, M. Guo, K. Li, Y. Ou, P. Wei, L.-L. Wang, et al., Science **340**, 167 (2013).

[151] C. L. Kane and E. J. Mele, Phys. Rev. Lett. **95**, 146802 (2005).

[152] J. Hu, J. Alicea, R. Wu, and M. Franz, Phys. Rev. Lett. **109**, 266801 (2012).

[153] H. Zhang, C. Lazo, S. Blügel, S. Heinze, and Y. Mokrousov, Phys. Rev. Lett. **108**, 056802 (2012).

[154] L. Kou, B. Yan, F. Hu, S.-C. Wu, T. O. Wehling, C. Felser, C. Chen, and T. Frauenheim, Nano Lett. **13**, 6251 (2013).

[155] F. Schwierz, Nat. Nanotechnol. **5**, 487 (2010).

[156] B. Radisavljevic, A. Radenovic, J. Brivio, V. Giacometti, and A. Kis, Nat. Nanotechnol. **6**, 147 (2011).

[157] J. O. McCaldin and T. C. McGill, Annu. Rev. Mater. Sci. p. 65 (1980).

[158] F. Léonard and A. A. Talin, Nat. Nanotechnol. **6**, 773 (2011).

[159] J. Tersoff, Phys. Rev. Lett. **52**, 465 (1984).

[160] R. T. Tung, Phys. Rev. Lett. **84**, 6078 (2000).

[161] G. Giovannetti, P. A. Khomyakov, G. Brocks, V. M. Karpan, J. van den Brink, and P. J. Kelly, Phys. Rev. Lett. **101**, 026803 (2008).

[162] M. A. Bissett, S. Konabe, S. Okada, M. Tsuji, and H. Ago, ACS Nano **7**, 10335 (2013).

[163] Q. Wu, Y. Wu, Y. Hao, J. Geng, M. Charlton, S. Chen, Y. Ren, H. Ji, H. Li, D. W. Boukhvalov, et al., Chem. Commun. **49**, 677 (2013).

[164] R. Sharma, J. H. Baik, C. J. Perera, and M. S. Strano, Nano Lett. **10**, 398 (2010).

[165] M. Chhowalla, H. S. Shin, G. Eda, L.-J. Li, K. P. Loh, and H. Zhang, Nat. Chem. **5**, 263 (2013).

[166] L. Qu, Y. Liu, J.-B. Baek, and L. Dai, ACS Nano **4**, 1321 (2010).

[167] D. Voiry, H. Yamaguchi, J. Li, R. Silva, D. C. B. Alves, T. Fujita, M. Chen, T. Asefa, V. B. Shenoy, G. Eda, et al., Nat. Mater. **12**, 850 (2013).

[168] J. Kibsgaard, Z. Chen, B. N. Reinecke, and T. F. Jaramillo, Nat. Mater. **11**, 963 (2012).

[169] J. K. Nø rskov, T. Bligaard, J. Rossmeisl, and C. H. Christensen, Nat. Chem. **1**, 37 (2009).

[170] Z. Qiao, W. Ren, H. Chen, L. Bellaiche, Z. Zhang, A. H. MacDonald, and Q. Niu, Phys. Rev. Lett. **112**, 116404 (2014).

[171] M. Sherafati and S. Satpathy, Phys. Rev. B **83**, 165425 (2011).

[172] D. Pesin and A. H. MacDonald, Nat. Mater. **11**, 409 (2012).

[173] E.-J. Kan, Z. Li, J. Yang, and J. G. Hou, J. Am. Chem. Soc. **130**, 4224 (2008).

[174] W. L. Wang, O. V. Yazyev, S. Meng, and E. Kaxiras, Phys. Rev. Lett. **102**, 157201 (2009).

[175] Y. Li, Z. Zhou, S. Zhang, and Z. Chen, J. Am. Chem. Soc. **130**, 16739 (2008).

[176] J. Červenka, M. I. Katsnelson, and C. F. J. Flipse, Nat. Phys. **5**, 840 (2009).

[177] Y. Wang, Y. Huang, Y. Song, X. Zhang, Y. Ma, J. Liang, and Y. Chen, Nano Lett. **9**, 220 (2009).

[178] J. Zhou, T. Hu, J. Dong, and Y. Kawazoe, Phys. Rev. B **86**, 035434 (2012).

[179] S. Tongay, S. S. Varnoosfaderani, B. R. Appleton, J. Wu, and A. F. Hebard, Appl. Phys. Lett. **101**, 123105 (2012).

[180] M. Wu, E.-Z. Liu, and J. Z. Jiang, Appl. Phys. Lett. **93**, 082504 (2008).

[181] X. Liu, C. Z. Wang, M. Hupalo, W. C. Lu, M. C. Tringides, Y. X. Yao, and K. M. Ho, Phys. Chem. Chem. Phys. **14**, 9157 (2012).

[182] J. He, K. Wu, R. Sa, Q. Li, and Y. Wei, Appl. Phys. Lett. **96**, 082504 (2010).

[183] Y. C. Cheng, Z. Y. Zhu, W. B. Mi, Z. B. Guo, and U. Schwingenschlögl, Phys. Rev. B **87**, 100401(R) (2013).

[184] W. Zhu, X. Qiu, V. Iancu, X.-Q. Chen, H. Pan, W. Wang, N. Dimitrijevic, T. Rajh, H. Meyer, M. Paranthaman, et al., Phys. Rev. Lett. **103**, 226401 (2009).

[185] S. Qi, H. Chen, X. Xu, and Z. Zhang, Carbon **61**, 609 (2013).

[186] P. Hohenberg and W. Kohn, Phys. Rev. **136**, B864 (1964).

[187] W. Kohn and L. J. Sham, Phys. Rev. **140**, A1133 (1965).

[188] J. P. Perdew and A. Zunger, Phys. Rev. B **23**, 5048 (1981).

[189] J. P. Perdew, J. A. Chevary, S. H. Vosko, K. A. Jackson, M. R. Pederson, D. J. Singh, and C. Fiolhais, Phys. Rev. B **46**, 6671 (1992).

[190] J. P. Perdew, K. Burke, and M. Ernzerhof, Phys. Rev. Lett. **77**, 3865 (1996).

[191] A. D. Becke, Phys. Rev. A **38**, 3098 (1988).

[192] C. Lee, W. Yang, and R. G. Parr, Phys. Rev. B **37**, 785 (1988).

[193] H. Margenau, Rev. Mod. Phys. **11**, 1 (1939).

[194] M. Dion, H. Rydberg, E. Schröder, D. C. Langreth, and B. I. Lundqvist, Phys. Rev. Lett. **92**, 246401 (2004).

[195] J. Klimeš, D. R. Bowler, and A. Michaelides, Phys. Rev. B **83**, 195131 (2011).

[196] X. Wu, M. C. Vargas, S. Nayak, V. Lotrich, and G. Scoles, J. Chem. Phys. **115**, 8748 (2001).

[197] S. Grimme, J. Comput. Chem. **27**, 1787 (2006).

[198] G. Kresse and J. Furthmüller, Phys. Rev. B **54**, 11169 (1996).

[199] H. Ago, Y. Ito, N. Mizuta, K. Yoshida, B. Hu, C. M. Orofeo, M. Tsuji, K.-i. Ikeda, and S. Mizuno, ACS Nano **4**, 7407 (2010).

[200] L. Gao, J. R. Guest, and N. P. Guisinger, Nano Lett. **10**, 3512 (2010).

[201] Z. Sun, Z. Yan, J. Yao, E. Beitler, Y. Zhu, and J. M. Tour, Nature **468**, 549 (2010).

[202] Z. Li, P. Wu, C. Wang, X. Fan, W. Zhang, X. Zhai, C. Zeng, Z. Li, J. Yang, and J. Hou, ACS Nano **5**, 3385 (2011).

[203] P. M. Ajayan and B. I. Yakobson, Nat. Mater. **10**, 415 (2011).

[204] O. V. Yazyev and S. G. Louie, Phys. Rev. B **81**, 195420 (2010).

[205] K. Kim, Z. Lee, W. Regan, C. Kisielowski, M. F. Crommie, and A. Zettl, ACS Nano **5**, 2142 (2011).

[206] J. An, E. Voelkl, J. W. Suk, X. Li, C. W. Magnuson, L. Fu, P. Tiemeijer, M. Bischoff, B. Freitag, E. Popova, et al., ACS Nano **5**, 2433 (2011).

[207] X. Li, C. W. Magnuson, A. Venugopal, J. An, J. W. Suk, B. Han, M. Borysiak, W. Cai, A. Velamakanni, Y. Zhu, et al., Nano Lett. **10**, 4328 (2010).

[208] G. Rosenfeld, R. Servaty, C. Teichert, B. Poelsema, and G. Comsa, Phys. Rev. Lett. **71**, 895 (1993).

[209] J. C. Fetzer, *The Chemistry and Analysis of the Large Polycyclic Aromatic Hydrocarbons*, vol. 27 (2000).

[210] J. Schneider, A. Rosenhahn, and K. Wandelt, Appl. Surf. Sci. **142**, 68 (1999).

[211] G. Bihlmayer, P. Kurz, and S. Blügel, Phys. Rev. B **62**, 4726 (2000).

[212] P. E. Blöchl, Phys. Rev. B **50**, 17953 (1994).

[213] G. Kresse and D. Joubert, Phys. Rev. B **59**, 1758 (1999).

[214] M. Methfessel and A. T. Paxton, Phys. Rev. B **40**, 3616 (1989).

[215] W. Zhang, P. Wu, Z. Li, and J. Yang, J. Phys. Chem. C **115**, 17782 (2011).

[216] B. I. Yakobson and F. Ding, ACS Nano **5**, 1569 (2011).

[217] P. Lacovig, M. Pozzo, D. Alfè, P. Vilmercati, A. Baraldi, and S. Lizzit, Phys. Rev. Lett. **103**, 166101 (2009).

[218] I. S. Youn, D. Y. Kim, N. J. Singh, S. W. Park, J. Youn, and K. S. Kim, J. Chem. Theory Comput. **8**, 99 (2012).

[219] J. G. Chen, C. A. Menning, and M. B. Zellner, Surf. Sci. Rep. **63**, 201 (2008).

[220] C. Barckholtz, T. A. Barckholtz, and C. M. Hadad, J. Am. Chem. Soc. **121**, 491 (1999).

[221] D. Martoccia, P. R. Willmott, T. Brugger, M. Björck, S. Günther, C. M. Schlepütz, A. Cervellino, S. A. Pauli, B. D. Patterson, S. Marchini, et al., Phys. Rev. Lett. **101**, 126102 (2008).

[222] Y. Zhang, T.-T. Tang, C. Girit, Z. Hao, M. C. Martin, A. Zettl, M. F. Crommie, Y. R. Shen, and F. Wang, Nature **459**, 820 (2009).

[223] A. N. Pal and A. Ghosh, Appl. Phys. Lett. **95**, 082105 (2009).

[224] C. H. Lui, Z. Li, K. F. Mak, E. Cappelluti, and T. F. Heinz, Nat. Phys. **7**, 944 (2011).

[225] S. Chen, W. Cai, R. D. Piner, J. W. Suk, Y. Wu, Y. Ren, J. Kang, and R. S. Ruoff, Nano Lett. **11**, 3519 (2011).

[226] N. Liu, L. Fu, B. Dai, K. Yan, X. Liu, R. Zhao, Y. Zhang, and Z. Liu, Nano Lett. **11**, 297 (2011).

[227] X. Liu, L. Fu, N. Liu, T. Gao, Y. Zhang, L. Liao, and Z. Liu, J. Phys. Chem. C **115**, 11976 (2011).

[228] Y. Wu, H. Chou, H. Ji, Q. Wu, S. Chen, W. Jiang, Y. Hao, J. Kang, Y. Ren, R. D. Piner, et al., ACS Nano **6**, 7731 (2012).

[229] S. Lee, K. Lee, and Z. Zhong, Nano Lett. **10**, 4702 (2010).

[230] K. Yan, H. Peng, Y. Zhou, H. Li, and Z. Liu, Nano Lett. **11**, 1106 (2011).

[231] M. Kalbac, O. Frank, and L. Kavan, Carbon **50**, 3682 (2012).

[232] S. Nie, W. Wu, S. Xing, Q. Yu, J. Bao, S.-s. Pei, and K. F. McCarty, New J. Phys. **14**, 093028 (2012).

[233] Q. Li, H. Chou, J.-H. Zhong, J.-Y. Liu, A. Dolocan, J. Zhang, Y. Zhou, R. S. Ruoff, S. Chen, and W. Cai, Nano Lett. **13**, 486 (2013).

[234] W. Song, C. Jeon, S. Youn Kim, Y. Kim, S. Hwan Kim, S.-I. Lee, D. S. Jung, M. W. Jung, K.-S. An, and C.-Y. Park, Carbon **68**, 87 (2014).

[235] P. R. Kidambi, B. C. Bayer, R. Blume, Z.-J. Wang, C. Baehtz, R. S. Weatherup, M.-G. Willinger, R. Schloegl, and S. Hofmann, Nano Lett. **13**, 4769 (2013).

[236] X. Zhang, L. Wang, J. Xin, B. I. Yakobson, and F. Ding, J. Am. Chem. Soc. **136**, 3040 (2014).

[237] G. Ehrlich and F. G. Hudda, J. Chem. Phys. **44**, 1039 (1966).

[238] R. L. Schwoebel, J. Appl. Phys. **40**, 614 (1969).

[239] T. Bučko, J. Hafner, S. Lebègue, and J. G. Ángyán, J. Phys. Chem. A **114**, 11814 (2010).

[240] F. Abild-Pedersen, J. K. Nø rskov, J. R. Rostrup-Nielsen, J. Sehested, and S. Helveg, Phys. Rev. B **73**, 115419 (2006).

[241] Y.-A. Zhu, Y.-C. Dai, D. Chen, and W.-K. Yuan, Surf. Sci. **601**, 1319 (2007).

[242] G. Henkelman, B. P. Uberuaga, and H. Jónsson, J. Chem. Phys. **113**, 9901 (2000).

[243] E. Voloshina and Y. Dedkov, Phys. Chem. Chem. Phys. **14**, 13502 (2012).

[244] M. Vanin, J. J. Mortensen, A. K. Kelkkanen, J. M. Garcia-Lastra, K. S. Thygesen, and K. W. Jacobsen, Phys. Rev. B **81**, 081408(R) (2010).

[245] M. Dion, H. Rydberg, E. Schröder, D. C. Langreth, and B. I. Lundqvist, Phys. Rev. Lett. **95**, 109902 (2005).

[246] Y. Gamo, A. Nagashima, M. Wakabayashi, M. Terai, and C. Oshima, Surf. Sci. **374**, 61 (1997).

[247] A. Varykhalov, M. R. Scholz, T. K. Kim, and O. Rader, Phys. Rev. B **82**, 121101(R) (2010).

[248] W. Chen, H. Chen, H. Lan, P. Cui, T. P. Schulze, W. Zhu, and Z. Zhang, Phys. Rev. Lett. **109**, 265507 (2012).

[249] X. Zhang, Z. Xu, L. Hui, J. Xin, and F. Ding, J. Phys. Chem. Lett. **3**, 2822 (2012).

[250] R. G. Van Wesep, H. Chen, W. Zhu, and Z. Zhang, J. Chem. Phys. **134**, 171105 (2011).

[251] J. Tersoff, A. W. D. van der Gon, and R. M. Tromp, Phys. Rev. Lett. **72**, 266 (1994).

[252] J. A. Venables, G. D. T. Spiller, and M. Hanbücken, Reports Prog. Phys. **47**, 399 (1984).

[253] S. N. Filimonov and Y. Y. Hervieu, Phys. Rev. B **85**, 045423 (2012).

[254] E. G. Seebauer and C. E. Allen, Prog. Surf. Sci. **49**, 265 (1995).

[255] A. F. Voter, in *Radiat. Eff. Solids*, edited by K. E. Sickafus and E. A. Kotomin (Springer Netherlands, 2007), vol. 235, pp. 1–23.

[256] L. Britnell, R. V. Gorbachev, A. K. Geim, L. A. Ponomarenko, A. Mishchenko, M. T. Greenaway, T. M. Fromhold, K. S. Novoselov, and L. Eaves, Nat. Commun. **4**, 1794 (2013).

[257] R. M. Feenstra, D. Jena, and G. Gu, J. Appl. Phys. **111**, 043711 (2012).

[258] A. Koma, K. Saiki, and Y. Sato, Appl. Surf. Sci. **41/42**, 451 (1989).

[259] A. Koma, Surf. Sci. **267**, 29 (1992).

[260] S. R. Forrest, Chem. Rev. **97**, 1793 (1997).

[261] A. Koma, J. Cryst. Growth **201/202**, 236 (1999).

[262] S. Tang, H. Wang, Y. Zhang, A. Li, H. Xie, X. Liu, L. Liu, T. Li, F. Huang, X. Xie, et al., Sci. Rep. **3**, 2666 (2013).

[263] J. Hwang, M. Kim, D. Campbell, H. A. Alsalman, J. Y. Kwak, S. Shivaraman, A. R. Woll, A. K. Singh, R. G. Hennig, S. Gorantla, et al., ACS Nano **7**, 385 (2013).

[264] J. M. Wofford, S. Nie, K. F. McCarty, N. C. Bartelt, and O. D. Dubon, Nano Lett. **10**, 4890 (2010).

[265] I. Vlassiouk, M. Regmi, P. Fulvio, S. Dai, P. Datskos, G. Eres, and S. Smirnov, ACS Nano **5**, 6069 (2011).

[266] Y. Liu, S. Bhowmick, and B. I. Yakobson, Nano Lett. **11**, 3113 (2011).

[267] R. Geick, C. H. Perry, and G. Rupprecht, Phys. Rev. **146**, 543 (1966).

[268] M. Harrison, D. P. Woodruff, J. Robinson, D. Sander, W. Pan, and J. Kirschner, Phys. Rev. B **74**, 165402 (2006).

[269] S. W. Han, H. Kwon, S. K. Kim, S. Ryu, W. S. Yun, D. H. Kim, J. H. Hwang, J.-S. Kang, J. Baik, H. J. Shin, et al., Phys. Rev. B **84**, 045409 (2011).

[270] A. Splendiani, L. Sun, Y. Zhang, T. Li, J. Kim, C.-Y. Chim, G. Galli, and F. Wang, Nano Lett. **10**, 1271 (2010).

[271] P. G. Moses, B. Hinnemann, H. Topsø e, and J. K. Nø rskov, J. Catal. **248**, 188 (2007).

[272] B. Hinnemann, P. G. Moses, J. Bonde, K. P. Jø rgensen, J. H. Nielsen, S. Horch, I. Chorkendorff, and J. K. Nø rskov, J. Am. Chem. Soc. **127**, 5308 (2005).

[273] J. Bonde, P. G. Moses, T. F. Jaramillo, J. K. Nø rskov, and I. Chorkendorff, Faraday Discuss. **140**, 219 (2008).

[274] T. F. Jaramillo, K. P. Jø rgensen, J. Bonde, J. H. Nielsen, S. Horch, and I. Chorkendorff, Science **317**, 100 (2007).

[275] Y. Li, H. Wang, L. Xie, Y. Liang, H. Guosong, and H. Dai, J. Am. Chem. Soc. **133**, 7296 (2011).

[276] S. Helveg, J. V. Lauritsen, E. Læ gsgaard, I. Stensgaard, J. K. Nø rskov, B. S. Clausen, H. Topsø e, and F. Besenbacher, Phys. Rev. Lett. **84**, 951 (2000).

[277] J. V. Lauritsen, J. Kibsgaard, S. Helveg, H. Topsø e, B. S. Clausen, E. Læ gsgaard, and F. Besenbacher, Nat. Nanotechnol. **2**, 53 (2007).

[278] W. Zhu and E. Kaxiras, Nano Lett. **6**, 1415 (2006).

[279] W. Zhu and E. Kaxiras, Appl. Phys. Lett. **89**, 243107 (2006).

[280] I. Popov, G. Seifert, and D. Tománek, Phys. Rev. Lett. **108**, 156802 (2012).

[281] S. Kurtin, T. C. McGill, and C. A. Mead, Phys. Rev. Lett. **22**, 1433 (1969).

[282] D. M. Ceperley and B. J. Alder, Phys. Rev. Lett. **45**, 566 (1980).

[283] L. Schimka, J. Harl, A. Stroppa, A. Grüneis, M. Marsman, F. Mittendorfer, and G. Kresse, Nat. Mater. **9**, 741 (2010).

[284] Y. Gao and X. C. Zeng, J. Phys. Condens. Matter **19**, 386220 (2007).

[285] P. A. Khomyakov, G. Giovannetti, P. C. Rusu, G. Brocks, J. van den Brink, and P. J. Kelly, Phys. Rev. B **79**, 195425 (2009).

List of Publications

1. W. Chen, H. Chen, H. P. Lan, P. Cui, T. P. Schulze, W. G. Zhu, and Z. Y. Zhang, "Suppression of Grain Boundaries in Graphene Growth on Superstructured Mn-Cu(111) Surface", *Phys. Rev. Lett.* **109**, 265507 (2012).

2. W. Chen, E. J. G. Santos, W. G. Zhu, E. Kaxiras, and Z. Y. Zhang, "Tuning the Electronic and Chemical Properties of Monolayer MoS_2 Adsorbed on Transition Metal Substrates", *Nano Lett.* **13**, 509 (2013).

3. L. Liu*, D. A. Siegel*, W. Chen* (equal contribution), P. Z. Liu, J. J. Guo, G. Duscher, C. Zhao, H. Wang, W. L. Wang, X. D. Bai, K. F. McCarty, Z. Y. Zhang, and G. Gu, "Epilayer-Substrate Interactions and Orientational Order in van der Waals Epitaxy: A Case Study", submitted to *Proc. Natl. Acad. Sci. U.S.A.* (2014).

4. W. Chen, W. G. Zhu, Y. F. Gao, E. Kaxiras, and Z. Y. Zhang, "Contrasting Mechanisms of Graphene Bilayer Growth on Cu and Ni", to be submitted to *Phys. Rev. Lett.* (2014).

5. W. Chen, H. Chen, W. G. Zhu, Z. Y. Zhang, "A Comprehensive Study of the Formation and Suppression of Graphene Grain Boundaries on Cu and Cu-based Substrates", in preparation for *Phys. Rev. B.* (2014).

Vita

Wei Chen was born in Funing, Yancheng, Jiangsu, China on February 25, 1989, the son of Guohai Chen and Liping Yin. He attended the Funing Middle School and continued to Funing High School. He entered the Special Class for the Gifted Young, University of Science and Technology of China in 2005 as an undergraduate, and got his Bachelor of Science degree in Theoretical Physics in 2009. After that, he went to the University of Tennessee at Knoxville for graduate study in condensed matter physics.